Determination of 27Al(d, p&α) and 17O(p, p) reaction cross section at E < 2MeV

Marziyeh Salimi

▶ **To cite this version:**

Marziyeh Salimi. Determination of 27Al(d, p&α) and 17O(p, p) reaction cross section at E < 2MeV. Analytical chemistry. Sorbonne Université; K. N. Toosi University of Technology (Tehran, Iran), 2022. English. NNT : 2022SORUS123 . tel-03828361

HAL Id: tel-03828361

https://theses.hal.science/tel-03828361

Submitted on 25 Oct 2022

HAL is a multi-disciplinary open access archive for the deposit and dissemination of scientific research documents, whether they are published or not. The documents may come from teaching and research institutions in France or abroad, or from public or private research centers.

L'archive ouverte pluridisciplinaire **HAL**, est destinée au dépôt et à la diffusion de documents scientifiques de niveau recherche, publiés ou non, émanant des établissements d'enseignement et de recherche français ou étrangers, des laboratoires publics ou privés.

Sorbonne Université
Université Pierre et Marie Curie

Ecole doctorale 397, Physique et Chimie des Matériaux
Institut de Nanosciences de Paris - UMR7586

K.N.Toosi University of Technology
Physics Department

Determination of ^{27}Al(d, p&α) and ^{17}O(p, p) reaction cross section at E < 2MeV

MARZIYEH SALIMI

Thèse de doctorat de Physique

Directed by:

Prof. Ian Vickridge (Paris)
Prof. Farhad Masoudi (Tehran)

Présentée et soutenue publiquement le 14-03-2022
Devant un jury composé de (in alphabetical order) :

Dr. KHODJA, Hicham	Directeur de Recherche CEA, Rapporteur
Dr. MASOUDI Seyed Farhad	KNTU, Physics Department, Directeur de thèse
Dr. MONCOFFRE Nathalie	Directrice de Recherche, CNRS, Rapporteur
Dr. RADIN Mahdi, Associate Professor	KNTU, Physics Department, Examinateur
Dr. TRASSINELLI Martino	Chargé de Recherche, CNRS, Examinateur
Dr. VICKRIDGE, Ian	Directeur de Recherche, CNRS, Directeur de thèse

Except where otherwise noted, this work is licensed under
http://creativecommons.org/licenses/by-nc-nd/3.0/

Abstract

The overall objective of this thesis is to contribute experimentally determined and evaluated cross sections to a differential cross-section database for Ion Beam Analysis (IBA) that contains accurate and reliable data freely available to the user community, such as the Ion Beam Analysis Nuclear Data Library (IBANDL) database (https://www-nds.iaea.org/exfor/ibandl.htm) [1].

In the first part of the present thesis, we determined differential cross-sections of the reactions $^{27}Al(d, p\&\alpha)$ and benchmarked them with thick target spectra derived from pure aluminum in two independent laboratories. The differential cross section of $^{27}Al(d, p\&\alpha)$ reactions was determined between 1.4 MeV and 2 MeV at scattering angles of 165°, 150°, and 135° in the VDGT laboratory in Tehran (Iran), as well as measuring them again, including target preparation, at a scattering angle of 150° with independent equipment at INSP in Paris (France). We found close agreement between these two experimental measurements in two different laboratories at 150°. There is no nuclear reaction model that can be adjusted to represent these cross sections since the compound nucleus has a level structure that cannot be treated with current models. We proposed a fitted Fourier series function to represent the evaluated data to define the Al-cross sections. The evaluated differential cross sections have been benchmarked and validated using thick target charged particle spectra obtained using incident deuteron beams of energies between 1.6 MeV and 2 MeV at both laboratories. The validation was performed by fitting deuteron-induced particle spectra obtained from a high purity bulk Al target with SIMNRA, and the thick target spectra are reproduced, allowing the recommendation of the use of these cross sections for NRA.

In the second part of the present thesis, the elastic proton scattering cross sections on ^{17}O were measured for the first time at the SAFIR platform at INSP in Paris. Thin films of ^{17}O were prepared by thermal oxidation of Si at $1100\,^{\circ}C$ under $^{17}O_2$. The physical thickness of the silica was determined by ellipsometry and the atomic thickness by RBS with an uncertainty of 3%. The small quantities of ^{18}O and ^{16}O, present as impurities in the highly enriched $^{17}O_2$ gas used to grow these films, were determined by the established NRA techniques using the $^{18}O(p, \alpha)^{15}N$ and $^{16}O(d, p_1)^{17}O$ nuclear reactions.

We determined the yield of elastically scattered protons using the corresponding peak in the Elastic Backscattering (EBS) spectra; however, this peak sits on the large continu-

ous signal from the silicon substrate. The Si signal was significantly suppressed by aligning the incident beam with the $< 100 >$ axis of the single crystal silicon by ion channeling. The solid angle of the detector, placed at a scattering angle of 165°, was determined by elastic scattering measurements of 2 MeV alpha particles on a reference sample of Bi implanted in Si. The measured $^{17}O(p,p)$ cross section, with a systematic uncertainty of about 14%, consists of several resonant structures superimposed on a smoothly varying component increasing ranging from about 1.2 times the Rutherford cross section at 600 keV to about 3 times Rutherford at 2 MeV. A resonance at 1230 keV shows promise for EBS depth profiling, especially at large backscattering angles.

Acknowledgments

I am indebted to my thesis supervisor, Prof. Ian Vickridge, this work would not have been possible without his constant assistance, support, and guidance. His level of ingenuity, knowledge, and patience is something I will always keep aspiring to. He continuously provided encouragement and was always enthusiastic to assist for everything throughout my life and thesis. His brilliant, skillful advice enriched this study higher than my expectation. Looking back, one could definitely not have requested a better supervisor!

I would like to announce my sincere appreciation and gratitude to my Iranian supervisor Prof. Seyed Farhad Masoudi, whose well-organized supervision, supportive policy, and constructive advice have been invaluable throughout this study. His unassuming approach to science and research was a source of inspiration.

I also had the pleasure of working with the VDGT team, especially Prof O. Kakuee, Dr H. Rafi-kheiri, V. Fathollahi , Prof. M. Lamehi-Rachti, Abdolahzadeh, A. Biganeh and A. Jokar , who graciously taught and helped me with the use of accelerators and PVD systems as well as kindly answered all of my questions

I would like to acknowledge the SAFIR team in the INSP laboratory, especially Jean-Jacques Ganem, Emrick Briand, Martino Trassinelli and Isabelle Trimaille who generously assisted and cooperated in experimental work. I am also particularly indebted to Sebastien Steydli for assistance in mechanical and vacuum aspects, and Herve Tancrez for electronic and command-control systems development.

I gratefully appreciate the help of Erwan Dandeu, engineer of Semiconductor materials and Loïc Becerra, responsible for the cleanroom in the INSP laboratory. They not only taught me how to use the PVD and SEM system for preparation and characterization of my samples but also let me change the systems according to my requirement.

I would like to express thanks to Johan Meersschaut, Masoud Dialameh and André Vantomme, from Katholieke Universiteit Leuven, who devotedly and kindly received me in their laboratories. It was an honor for me to collaborate with them in measuring the amount of Boron in their samples at the Interuniversity Microelectronics Center (imec), Leuven in Belgium.

I am very thankful to Aliz Simon for receiving me warmly and giving me a chance to meet great scientists in the International Atomic Energy Agency (IAEA), in Vienna, Austria. It was an unforgettable experience! I have been more than delighted to be

given access for a visit to the “Atéliers de restorations” of the Musée du Louvre, Paris in France (Centre de recherche et de restauration des musées de France), and all my acknowledgements fall to PACHECO Claire AGLAE, Accélérateur Grand Louvre d'Analyse Elémentaire, a laboratory for ion beam analysis (IBA).

I also would like to thank in advance all esteemed Professors in Jury, Dr. KHODJA, Hicham; Dr. MONCOFFRE Nathalie; Dr. TRASSINELLI Martino and Dr. RADIN Mahdi, for reviewing this work, and sharing their wealth of scientific experiences. I am most grateful.

I would also like to express my deep appreciation of the strong support of M. Marangolo (Director of INSP), N. Witkowski (Director of the Doctoral School), Hakima.si Bachir and Patricia Zizzo for my co-tutelle doctoral contract. I immensely acknowledge the contribution from CAMPUS FRANCE in support of the co-tutelle doctoral contract.

Many thanks to all of the members of staff in KNTU and UPMC University for their kind support during my PhD study. Also, I extend my thanks to all my wonderful colleagues at KNTU and UPMC University, as well as to all of my friends who directly and indirectly provided me with valuable suggestions, and moral support.

My warm and heartfelt thanks go to my family for their tremendous help and hope they had given to me. Without that hope, this thesis would not have been possible. Thank you all for the strength you gave me. Similarly, other relatives are also subject to special thanks for their inspiration and heartening statements in my life. I love you all!

Finally, this expression of appreciation would not be complete if I did not admit that I deeply enjoyed my stay in Paris, France. It was the first experience of living abroad, traveling to several countries in Europe, finding new friends in different countries and familiarizing with the variety of cultures. Furthermore, I attended a RADIATE summer school (in louvre museum, Paris, France) and IBA2019 (Ion Beam Analysis) conference (in Antibes, France) in the first week of arrival. I had a chance to present two accepted papers in IBAF2021(”Ion Beam Applications” Francophone), one as oral and another as poster, also I was assigned as chair of poster session in IBAF2021.

List of Acronyms

Abbreviation

ANN	Artificial Neural Networks
CM	Center of Mass
EBS	Elastic (non-Rutherford) Backscattering
ERDA	Elastic Recoil Detection Analysis
FWHM	Full Width at Half-Maximum height
IAR	Isobaric Analogue Resonance
IBA	Ion Beam Analysis
PIXE	Particle Induced X-ray Emission
RBS	Rutherford Backscattering Spectrometry
NRA	Nuclear Reaction Analysis
NRP	Narrow Resonance Profiling
PIGE	Particle Induced Gamma Emission
PVD	Physical Vapour Deposition
VDG	Van de Graaff
VDGT	Van De Graaff Lab in Tehran
INSP	Institut des NanoSciences de Paris
SEM	Scanning Electron Microscopy

Variables

T	Kinetic energy for a particle when discussing nuclear physics
E_0	Initial kinetic energy of a charged particle used for IBA
M_u	Molar mass constant ($1g/mol$)
ρ	Density of the material
Z	Atomic number
A	Relative atomic mass
N_A	Avogadro number
M_1	Mass of the projectile
M_2	Mass of the nucleus
M_3	Mass of the outgoing particle
M_4	Mass of the residual nucleus

E_n	Energy of excitation in the nth excited state
N	Number of incident particle per cm^2
b	Impact parameter
m	Electron mass
v	Ion velocity
z	Atomic number
R	Nuclear diameter
r	Particle - nucleus distance in scattering calculations
B_c	Coulomb Barrier
Ω	Variance of the energy straggling distribution
S_A	Stopping power of element A
S	Bragg compound stopping power obtained from Bragg's rule

Contents

List of Figures

List of Tables

PART I : ENGLISH VERSION

Chapter 1

Introduction and Motivation

Ion Beam Analysis (IBA) is a suite of techniques based on the interactions of fast light ions with solids. In general, they require little or no sample preparation and are quantitative. The quantitative nature is general for Rutherford Backscattering Spectrometry (RBS), for which the scattering cross sections are known analytically (and with reliable screening corrections for high Z target elements), however for non-Rutherford Elastic Back Scattering (EBS) and for Nuclear Reaction Analysis (NRA) the cross sections are measured and, where possible, suitable nuclear reaction models with adjustable parameters can be adapted to express the cross section, allowing reliable interpolation, and in some cases extrapolation, to angle and energy ranges where no measurements exist. This thesis is concerned with the accurate determination of cross sections for two common elements for which suitable cross-sections have not yet been measured.

The first aim of the thesis is to accurately measure on the VDGT (Van de Graaff accelerator in Tehran) in Iran the cross sections of deuteron induced nuclear reactions on ^{27}Al, for which the measurements from the literature have significant differences. It is remarkably difficult to accurately measure cross sections – targets of various thicknesses, with compositions known to within about 1% are required, together with very accurate accelerator energy calibration and a high degree of mastery of the detection electronics. In addition to poor accelerator energy calibration and insufficiently well-characterized targets, effects such as uncontrolled electronic dead-time, target degradation under the beam, and incident beam current fluctuations amongst others are probably at the root of the variability amongst previously published cross sections. The Al cross sections measurements have been repeated at the INSP (Institute de Nanoscience) Paris. This is the first time that such cross sections have been measured on two independent systems.

Further to this careful metrological work, the thesis has determined for the first time the cross sections of the $^{17}O(p,p)^{17}O$ reactions, for which there is no literature data. Isotopically pure $^{nat}\mathrm{Si}^{17}\mathrm{O}_2$ targets have been produced by dry thermal oxidation of silicon in pure $^{17}O_2$ at INSP, which has the isotopically pure gas and the dedicated furnace facilities for handling this expensive gas. All measured cross sections are incorporated

into the IBANDL database [1] hosted and maintained by the International Atomic Energy Agency in Vienna.

This thesis is organized into 3 parts. The first, in English, presents an exhaustive review of my work, the second part is an extended abstract in French, and the third one is a short abstract in Persian.

In first part, in Chapter 2, the physics of the energy loss of ions in traversing matter and the interaction of charged particles with nuclei are presented. The incident charged particles lose their energy when penetrating matter, their energy distribution is broadened by energy straggling effects, and they undergo atomic and nuclear collisions with the target atoms and nuclei. The knowledge of these basic phenomena is very important for different methods of materials analysis using beams of charged particles.

In Chapter 3, the main IBA methods are introduced, together with their analytical characteristics, and a discussion of their relative strengths and weaknesses compared to other analytical techniques. Then, different experimental aspects and steps to the measurement of the cross section for IBA will be discussed.

Chapter 4 is based on our article titled "Determination and Benchmarking of ^{27}Al (d,α & p) Reaction Cross Sections for Energies and Angles Relevant to NRA" published in the Nature journal Scientific Reports [2]. We present the advantages of applying NRA with a deuterium beam, and explain why it is important to accurately know the differential $^{27}Al(d, \alpha \& p)$ cross sections. After reviewing previous relevant cross section measurements we present the cross-sections for the $^{27}Al(d, p_{0+1,2+3,4,5+6,9,10,11,12})$ and $^{27}Al(d, \alpha_{0,1,2,3,4})$ reactions at energies below 2 MeV and at 150° scattering angle in two completely independent measurements in two different laboratories: the Van De Graaff Lab in Tehran (VDGT) and the SAFIR platform of the Institute des NanoSciences de Paris (INSP). The $^{27}Al(d, p)$ and (d, α) cross-sections were also determined at 135° and 165° at VDGT. With our measured data and the critical evaluation of previous measurements, we propose a set of recommended cross-sections for NRA, embodied in fitted Fourier series functions, and demonstrate their validity through benchmarking experiments in a thick pure aluminum target in both laboratories.

Chapter 5 is based on a paper titled "Measurement of (p,p) Elastic Differential Cross Sections for ^{17}O in the 0.6–2 MeV range at 165° " published paper in Nucl. Instr. and Meth. Section B [3]. This paper presents the first measurements of the (p,p) Elastic Differential Cross Sections for ^{17}O. After explaining the purpose and importance of measuring the proton elastic scattering cross section on ^{17}O, we present the preparation and characterization ^{17}O thin film sample used for the measurement of the $^{17}O(p, p)$ elastic proton scattering cross sections at the SAFIR platform at INSP in Paris. The measured cross section $^{17}O(p, p)$ consists of resonant structures superimposed on a continuous background of Rutherford shape and of greater intensity than this. The elastic cross section is available on IBANDL [1].

In Chapter 6 we present overall conclusions and the perspectives for further work and articles. In chapter 7, we explain the summary of thesis in French. In chapter 8, we write a Persian abstract.

Chapter 2

Theoretical aspects of the physics underlying IBA

2.1 Energy loss and energy straggling

2.1.1 Introduction

One of the fundamental processes underlying materials analysis techniques using ion beams is the deceleration of ions in traversing materials. Depth perception follows from the energy lost by the incident beam and exiting particles, and the energy loss influences both elemental identification and quantitative analysis.

The basic physics of energy loss phenomena, involving different interactions among the target nuclei-electrons and projectile ions, are very complex, and also it is very important in different fields of physics and materials, so this topic has been studied since the beginning of the 20th century.

The theoretical physics related to energy loss [4–15], and its experimental investigation [16, 17] have been listed in the handbook in [18] and SRIM Website [19].

2.1.2 Basic concepts and definitions

Let us consider particles of mass M_1, atomic number Z_1 and initial energy E_0 traversing a layer composed of atoms with mass M_2 and atomic number Z_2, of thickness and areal density of N_t, where N is the volume atomic density. As shown in Figure 2.1, $\Delta E$is the average energy lost by the particles when traversing the thickness Δx. The average energy loss per unit depth is thus $\Delta E/\Delta x$. In the limit, as Δx goes to zero, $S = dE/dx$ is defined as the stopping power. The stopping cross section ε is given by Eq. 2.1.

$$\varepsilon = \left(\frac{1}{N}\right)\left(\frac{dE}{dx}\right) \tag{2.1}$$

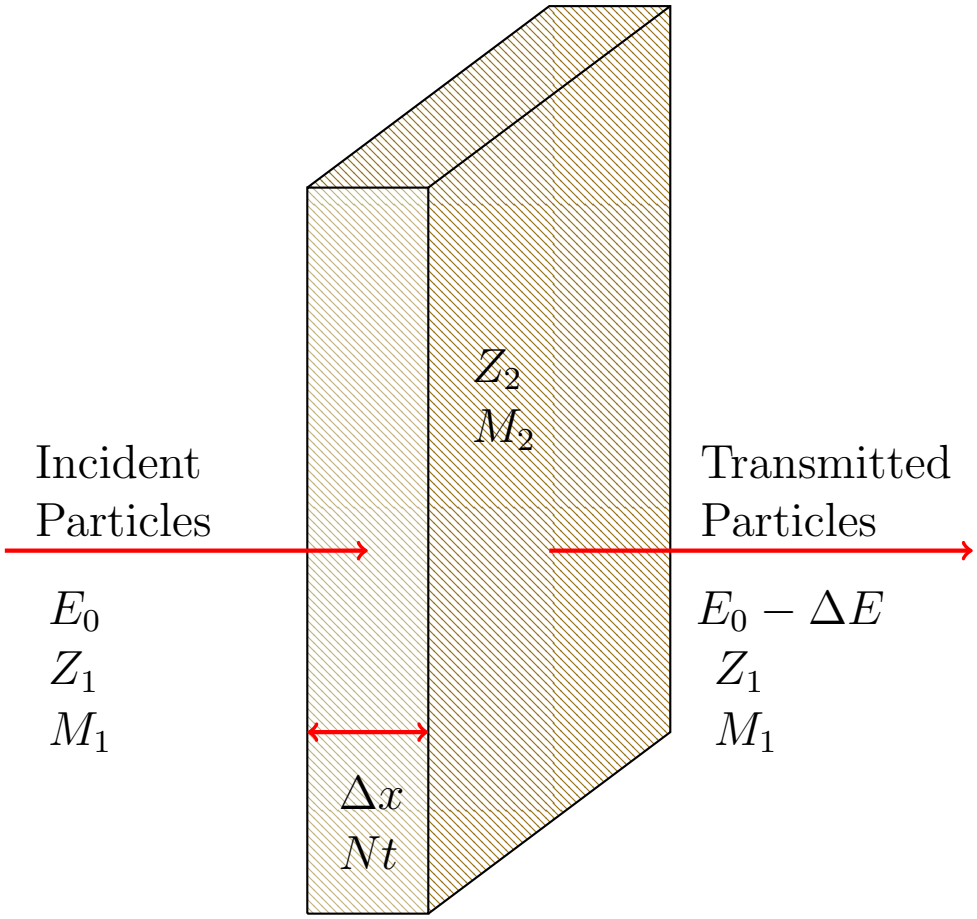

Figure 2.1: Definition of variables for stopping power discussion.

The stopping cross section given by Eq.2.1 is in $eV \times cm^2$ when the stopping power is given in eV/cm and N is given in at/cm^3. Unit conversions shown in Appendix I are relevant to energy loss calculations.

Bohr [4,20] developed the first expression for the stopping power for charged particles traversing matter, considering the interactions of charged particles with electrons, considered to be unbound and for electron mass m, elementary charge e, charge ze, ion speed v and the density of oscillators n with frequency ω:

$$\left(\frac{dE}{dx}\right)_{Bohr} = \frac{4\pi n z_1^2 e^4}{mv^2}\left[\ln\left(\frac{1.1229 mv^3}{|z_1|e^2\omega}\right)\right] \tag{2.2}$$

For a particle with energy E, charge ze, speed v, and traveling a distance x into a target of electron number density n and mean excitation potential I, the speed of light c and the vacuum permittivity ε , the electron charge e and rest mass m_e, $\beta = \frac{v}{c}$, Bethe [21] developed the relativistic equation 2.3:

$$-\left\langle\frac{dE}{dx}\right\rangle = \frac{4\pi}{m_e c^2} \times \frac{nz^2}{\beta^2} \times \left(\frac{e^2}{4\pi\varepsilon_0}\right)^2 \times \left[\ln\left(\frac{2m_e c^2\beta^2}{I \times (1-\beta^2)}\right) - \beta^2\right] \tag{2.3}$$

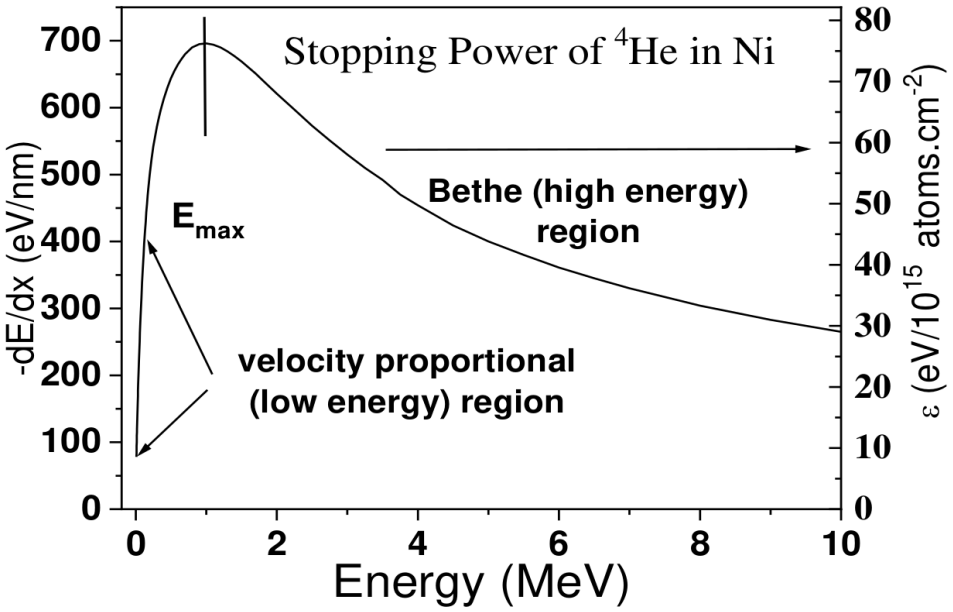

Figure 2.2: The typical stopping power variation with energy, using alpha particles in Ni as an illustration.

For the density of the material ρ, atomic number Z, relative atomic mass A, Molar mass constant M_u , and Avogadro number N_A , the electron density of the material can be calculated by Eq.2.4

$$n = \frac{N_A \times Z \times \rho}{A \times M_u} \tag{2.4}$$

The Bethe equation diverges at low particle energies, however at low enough particle energies the stopping power is strongly influenced by electron screening of the particle nuclear charge, and by the fact that the lower energy projectiles have less and less bound electrons that they can excite – effects which strongly reduce the stopping power – in this region, the stopping power is proportional to velocity [22]. The overall behavior of the stopping power is thus Bethe-like at high energies, and velocity-proportional at low energies, passing by a maximum value between the two regimes. However, despite successfully predicting these main features of the stopping power, none of these approaches is able to predict elemental stopping powers with the accuracy required by IBA.

The most widely used modern approach is to use semiempirical stopping powers where equations are established based on the theoretical work described above, with adjustable parameters that are determined by fits to measured experimental stopping powers. This approach is at the heart of the work of J. Ziegler [13], embodied in the SRIM stopping powers.

The typical stopping power variation with energy is given for example for ^4He in Ni in Figure 2.2:

The stopping powers of compounds may be estimated by a linear combination of the stopping power of their constituent elements – the Bragg rule. For a compound $A_aB_bC_c$ ...,

with elemental stopping powers S_A for each A, the stopping power S_{Bragg} of the compound is Eq.2.5:

$$S_{Bragg} = aS_A + bS_B + cS_C + ... \tag{2.5}$$

The energy loss ΔE of a particle penetrating a finite thickness x of target material, and the depth x at which a particle of initial energy E_0 attains energy E, are given by Eq.2.6:

$$\Delta E = \int_0^x \left(\frac{dE}{dx}\right) dx \qquad \text{or} \qquad x = \int_E^{E_0} \left(\frac{dE}{dx}\right)^{-1} dE \tag{2.6}$$

In general, Eq. 2.2 needs to be integrated numerically since, as mentioned above, accurate integrable expressions for dE/dx as a function of E (or of x) do not exist and so values must be read from tables or fitted semi-empirical expressions.

For thin targets, such as those used for the cross section measurements in this thesis, the surface energy loss approximation is given by Eq. 2.7 where it is assumed that the stopping power is constant over the thickness Δx

$$\Delta E = \frac{dE}{dx}(E_0)\Delta x \qquad \text{or} \qquad \Delta E = \varepsilon_0(E_0)Nt \tag{2.7}$$

With this approximation, the mean energy within the thin layer is $E_{av} = E_0 - dE/2$, which then gives Eq. 2.8:

$$\Delta E = \frac{dE}{dx}(E_{av})\Delta x \qquad \text{or} \qquad \Delta E = \varepsilon(E_{av})Nt \tag{2.8}$$

For thick targets such as those used for the Benchmarking experiments (see chapter 4), the appropriate numerical integrations are employed by the simulation code SIMNRA [23].

2.1.3 Bohr's theory of straggling

The slowing down of the incident ion beam as it traverses the material is accompanied by a spreading of the energy distribution of the particles which is called energy straggling. It arises from the statistical fluctuations in the number of collision events, and of the energy lost in each event. In ion beam analysis, straggling broadens spectral features and measured energy distributions, which leads to impaired depth and mass resolutions in RBS and NRA (Figure 2.3). The energy spread due to straggling increases with depth until the beam energy is close to the stopping power maximum, and then narrows as the ions lose the last of their energy [18, 24].

The energy loss is considered to be the result of a series of independent collisions between the incident particle and the target electrons. The total energy loss is the sum over the number of collisions, of the energy lost in each collision – both the number of collisions and the energy lost in each collision being described by probability distribu-

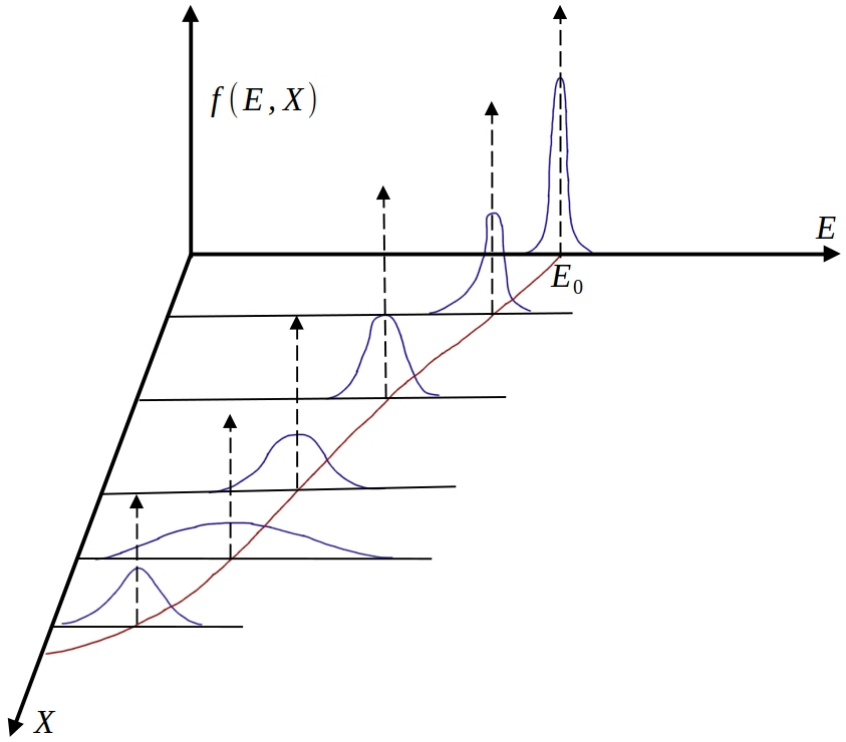

Figure 2.3: Straggling distributions as a function of beam penetration into a target [18]

tions. When the total energy loss is much greater than the average energy loss in an individual collision, the probability distribution of the energy loss is closely approximated by Gaussian function. For average energy losses greater than about 25% of the initial energy, the interactions between the charged particle and the electrons can no longer be considered to be independent (the stopping power changes significantly, for example) and the Gaussian approximation is no longer valid. Tschalar [25] has extensively considered energy loss distributions for large energy losses.

For high ion velocity, straggling is independent of ion velocity. For the energy loss distribution at high velocity and small enough average energy losses, Bohr calculated the energy loss variance Ω_B^2 given in Eq. 2.9, assuming that the electrons in the solid are free [26].

$$\Omega_B^2[keV^2] = 0.26 Z_1^2 Z_2 N t \left[10^{18} \frac{atoms}{cm^2}\right] \tag{2.9}$$

with the atomic number of the projectile (Z_1), the atomic number of the target (Z_2), the elementary charge (e), the density of target atoms (N) and the considered depth (t). If the distribution may be considered to be Gaussian of variance Ω , then the full width at half-maximum height (FWHM) of the energy loss function is given by Eq. 2.10.

$$\text{FWHM} = 2\sqrt{2\ln(2)}\Omega \approx 2.355\Omega \tag{2.10}$$

2.2 The interaction of charged particles with nuclei

2.2.1 Introduction

All the IBA methods except RBS and particle-induced X-ray emission (PIXE) spectroscopy, are based on nuclear interactions, so the knowledge of them is necessary to employ the IBA method in practice. The basics of projectile-nucleus interactions relevant to IBA were established by the 1960s. Although a number of theoretical models from low energy nuclear physics have been applied for IBA, beyond the Rutherford scattering cross section which can be calculated analytically, nuclear reaction cross sections cannot be calculated ab initio with a precision adequate for IBA [27]. The theories can, though, often produce a model for data evaluation, with parameters that are adjusted based on reliable experimental results. The nuclear physics relevant to IBA is explained in this section. It is widespread to use the cgs (cm, g, second) system of units in nuclear physics since the equations are simpler to read. This convention is applied in section 2.2.2. In the following section we present the fundamentals of non-relativistic low energy nuclear scattering theory that has concepts applicable not only for the cross sections measured here, but more generally for EBS and NRA cross sections relevant to IBA.

We first consider the theory of Elastic scattering in section 2.2.2, and then, in section 2.2.3, consider the basics of nuclear reaction theory, for Q not equal to 0, relevant to the work presented in this thesis.

2.2.2 The formal theory of elastic scattering

An atomic nucleus, as a strongly bound system of nucleons, may be characterized by a volume of radius R, given in Eq. 2.11:

$$R \approx (1.1 - 1.5)A^{1/3} \text{ fm} \tag{2.11}$$

where A is the mass number.

Nuclear forces are attractive and act at a short distance. They are very specific to each nucleus. At short distances, about 1 fm = 10 $^{-13}$ cm, nuclear forces are typically more than 100 times greater than Coulomb forces.

For a point projectile of charge z, at distance r from a nucleus assumed to be a uniformly charged sphere of radius R and charge Z, the electrostatic potential energy is Eq. 2.12:

$$V_c(r) = \begin{cases} \frac{Zze^2}{r} & , r \geq R \\ \frac{Zze^2}{2R}\left(3 - \frac{r^2}{R^2}\right) & , r \leq R \end{cases} \tag{2.12}$$

The potential energy for the attractive forces is negative so that the nuclear potential

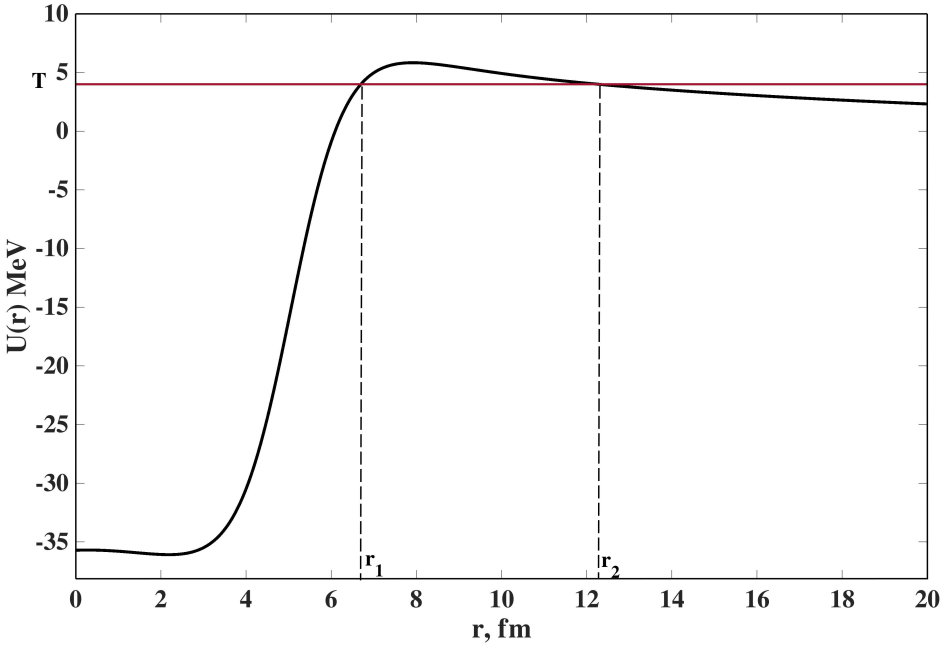

Figure 2.4: The combined Coulomb and nuclear potential of a nucleus [18].

is a potential well. For the combined nuclear and Coulomb potential, the transfer from repulsion to attraction occurs within a short distance in the vicinity of the boundary of the nucleus.

In order for a charged projectile to be able approach the target nucleus sufficiently closely that nuclear forces come into play, the kinetic energy T of the charged projectile, shown in Figure 2.4, should be great enough to overcome the Coulomb potential barrier. The height of the Coulomb barrier B_c is simply the potential at the distance R, and is given by Eq. 2.13:

$$B_c = \frac{Zze^2}{R} \tag{2.13}$$

For protons incident on ^{17}O,B$_c$ is about 3.2 MeV, however even at incident particle energies below B c the nuclear potential can influence the interaction through quantum tunneling effects. This is the case for the $^{17}O(p,p)^{17}0$ cross sections measured in this thesis. Since the proton and the neutron in a deuteron are only weakly bound, and the neutron itself is not subject to the Coulomb barrier, deuteron induced reactions can also occur at energies substantially below the Coulomb barrier, as is the case for the $^{27}Al(d,p\&\alpha)$ reactions measured in this thesis, for which B_c is about 4.4 MeV.

2.2.3 Elastic scattering in a pure Coulomb potential

For long-range electric forces in the projectile-nucleus interaction, the differential elastic scattering cross-section is obtained from the conservation of the angular momentum and energy (shown Figure 2.5).

If the interaction law is known, it is plausible to discover the relation between the

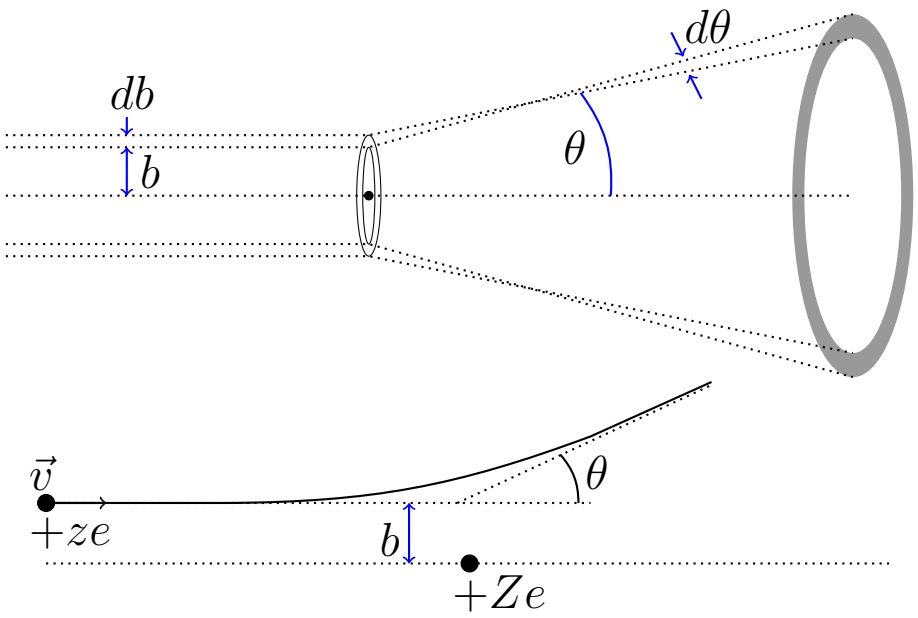

Figure 2.5: Definition of variables for discussion of projectile scattering by the electric field of the nucleus [18]

scattering angle and the impact parameter b, which is expressed in the nonrelativistic case by Eq. 2.14:

$$\tan\theta = \frac{2Zze^2}{mv^2b} \tag{2.14}$$

If N incident particles per cm^2 interact with a single stationary nucleus, then dN ions are scattered in the angle interval from θ to $\theta + d\theta$ shown in Eq. 2.15:

$$dN = N2\pi bdb \tag{2.15}$$

The ratio of scattered particles to the beam fluence is equal to the area of the ring with radii b and $b + db$ that surrounds the center of scattering.

$$d\sigma = \frac{dN}{N} = 2\pi bdb \tag{2.16}$$

In the absence of nuclear forces, for a purely Coulomb interaction, the differential cross section is given by the Rutherford formula. For a target with charge Ze and incident beam with charge ze, $\frac{d\sigma}{d\Omega}$ may be written as shown in Eq. 2.17 [28].

$$\frac{d\sigma}{d\Omega} = \left(\frac{1}{4\pi\varepsilon_0}\right)^2 \left(\frac{Zze^2}{mv^2}\right)^2 \frac{1}{4\sin^4\frac{\theta}{2}} \tag{2.17}$$

This is valid for energies, masses, and atomic numbers for which the two particles do not approach each other closer than about R. When the incident particle is located closer to the nucleus than about R, the uncertainty in its momentum (and therefore

kinetic energy) become significant according to the Heisenberg's uncertainty principle ($\Delta x \Delta p \geq \hbar$). Classical mechanics can no longer be applied, and wave mechanics must be used.

2.2.3.1 Scattering with a nuclear potential

In accordance with quantum mechanics, the state of a particle is defined by the wave function, Ψ, a solution to the Schrodinger wave Eq. 2.18:

$$\Delta\Psi + \frac{2m}{\hbar}(E - V)\Psi = 0 \tag{2.18}$$

For the elastic scattering of spinless nonidentical particles of energy E and momentum p in a spherically symmetrical potential V the solution to the Schrodinger equation is a plane wave Eq. 2.19:

$$\Psi = e^{i\vec{k}z} \tag{2.19}$$

$$\lambda' = \frac{\lambda}{2\pi} \qquad , \qquad \vec{k} = \frac{\vec{p}}{\hbar} = \frac{1}{\hbar} \tag{2.20}$$

where $\vec{k}$ and λ are a propagation vector and the de Broglie wavelength.

When $V = 0$, Eq. 2.18 reduces to Eq. 2.21:

$$\Delta\Psi + \frac{2m}{\hbar}E\Psi = 0 \tag{2.21}$$

For which the solution is a plane wave – the projectile propagates with no change of velocity.

Upon scattering, due to the interaction of the plane wave with the field of the nucleu V(r), it produces a spherical wave divergent from the center of the interaction which has the form Eq. 2.22:

$$f(\theta) \times \frac{e^{ikr}}{r} \tag{2.22}$$

At the end of scattering action, a superposition of the plane wave and the spherical wave is illustrated as form in Eq. 2.23

$$e^{ikz} + e^{ikr} \times \frac{f(\theta)}{r} \tag{2.23}$$

Where θ and $f(\theta)$ are the scattering angle and the amplitude of the divergent wave. The $1/r$ factor displays the decreasing of the flux in inverse proportionality to the square of the distance.

Let us recall that the differential cross-section $d\sigma$ is defined by the fraction dN/N of projectiles scattered into the solid angle $d\Omega$. The flux density $N = \rho v$ where ρ is the volume density of the beam and v is the velocity of particles in the beam. Assuming the primary beam to have unity density of particles, then $N = v[S^{-1}cm^{-2}]$. The probability

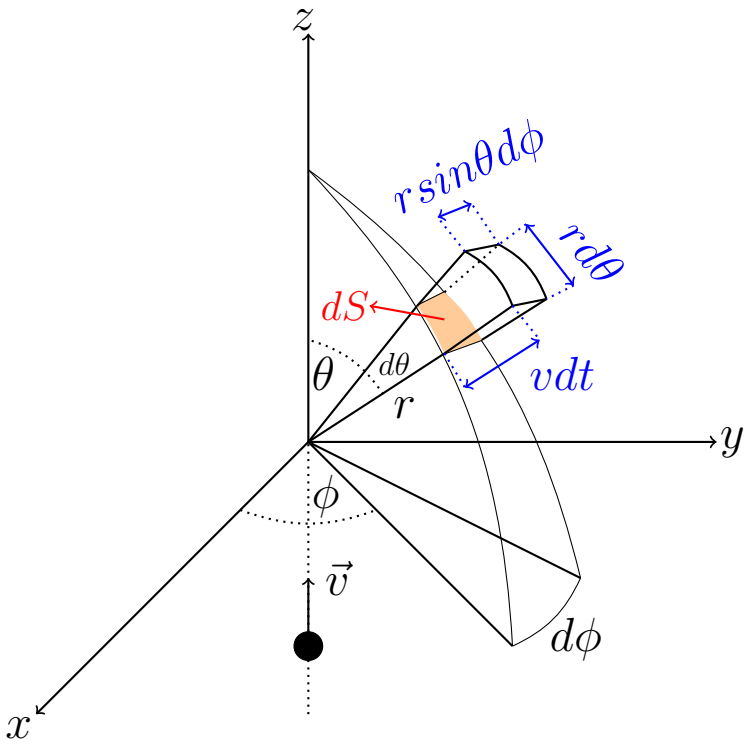

Figure 2.6: Schema for the description of the differential cross section, redrawn from [18]

of finding particles in the elementary volume (dV) determine with the number of particles (dN) traveling through the surface element (dS) per unit of time (Eq. 2.24, Figure 2.5 and Figure 2.6), and the probability density is calculated by the square of the modulus of the scattered wave function (Eq. 2.25):

$$dV = Vr^2 \sin d\theta d\phi \tag{2.24}$$

$$dN = \left| f\left(\theta\right) \frac{e^{ikr}}{r} \right|^2 vr^2 \sin\theta d\theta d\phi \tag{2.25}$$

The velocity is constant in elastic scattering, and $sin(\theta) \times d\theta \times d\Psi = d\Omega$, so the differential cross section is given via the square of the modulus of the amplitude of the scattered wave (Eq. 2.26):

$$d\sigma = \frac{dN}{N} = \frac{\left|f\left(\theta\right)\right|^2 r^2 v d\Omega}{r^2 v} = \left|f\left(\theta\right)\right|^2 d\Omega \tag{2.26}$$

$$\frac{d\sigma}{d\Omega} = \left|f\left(\theta\right)\right|^2 \tag{2.27}$$

where $f(\theta)$ is the angular distribution of the scattered particles.

For quantitative analysis of the elastic scattering, Eqs. 2.18 and 2.21 are considered in spherical coordinates. The general solution of Eqs. 2.18 has the form of Eq. 2.28)

$$\Psi = \sum_{l=0}^{\infty} Al \times P_l\left(\cos\theta\right) \times R_{kl}(r) \tag{2.28}$$

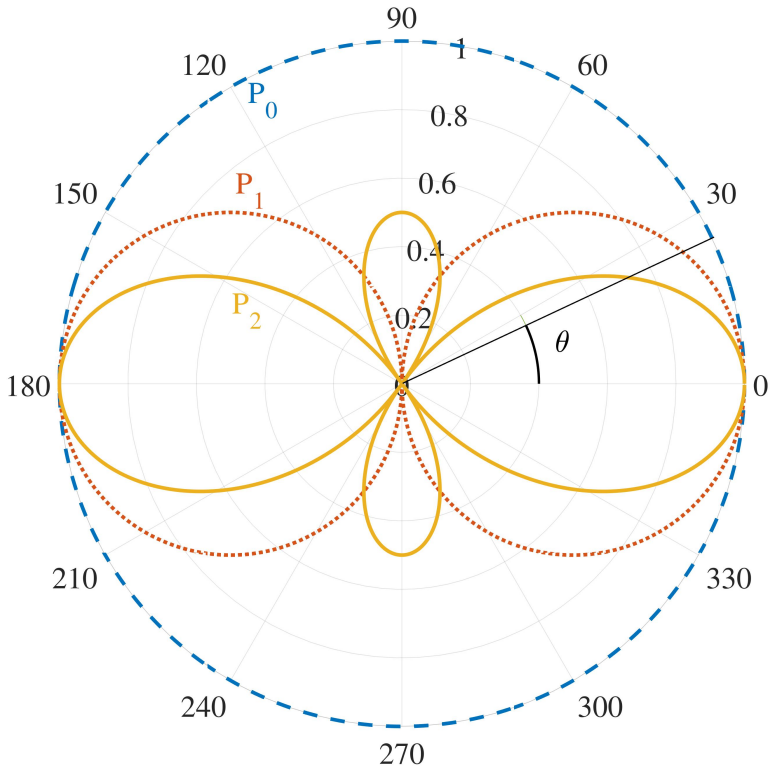

Figure 2.7: Angular distributions for the first three partial waves in Eq. 2.30

Where $R_{kl}(r)$ and $P_l(\cos\theta)$ are a radial wave function and a Legendre polynomial.

For a large distance (r) from the center of scattering, the radial function for every part is illustrated by one convergent and one divergent partial spherical wave form.

For the first step, the two-plane waves have identical amplitudes, as expressed in Eq. 2.29

$$R_{kl}\left(r\right) \approx e^{i\left(kr-\frac{l\pi}{2}\right)} - e^{-i\left(kr-\frac{l\pi}{2}\right)} \tag{2.29}$$

Therefore, the plane wave is represented through an extension over Legendre polynomials which has the form Eq. 2.30

$$e^{ikz} = \sum_{l=0}^{\infty} \frac{(2\times l+1)\times i^l}{2\times i\times k\times r} \times P_l\left(\cos\theta\right) \times \left[e^{i\left(kr-\frac{l\pi}{2}\right)} - e^{-i\left(kr-\frac{l\pi}{2}\right)}\right] \tag{2.30}$$

In Figure 2.7, each of the spherical waves is related to particles moving with an orbital momentum l and it is identified by the angular distribution $P_l(\cos\theta)$.

As the scattering proceeds, the production of an additional divergent spherical wave causes the ratio between the divergent and convergent waves to change, as is shown by a coefficient at the divergent wave in Eq. 2.31

$$R_{kl}\left(r\right) \approx S_l\times e^{i\left(kr-\frac{l\pi}{2}\right)} - e^{-i\left(kr-\frac{l\pi}{2}\right)} \tag{2.31}$$

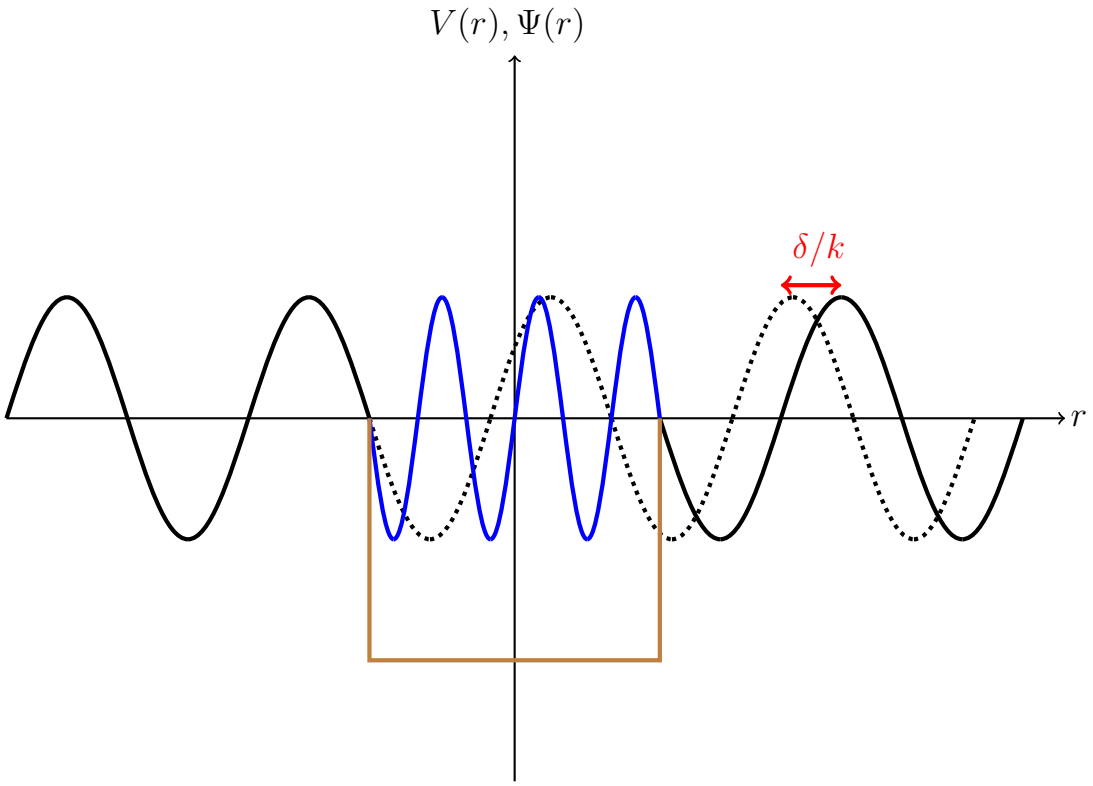

Figure 2.8: Illustration of the wave phase shift structure [18].

For elastic scattering, the fluxes for the divergent and convergent waves should be equivalent to 1, which means that $|S_l|^2 = 1$, giving

$$S_l = e^{2i\delta_l} \tag{2.32}$$

where δ_l is the phase shift, which is the difference in the wave velocity in the absence and presence of the nuclear force field, as shown in Figure 2.8.

After scattering, the partial wave has the form Eq. 2.33. For the final stage of scattering, the solution of Eq. 2.18 is Eq. 2.34. The relationship between the phases and scattering amplitude is given by Eq. 2.35

$$R_{kl}(r) \approx e^{i\left(kr-\frac{l\pi}{2}+2\delta_l\right)} - e^{-i\left(kr-\frac{l\pi}{2}\right)} \tag{2.33}$$

$$e^{ikz} + \frac{f(\theta) \times e^{ikr}}{r} = \sum_{l=0}^{\infty} \frac{(2 \times l + 1) \times i^l}{2 \times i \times k \times r} P_l(\cos\theta) \left[S_l e^{i\left(kr-\frac{l\pi}{2}\right)} - e^{-i\left(kr-\frac{l\pi}{2}\right)}\right] \tag{2.34}$$

$$f(\theta) = \frac{1}{2 \times i \times k} \sum_{l=0}^{\infty} (2 \times l + 1) \left(e^{2\times i\times\delta_l} - 1\right) P_l(\cos\theta) \tag{2.35}$$

To summarize for elastic scattering, the differential cross section is calculated from Eq. 2.27, with the scattering amplitude of phase shifts δ_l according to Eq. 2.35. For partial waves, the phase shifts are determined by solving the Schrodinger equation [Eq.

2.18] with a potential $V(r)$. This equation is divided into radial and angular parts. For the radial equation, the asymptotic general solution is Eq. 2.36.

$$R_{kl} \approx \sqrt{\frac{2}{\pi}} \frac{1}{r} \sin\left(kr - l\frac{\pi}{2} + \delta_l\right) \tag{2.36}$$

According to the boundary conditions, the phase shifts δ_l are functions of l and k but do not rely on the scattering angle.

For a charged projectile, the interaction is determined by the combined Coulomb and nuclear fields of the target nucleus. The scattering amplitude is given by Eq. 2.37.

$$f(\theta) = f_c(\theta) + \frac{1}{2 \times i \times k} \sum_{l=0}^{\infty} (2 \times l + 1) \times (S_l - 1) \times e^{2i\sigma_l} P_l(\cos\theta) \tag{2.37}$$

where σ_l and $f_c(\theta)$ is the phase shift and amplitude of the Coulomb scattering, respectively. For elastic scattering, the phase shifts are real numbers. The S_l values are scattering matrix, elements of some diagonal matrix, calculated by Eq. 2.32.

2.2.4 The projectile-nucleus interaction mechanism

Scattering resulting from direct interaction of a bombarding particle with a nuclear potential well is called direct or potential scattering. At low energies, nuclear interactions can also happen in two stages via the mechanism of compound nuclei. Absorption of the bombarding particle by the target nucleus is the first stage of the interaction, leading to the generation of an intermediate or compound nucleus. A compound nucleus is always extremely excited since it absorbs both its kinetic energy and nucleon bond energy. In the second stage, a compound nucleus decays by emitting some particles. The original nucleus can always be reformed if the original particle is omitted. The lifetime of a compound nucleus is typically 10^{-14} s, which is many orders of magnitude longer than the direct interaction time (10^{-23} to 10^{-21} s) that is required for the incident particle to traverse the potential well [29].

Due to the basic principle of quantum mechanics, the energy of particles moving through a finite region of space is quantized, having only discrete allowed values. Since the particles constituting the nucleus are bound within the confines of the nucleus, all nuclei therefore have discrete energy levels, as illustrated in Figure 2.9, leading for light nuclei, to resonance structures in their cross sections as a function of incident particle energy. For heavy nuclei, the density of levels is high, causing the levels to overlap at low excitation energies when the level width (Γ) is greater than the distances between the levels (D). In consequence, this leads to a smoother dependence of cross sections on energy. When $\Gamma \sim D$, in the intermediate condition, the cross section displays a highly fluctuating structure which is called Ericson fluctuations. Due to the long lifetime

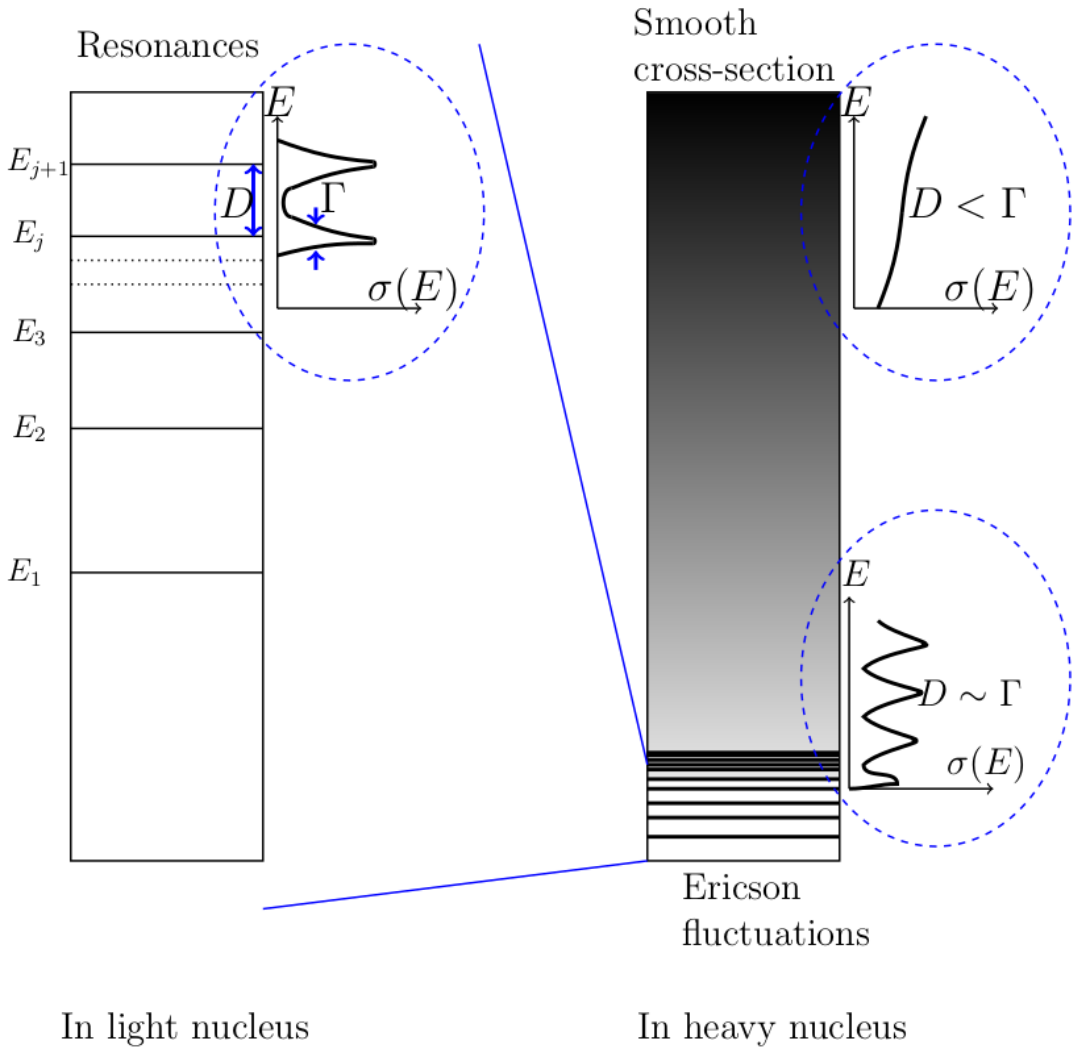

Figure 2.9: Diagrams showing the energy levels of the light and heavy nuclei and the corresponding generalised cross section behaviour for elastic scattering by the nuclei [18]

and the uncertainty relation $\Delta E.\Delta t \geq \hbar$ the widths of the compound nucleus levels are rather small, as are the widths of the resonances observed in the cross section. Due to the interference between potential and resonance scattering, the excitation function has a symmetric structure with resonances depicted as peaks and valleys rather than as BreitWigner functions (Figure 2.10).

The cross sections for the compound nucleus formed by the interaction of protons with a medium- or heavy-weight nucleus might still contain some strong sharp resonances despite the intense overlap between the exciting levels. Isobaric analog resonances (IAR) occur because of the population of isobaric analogue states in the compound nucleus. The interaction of p-p, n-p, and n-n are similar except for electrical forces. The energy levels of isobaric (equal-A) nuclei are thus relatively unaffected by proton-neutron interchange. In the (Z+1,N) nucleus, the isobaric analog states will possess the same properties as the (Z,N+l) nuclear energy states. However, the energy state shift will be equal to ΔE as shown in Eq. 2.38 because of the increased Coulomb energy related to the extra proton.

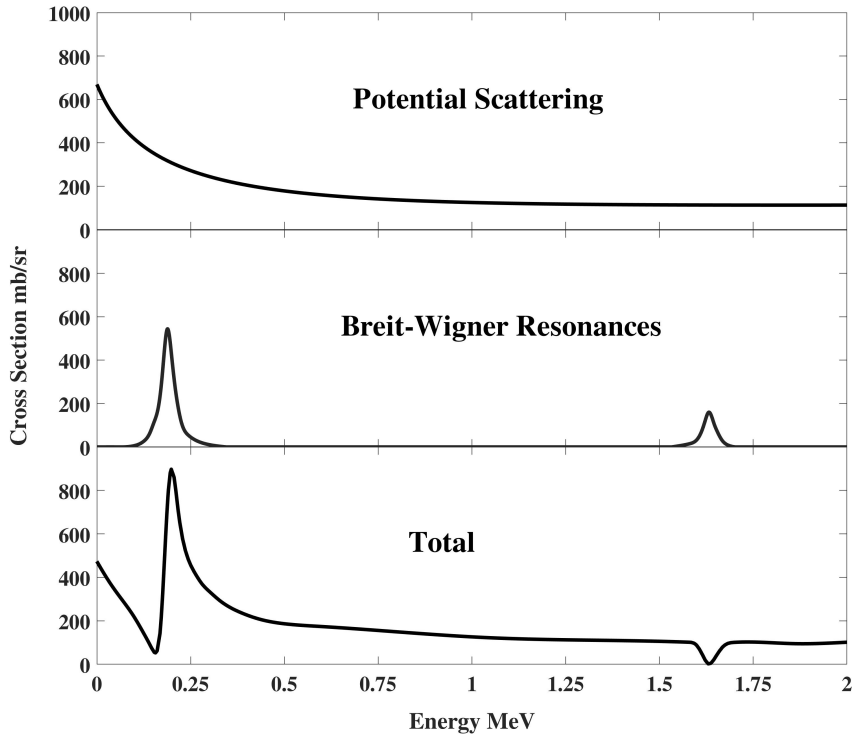

Figure 2.10: Resonances have a tremendous effect on the cross section at energies much smaller than the Coulomb barrier [18].

This difference in mass will be less than the neutron-proton mass difference (Figure 2.11).

$$\Delta E = \delta E_c - (m_u - m_p)\, c^2 \tag{2.38}$$

At sub-Coulomb energy, elastic scattering cross section deviates from the Rutherford value in most cases because of lARs. Calculations of the cross section can be performed using the resonance structure of the compound nucleus.

In addition to elastic scattering, identified by the kinetic energy conservation and identical particles in the input and output channels, various types of nuclear reactions may occur. In these cases, electric charge, the number of nucleons, the mass-energy, the parity, and the angular momentum are conserved [18].

We write the reaction of an incident particle A of non-zero rest mass m_1 and atomic number Z_1 interacting with a target nucleus B of rest non-zero rest mass m_2 and atomic number Z_2 , producing a light product $b, (M_3\,,\, Z_3)$ and a heavy product $B\,(M_4\,,\, Z_4)$ as: A(a,b)B.

The nuclear reaction may produce or absorb energy by inter-conversion of energy and mass, and/or by excitation of internal nuclear states. If all of the reactants and products are in their ground states then the amount of energy, Q_0 , available is given by the Einstein

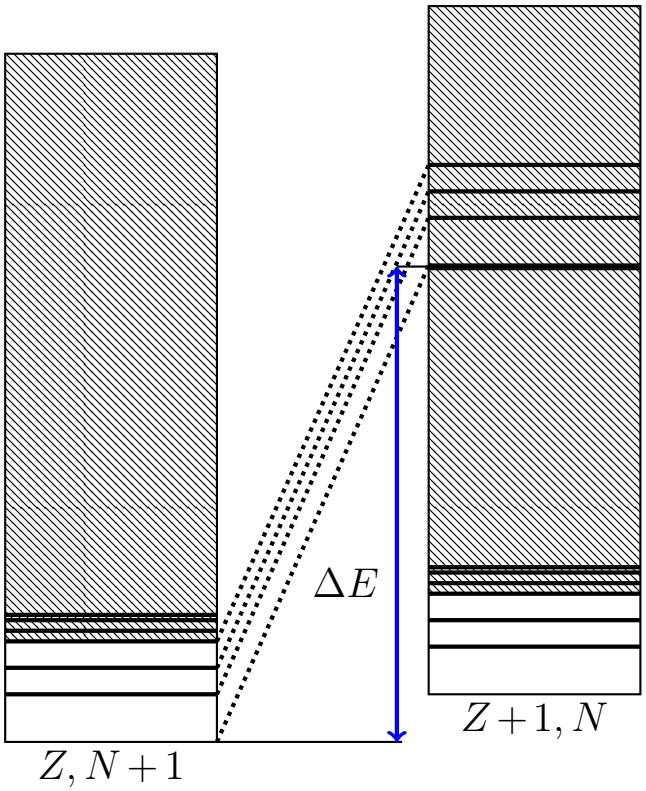

Figure 2.11: Illustration of the level scheme for isobaric analogue states [18].

relation $E = mc^2$ and with the mass of the projectile (M_1), target nucleus (M_2), outgoing particle (M_3), and residual nucleus (M_4),

$$Q = (M_1 + M_2)\, c^2 - (M_3 + M_4)\, c^2 \tag{2.39}$$

For Q positive, the reaction is exothermic and can occur at any energy, whereas for Q negative, the reaction is endothermic with a threshold and can happen only when the projectile contributes more energy than this threshold. Endothermic reactions require the input of external energy, usually the kinetic energy of the reactants, to proceed. The special case of $Q = 0$ indicates elastic scattering, and $a = b$, $A = B$. This is the case for example for Rutherford scattering RBS, Elastic Backscattering EBS and Elastic recoil detection ERDA.

For Q value correspond to ground state of B, Q_0, If after the reaction, one of the products (usually the heavy product B) remains in the n^{th} excited state, of excitation energy E_n , then the reaction energy available for the kinetic energies of the reaction products is reduced by E_n so that we write [29]:

$$Q_n = Q_0 - E_n \tag{2.40}$$

It is a direct reaction mechanism if the projectile's energy is transferred to one nucleon

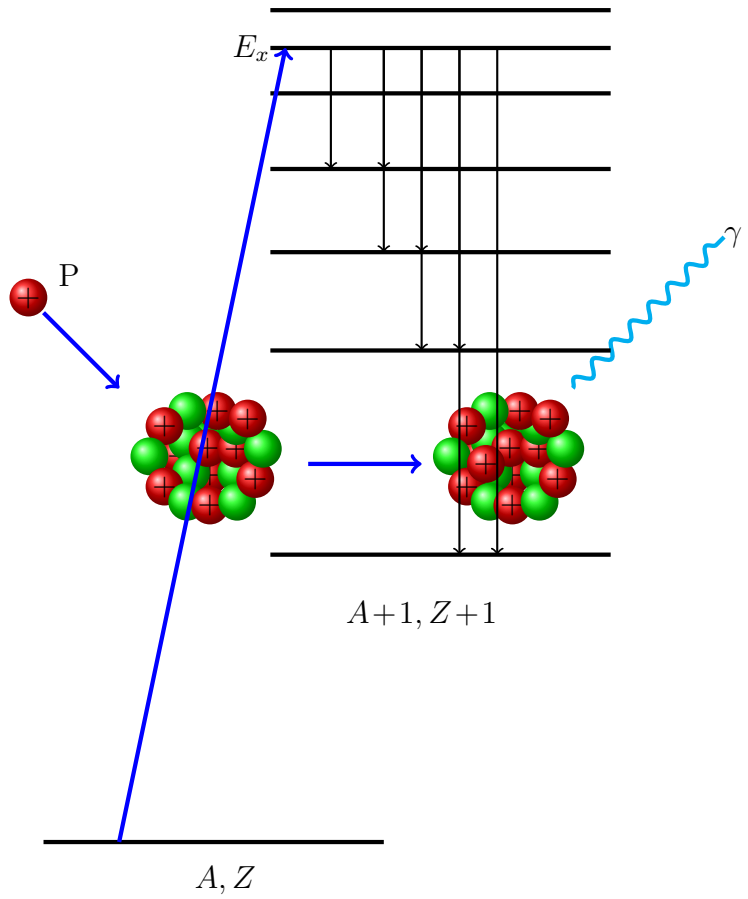

Figure 2.12: Level scheme of a (p, γ) reaction [18]

or a small group of nucleons, whereas if the energy is transferred to all of the nucleons, it is a compound reaction mechanism.

Inelastic interactions induced by protons, for example (p, γ), (p, α), $(p, p'\gamma)$, and $(p, \alpha\gamma)$ reactions, are amongst the most important non-elastic processes induced by protons in IBA. The inelastic scattering can occur if the energy of the projectile is greater than that of the first excited state within the target nucleus in the center-of-mass system. In the case of $(p, p'\gamma)$, there are then additional peaks seen at energies less than the energy of the elastic peak in backscattering spectra.

(p, α) reactions are mostly exothermic (Q $\sim$ 1-3 MeV) but the cross sections of these reactions are generally small due to the large Coulomb barrier for particles. For (p, n) reactions that result in excited states in the residual nucleus, for low-energy protons the cross section is negligible.

(p, γ) reactions emit γ-rays with different energies that correspond to the transitions amongst various levels of the residual nucleus as shown in Figure 2.12. Because the proton is not only bringing its kinetic energy to the compound nucleus, but also its binding energy (on average about 8 MeV), the compound nucleus can become extremely excited. For the initial proton energy (E_0), the reaction energy (Q), the projectile nucleus masses (M_1)

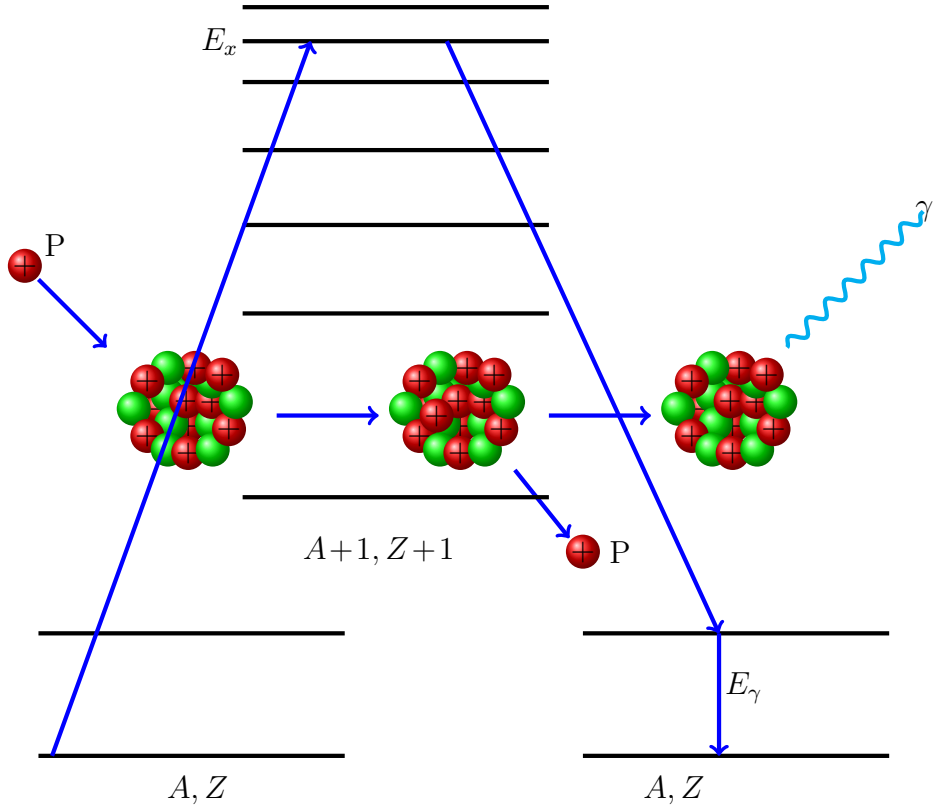

Figure 2.13: The level scheme for a $(p, p'\gamma)$ reaction [18].

and target nucleus masses (M_2), Eq. 2.41 shows the excitation energy:

$$E_x = \frac{M_2}{M_1 + M_2} \times E_0 + Q \tag{2.41}$$

With the excited state's energy in the residual nucleus (E_{level}), we can calculate the energy of the emitted primary γ-rays with Eq. 2.42.

$$E_\gamma^{(i)} = E_x - E_{level}^{(i)} \tag{2.42}$$

The $(p, p\gamma')$ reaction can only occur if the projectile energy outpaces the first energy level within the target nucleus (see Figure 2.12). In fact, this reaction involves inelastic scattering along with γ-emission from the residual nucleus. The process of $(p, \alpha\gamma)$ and $(p, n\gamma)$ reactions are similar to those shown in Figure 2.13 with the exception that the compound nucleus emits another particle instead of a proton.

For deuteron-induced reactions, there are three mechanisms contributing to the process's total amplitude: stripping, resonance, and statistical. In stripping, which is a direct process, a deuteron is aligned in such a way that its proton is farther from the target nucleus than its neutron because of electrical forces. Due to the small deuteron binding energy (about -2.2 MeV), the neutron might be attracted by the nucleus, as the proton continues its trajectory past the target nucleus. According to the statistical mechanism,

the levels of compound nuclei overlap fully. Projectile energy is assumed to transfer to all nucleons of the nucleus. Thus, the nucleus is "heated" to a certain temperature. In the excited state, the excitation energy may become concentrated on one of the nucleons (or clusters), which is then "evaporated" from the nucleus.

Considering that deuterium only has a binding energy of -1 MeV per nucleon, while other nuclei have its -8 MeV per nucleon, the binding energy of a deuteron in a compound nucleus is about 14 MeV. As a result, if a compound nucleus absorbs an accelerated deuteron, the excitation energy will be high, so different highly exoergic reactions are achievable.

Chapter 3

Ion Beam Analysis

3.1 Introduction

Ion beam analysis (IBA) is a set of modern analytical techniques based on atomic and nuclear reactions between accelerated charged particles and materials, leading to the emission of particles or photons. In the simplest cases, the energy of the emitted radiation is specific to an elemental or isotopic constituent of the sample, and its intensity is proportional to the concentration of that constituent [30].

IBA techniques are generally nondestructive in the sense that the analysed sample is not consumed by the analysis, with no special requirement for Preparing samples. A small quantity (mg) and size (less than 0.5 mm) of sample is sufficient for analyzing multi elementary samples, and analysis is typically rapid – a few minutes per analysis point to produce high-accuracy quantitative results. IBA analysis probes up to 1 to 50 microns below the surface of the samples. Although generally non-destructive, sample damage may occur due to displacement of target atoms from elastic collisions, charge buildup due to ionization, and surface contamination (notably, carbon contamination) under the analyzing beam if the target chamber has poor vacuum.

IBA may be used for delicate samples such as polymers and single crystals, however care must be taken to evaluate measurement induced damage. Based on an operational point of view, the damage induced by IBA measurements may be divided into two types: Type I and Type II [31] . Type I damage may be observed by its effects on the measured quantity, during the measurement, and thus leads to a measurement artefact. Any other damage that occurs in the sample due to the IBA measurement is termed Type II damage. Type II damage changes other properties than that determined by the IBA measurement of the sample.

IBA requires an Electrostatic particle accelerator producing MeV beams of protons, deuterons, ^{3}He, ^{4}He, heavy ions; charged particle, X-ray and gamma detectors; scattering chamber or beam extraction into air; data acquisition and spectral analysis software

and hardware. Knowledge of the underlying physics of charged particle interactions with matter-stopping power, ionization and X-ray production cross sections, elastic and nuclear interaction cross sections – is of course necessary to properly interpret IBA results and to design good IBA measurements.

The characteristics of IBA have led to broad application in large multi-elemental analysis applications, and in materials science. Many applications are presented in the bi-annual IBA [32] and related conferences. We mention here application for fine aerosol particulate monitoring, cultural heritage provenance and authentication, in geology, in biology and in studies of thin film growth.

We present here first the general characteristics of the main IBA methods, and then some specific experimental aspects of IBA, including accelerator energy calibration and target preparation used in this thesis.

3.2 The different methods of Ion beam analysis

IBA can be divided into several specific methods, depending on the incident beam and the detected interaction products, which are: Rutherford Backscattering Spectrometry (RBS), Elastic (non-Rutherford) Backscattering Spectrometry (EBS), Elastic recoil detection (ERD), Particle Induced Gamma Emission (PIGE), Particle Induced X-ray Emission (PIXE) and Nuclear Reaction Analysis (NRA) as summarized in Figure 3.1, Ion Channeling [26], in which the incident particle beam is directed along a major axis or plane of a single crystalline sample can be applied with all of the IBA methods. Here, we present the various IBA techniques in decreasing order of the underlying cross sections. In what follows we use the notation A(a, b)B to represent the interaction where particle a is incident on particle A, and the underlined product b is detected, leaving the residual particle B. A is heavier than a, and B is heavier than b [33].

3.2.1 PIXE: $A(a, \underline{x})A$

PIXE occurs in two steps: (1) ionization of a target atom's inner shell by an incoming ion; (2) filling in the resulting electronic vacancy with an outer shell electron along with emission of the excess energy by the emission of a characteristic X-rays According to Moseley's law in Eq. 3.1, for a different constant for each spectral series (C) and a shielding constant close to 1 (s), an emitted X-ray's energy is directly related to the material's atomic number (Z):

$$E = C(Z - s)^2 \tag{3.1}$$

The X-ray production rate per incident ion is determined by the ionization cross section of the particular inner shell, which depends on the incident particle energy and the target element atomic number, and on the proportion of outer shell electrons which lose their

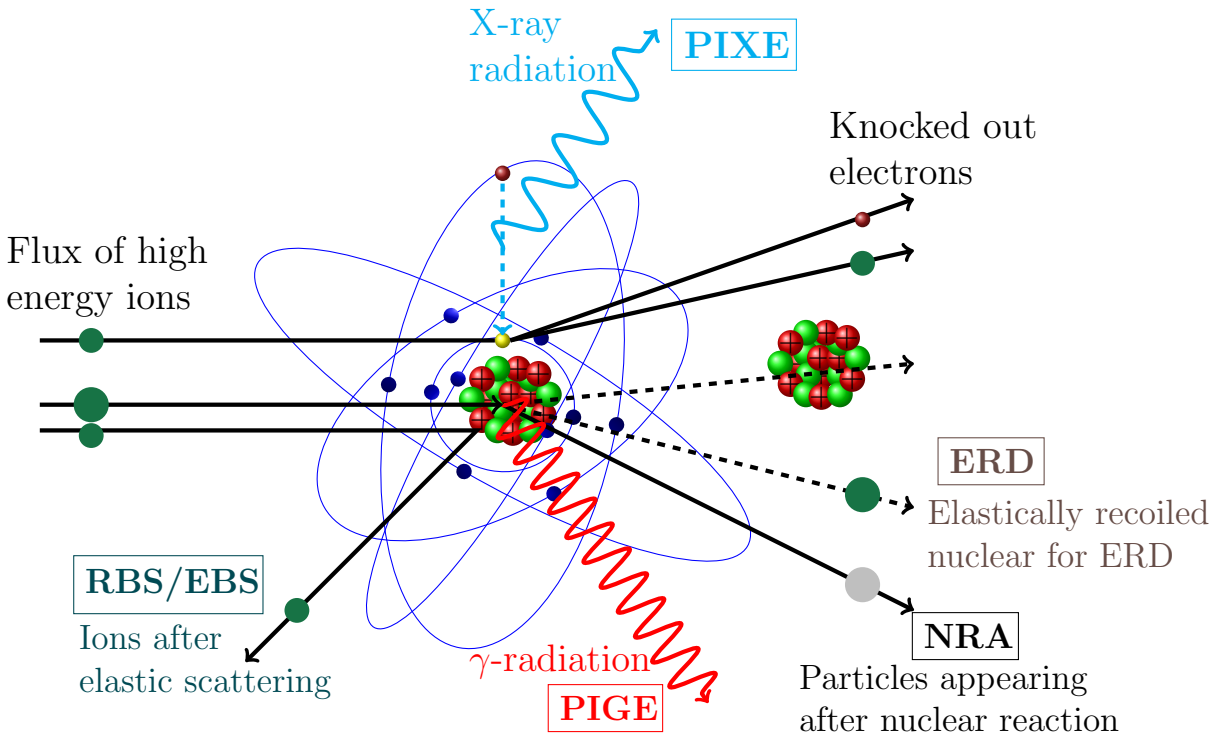

Figure 3.1: Schematic overview of the different methods of Ion Beam Analysis and the underlying interactions.

excess energy in the form of X-rays, characterized by the fluorescence yield. An early but accessible presentation of the basic physics and applications of PIXE may be found in Ref [34].

The PIXE method can provide elemental composition measurements of a single homogeneous thin layer or multiple homogeneous thin layers. For the most accurate analysis, fluorescence of lower Z elements by characteristic X-rays from higher Z elements must be taken into account during spectrum interpretation. PIXE can provide some indication of the depth distribution of the element in the analyzed objects by means of K_α/K_β or L_α/L_β ratios of characteristic X-rays [35], or by using multiple irradiation angles or energies. However, PIXE cannot measure concentration depth profiles of material as accurately as NRA and EBS methods presented below, since the observed characteristic X-ray yield from the sample is generated over a large range of depths, and the characteristic X-ray energy is independent of depth [36].

PIXE can be very sensitive, with detection limits near 1ppm under favorable conditions, and is multi-elemental since characteristic X-rays from many target elements can be present in a single spectrum. The typical analysed thickness is 10-30 μm.

3.2.2 RBS method: $A(a,\underline{a})A$

The most widely known IBA method is RBS, which is based on the detection of the charged (usually alpha) particles elastically scattered by the nuclei of the sample. The interaction is fully described by the analytical Rutherford cross section (Eq. 2.11), with small and well-known electron screening corrections, and established reaction kinematics, where the ratio K of the energy of the scattered particle to that of the incident particle is given in the laboratory frame by Eq. 3.2

$$K = \frac{M_1^2}{(M_1+M_2)^2}\left\{\cos\theta \pm \left[\left(\frac{M_2}{M_1}\right)^2 - \sin^2\theta\right]^{\frac{1}{2}}\right\}^2 \tag{3.2}$$

Concentration depth profiles can be obtained from the RBS spectra, with a depth resolution of about 10 nm under routine experimental conditions, limited by the energy resolution of the charged particle detector, which is typically about 15 keV.

RBS is useful for near-surface layer analysis with analyzed depth up to 2 μm for 4 He ions and up to 20 μm for protons. It is ideal for depth-profiling of heavy elements on lighter substrates because the cross section for the heavy element is high due to the Z_2^2 dependence, and the scattered alpha energy is high, leading to an intense isolated signal. Of course, the opposing case of light elements on heavy substrates is unfavorable because now, the cross section for the element of interest is low, and the scattered particle is at low energy such that the corresponding peak is of small intensity on a large background from the thick heavy target.

In favorable cases, RBS can measure sub-monolayer coverages of a heavy element on a light substrate.

3.2.3 EBS method $A(a,\underline{a})A$

At high enough energies and for light enough targets, scattering can remain elastic (internal nuclear states are not excited) while the cross section starts to deviate from the Rutherford value (the nuclear force starts contributing to the scattering). Table 3.1 the incident energies for which 165° alpha elastic scattering cross section first deviates by more 5% from the Rutherford cross section for a selection of elements up to Z=14(Si). For example, the alpha particle elastic backscattering cross section deviates more than 5% from the Rutherford cross section above 1.5 MeV for a boron target, and above 2.5 MeV for a neon target. This can provide useful analytical characteristics, such as enhanced cross sections or strongly resonant cross section structure that can be exploited.

EBS provides a useful alternative to NRA for light element analysis, in particular when deuteron beams cannot be used because of the strong radioprotection requirements. For accurate analysis, evaluated differential cross sections from the literature (or IBANDL [1])

Table 3.1: The incident energies for which 165° alpha elastic scattering cross section first deviates

	Nuclei	Energy (MeV)
1	Boron	1.5
2	Carbon	2.14
3	Nitrogen	2.15
4	Oxygen	2.35
5	Fluorine	<2
6	Neon20	2.47
7	Sodium	> 3
8	Mg	> 3
9	Al	> 4
10	Si	3.9

are needed. Since EBS is most useful for light elements (where significant deviations from the Rutherford cross section can occur), it is also subject to the same limitation of RBS, that the relevant signals are often sitting on the background from a heavy substrate, although in the case of EBS the cross section for the light element may be substantially greater than the Rutherford cross section. In the case where there are a number of light elements in the target, significant overlap can also occur.

3.2.4 ERDA method $a(A,\underline{a})A$

When an ion impacts an atomic nucleus in the target, the nucleus recoils. This recoiled particle can also be detected and used for analysis. The method is then termed Elastic Recoil Detection Analysis (ERDA). The best conditions are obtained when the recoiled ion is lighter than the incident particle, and is detected at forward scattering angles, and so for thick targets grazing incident and recoil angles are used. With alpha particle beams of up to a few MeV hydrogen and its isotopes can be detected, and depth profiled with similar performance to that of RBS just using a semiconductor particle detector and so ERDA for hydrogen is easily implemented in small IBA facilities such as that at VDGT and SAFIR. If a heavier beam is used (Heavy Ion ERDA), at energies of 10 or more MeV, heavier elements can recoil with energies useful for analysis [37]. In this case, more elaborate detection systems employing time of flight and gas ionization detectors are required. The advantage is that the method allows interference-free depth profiling of elements lighter than the incident beam.

ERDA is excellent for depth-profiling of very light elements in thin films (for very small depths ¡ 1 μm), but for profiling elements heavier than hydrogen, it is necessary to have high energy heavy ions, implying larger and more complicated facilities.

3.2.5 PIGE method $A(a,\underline{\gamma})B$

Particle-Induced Gamma-ray Emission (PIGE) can be considered a subcategory of nuclear reaction analysis when the reaction products are prompt gamma rays. Since the early 1960s, this technique has been utilized for a variety of applications, including analysis of fission reactor materials, cultural heritage, environment, and fusion reactor materials. This technique has the potential for depth profiling certain isotopes, with higher resolution than the other IBA methods [38].

The PIGE technique is a nondestructive, analytical procedure for quantifying elements in solid surfaces. Because of the increasing Coulomb barrier with atomic number, this technique is more appropriate for light elements than heavy ones.

The most important aspect of PIGE can be defined as: a) Provide better resolution of depth profiling information than other IBA techniques for some isotopes, b) Highly isotope specific, c) Detect many nuclides, d) The achievability of simultaneous measurement of multiple light elements in heavy matrixes [39].

PIGE can be very sensitive in certain cases, but the PIGE cross sections vary considerably from isotope to isotope and from element to element, and so general comments about sensitivity cannot be made.

3.2.6 NRA method $A(a,\underline{b})B$

Nuclear Reaction Analysis (NRA) is the IBA method of choice for determining concentration depth distributions of light elements in a heavy matrix and can provide high-resolution depth profiling of specific isotopes. In the energy range of small accelerators (up to a few MeV) nuclear reactions can be induced by all of the light ion beams (^{1}H, ^{2}H, ^{3}He, ^{4}He) with different general characteristics as summarized below:

- Alpha: Very few elements have positive Q-values (^{10,11}B, ^{19}F, ^{23}Na, ^{27}Al, ^{31}P, ^{35}Cl) thus the background is strongly reduced. Cross sections are high enough only at high beam energies.

- Proton: Reactions exist with low Q-value (^{6}Li, ^{9}Be, ^{10}B, ^{27}Al) and high Q-value (^{7}Li,^{11}B, ^{18}O, ^{19}F, ^{23}Na, ^{31}P). A number of cross sections (^{27}Al(p,γ), ^{18}O(p,α), ^{19}F(p,$\alpha\gamma$)...) have very fine structure – narrow resonances – that allow depth profiling with near nanometric depth resolution (ref).

- Deuteron: (d,p) and (d,α): Almost all light isotopes have high positive Q-values. Cross sections are high enough to be used for analysis with quite low beam energies, often below 1 MeV.

In NRA, deuterium is a desirable projectile option in nuclear reactions because 1) it allows simultaneous analysis of many light elements such as oxygen, boron, and alu-

minium in the composition of complex targets; 2) deuterium-induced nuclear reactions often have large cross-sections which can increase the sensitivity and accuracy of analysis; 3) amongst the nuclear reactions that may be exploited, those induced by deuterium beams are particularly rich since the proton and the neutron are weakly bound and the uncharged neutron is not repelled by the nuclear charge. There is no Coulomb barrier for the neutron.

Despite these considerable advantages, NRA with deuterium beams is much less widely used than RBS. The main reasons for this are 1) strong radiation safety precautions are mandatory because the (d,n) reaction channel is almost always open, and 2) NRA cross-sections cannot be accurately calculated analytically, being highly variable with incident particle energy, scattering angle, and the nature of the reacting nucleus. The existing databases of NRA cross sections are far from complete and further development of NRA requires new data for developing nuclear reaction models, determining model parameters, and providing recommended cross sections for use in NRA.

3.3 Experimental aspects to measurement the cross section for IBA

3.3.1 Introduction

Accurate differential cross-section determination is dependent on the accuracy of recordings and measurements performed in the laboratory. The accuracy of these measurements depends on consideration of a number of parameters, including (i) a well-calibrated accelerator energy scale, E, (ii) efficiency and solid angle calibration of the detector, (iii) target preparation (iv) incident ion beam charge collection and integration, (v) a precisely known detection angle, θ, (vi) Adequate dead-time correction.

Proper design is very important for accurate cross-section measurement for use in IBA and other applications. For example, the solid angle and detector used for RBS should be different from that used for NRA. The experimental steps and works to measure the cross section for IBA are as follows: The first step is to calibrate the accelerator's energy. The second step is to select and create a suitable thin sample and its characteristics. The third step is to calibrate the detector by selecting the appropriate reference target to eliminate the effect of uncertainties in current integration and solid angle of the detector. The fourth step is to design and perform experiments taking into account uncertainties and calculating them. The fifth step is to evaluate the obtained data by comparing it with the existing data in the literature and/or theoretical models and the final step is to benchmark the cross section with particle spectra obtained from a thick target.

In this thesis, considerable effort has been made to accurately calibrate the accelerator

energies in the two labs, and this is described in detail below. The preparation of the thin self-supporting Al targets and the thermal $Si^{17}O_2$ targets are also described below. The accurate determination of detector solid angle and efficiency, and incident beam charge integration can be avoided by the use of internal standards built into the target. This is the case for the ^{27}Al(d,p&α) cross sections, where a thin gold or silver layer for which elastic scattering is known to be Rutherford acts as the internal standard. This is fully described in chapter 4. The measures taken to minimize uncertainties on the ^{17}O(p,p) cross section measurements are described in chapter 5.

3.3.2 Energy calibration of Accelerators

The accelerator energy is deduced from the reading of a quantity that is presumed to be related to (and often proportional to) the energy – for example the voltage generated by the Generating VoltMeter (GVM), or the magnetic field of a bending magnet, determined from a nuclear magnetic resonance (NMR) or Hall Effect meter. The energy calibration of the accelerator consists in finding the constant of proportionality (or constants in the case of a polynomial dependence) between the measured value and the accelerator energy.

Calibration of the GVM is a calibration of the terminal potential, and so is valid for all beamlines, and is independent of the magnetic field in the analyzing and any steering magnets. The desired beam energy is adjusted with respect to the GVM reading, and the analyzing magnet field is simply adjusted to optimize transmission through the beamline. Determining the accelerator beam energy from the magnetic field of the analyzing magnet is the inverse process: the magnetic field is adjusted to give the required energy in the appropriate beamline, and the terminal potential is adjusted to optimize beam transmission. Since the magnetic field for a given beam species and energy depends on the deflection angle, it is necessary to calibrate the magnetic field for each beamline (i.e. deflection angle) since beamline angles are rarely known with very high precision.

The relationship between the beam energy and the frequency f of the NMR meter may be derived as follows. The force exerted on a charged particle by mass m and velocity V in the radius of motion R in the magnetic field B is obtained from Eq. 3.3. In a Van de Graaff accelerator, the energy of a beam line is regulated by the intensity of the magnetic field, and the intensity of the magnetic field is measured by the Nucleus Magnetic Resonance (NMR) frequency of hydrogen. Here the goal is to find the constant ratio, (k NMR in Eq. 3.4), between the projectile energy and NMR frequency.

$$qVb = \frac{mV^2}{R} \Longrightarrow q^2B^2 = \frac{(mV)^2}{R^2} \Longrightarrow E = \frac{(qBR)^2}{2m} \tag{3.3}$$

Since B is proportional to $f : B^2 = k' f^2$, we obtain

$$E = q^2 \frac{R^2}{2m} \times k' f^2 \Longrightarrow E = k_{NMR} f^2 \tag{3.4}$$

For the GVM, the energy E of a singly charged ion is proportional to the voltage V_{VGM} given by the $GVM : E = k_{VGM} V_{VGM}$, and energy calibration consists in determining k_{VGM} .

In the work presented in this thesis, the accelerator energy was calibrated with respect to the GVM voltage in Paris and with respect to the analyzing magnet field in Tehran. As will be shown below, these two entirely different calibration approaches gave essentially identical energy dependencies of the cross sections measured in the two labs.

In either case, it is necessary to be able to determine the beam energy by a method independent of the GVM or analyzing magnet field measurement. This is usually through the use of nuclear reaction or elastic scattering cross sections with features (thresholds, resonances,...) at well-known energies.

There are three main techniques for energy calibration of the accelerator include 1) neutron producing threshold reactions of (p,n) or (α,n), 2) using narrow gamma-ray resonances induced by low-energy protons beams up to 6 MeV, and by alpha and deuterium beam for higher energy up to 60 MeV and 3) elastic scattering. Among them, methods 1 and 2 are used most commonly, and were the methods used in this thesis. These are described in detail in sections 3.3.2.1 and 3.3.2.2 below and employed in sections 4.3 and 5.3 for experimental setup of measurements. The elastic scattering method is briefly presented, but we don't use this method in this thesis.

3.3.2.1 Neutron producing threshold reactions (Using in VDGT)

The base of this method is that neutron-producing threshold reactions do not produce any neutrons when the energy of the proton beam is lower than the threshold energy. A thick target including the neutron producing nucleus such as LiF and a neutron detector such as BF_3 are required for the measurement [18,40]. It is necessary to know and choose the proper reactions, thick targets and to measure the neutron production as the proton energy is scanned from below to above the threshold. The most well-known reactions used in this method are shown in Table 3.2.

In VDGT lab in Tehran, Iran, the experimental work was carried out on the 30° left beamline of the 3 MV Van de Graaff electrostatic accelerator in Tehran with an energy resolution estimated to be about 0.1% [57]. The beam energy calibration of accelerator was performed using the 1880.44 ± 0.02 keV threshold energy of ^{7}Li(p,n)^{7}Be reaction [58]. The target used for these measurements was a LiF pellet which was prepared by pressing LiF powder in a hydraulic press. A 10nm layer of Ag was then deposited onto the pellet by using a vacuum evaporation system. (Shown in Figure 3.2)

Table 3.2: Common reactions used in accelerator energy calibration for method neutron producing threshold reactions. The red entry is the one used for this thesis.

Reactions	**Ion Energy (keV)**	**Resonance natural width (keV)**	**Detected radiation**	**Reference**
^{12}C(p,n)^{12} C	14230.75±0.02	1.2	n, threshold	[41]
^{13}C(p,n)^{13}N	3235.48±0.29	-	n, threshold	[42]
^{13}C(p,n)^{13}N	3235.7±0.07	-	n, threshold	[41]
^{13}C(p,n)^{14}N	1746.9	0.075	n, threshold	[43]
^{7}Li(p,n)^{7}Be	1880.36±0.08	-	n, threshold	[42]
^{7}Li(p,n)^{7}Be	1880.44±0.02	-	n, threshold	[41]
^{27}Al(p,n)^{27}Si	5803.3±0.26	-	n, threshold	[41]
^{19}F(p,n)^{19}Ne	4234.3±0.8	-	n, threshold	[41]
^{15}N(p,n)^{15}O	3774.05±0.52	-	n, threshold	[42]
^{11}B(p,n)^{11}C	3016.99±0.07	-	n, threshold	[42]
^{3}H(p,n)^{3}He	1018.8751±0.0015	-	n, threshold	[42]

Table 3.3: Common reactions used in accelerator energy calibration for method narrow resonances. The red entries are those used in this thesis.

Reactions	Ion Energy (keV)	Resonance natural width (keV)	Detected radiation	Reference
^{27}Al(p, γ)^{28}Si	1799.75±0.09	<0.200	γ	[44]
^{27}Al(p, γ)^{28}Si	1587.49±0.08	<0.200	γ	[44]
^{27}Al(p, γ)^{28}Si	1316.87±0.03	0.070±0.035	γ	[45, 46]
^{27}Al(p,γ)^{28}Si	991.88±0.04	0.10±0.02	γ	[41]
^{27}Al(p, γ)^{28}Si	991.9	0.1	γ	[47]
^{27}Al(p, γ)^{28}Si	991.756±0.017	0.100±0.015	γ	[45, 46]
^{27}Al(p, γ)^{28}Si	632.23±0.04	0.0048±0.0004	γ	[44, 45]
^{19}F (p,$\alpha\gamma$)^{16}O	340.46±0.04	2.34±0.04	γ	[48]
^{19}F(p,α)^{16}O	340.46±0.04	2.34±0.04	γ	[41]
^{13}C(p, γ)^{14}N	1746.618±0.017	0.135±0.008	γ	[49, 50]
^{13}C(p,γ)^{14}N	1747.6±0.9	0.077±0.012	γ	[41]
^{13}C(p,γ)^{14}N	1747.6±0.9	0.075±0.005	γ	[51]
^{14}N(p,p'γ)^{14}N	5937	17	γ	[52]
^{32}S(p,p'γ)^{32}S	3379	1.2	γ	[53]
^{27}Al(p,$\alpha\gamma$)^{27}Al	1683.57	0.2	γ	[41]
^{19}F(p,$\alpha\gamma$)^{16}O	872.88±0.2	4.7±0.2	γ	[41]
^{15}N(p,$\alpha\gamma$)^{12}C	429.57±0.09	0.103±0.011	γ	[54]
^{11}B(p,γ)^{12}C	163.1±0.4	5.3±1.0	γ	[55, 56]

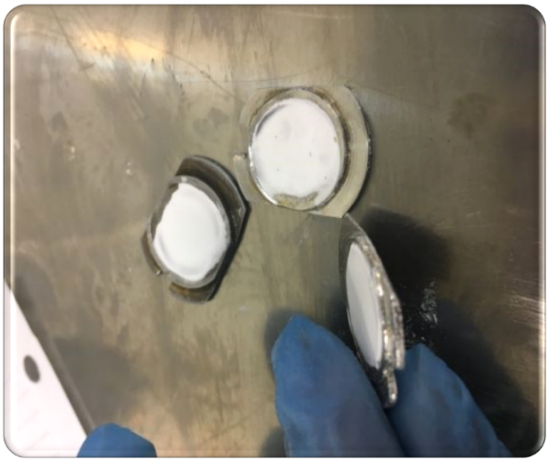

(a)

(b)

Figure 3.2: a) Create a thick layer of LiF (pellet) by hydraulic press, b) Thin layer of Ag coated on LiF by PVD method (VDGT)

Detector BF_3 model LND-INC-202 with a length of 26 cm and a diameter of 2.5 cm behind the Faraday cup of the reaction chamber with an angle of zero degrees to the incident beam was used to detect neutrons. Between the target and the detector, 5 cm thick polyethylene bricks were used to moderate the fast neutrons produced by ^{7}Li(p,n)^{7}Be to thermal neutrons which are detected in the BF 3 detector, where the thermal neutrons react with ^{10}B to produce an alpha particle. Two groups of alpha particles with energies of 1.47 MeV and 1.776 MeV are recorded in the detector [48].

$$\mathrm{p} + {}^{7}\mathrm{Li} \longrightarrow {}^{7}\mathrm{Be} + \mathrm{n} + \mathrm{Q}\ (1.644\ \mathrm{MeV}) \tag{3.5}$$

$$\mathrm{n} + {}^{10}\mathrm{B} \begin{cases} \nearrow\ {}^{7}\mathrm{Li} + {}^{4}\mathrm{He} + \mathrm{Q}\ (2.78\ \mathrm{MeV}) \\ \searrow\ {}^{7}\mathrm{Li} + {}^{4}\mathrm{He} + \mathrm{Q}\ (2.3\ \mathrm{MeV}) \end{cases} \tag{3.6}$$

For the experimental part, the incident proton beam should start from the energy above the energy threshold of the neutron, about 1900 keV, the frequency should be reduced by interval 0.01Hz, equivalent to 2keV, until the number of neutrons is equivalent to the background level. In each step, the curve of $(\mathrm{yield})^{(2/3)}$ versus NMR frequency is plotted shown in Figure 3.3, because the $(\mathrm{yield})^{(2/3)}$ is distinctly more linear than the $(\mathrm{yield})^{1}$, and the extrapolation procedure seems sufficiently accurate. Finally, the energy frequency of the reaction threshold ^{7}Li(p,n)^{7}Be is the intersection of the fitted lines of $(\mathrm{yield})^{(2/3)}$ and background. With Eq. 3.4 the calibrated constant k is calculated in Eq. 3.5.

$$Y_n = N_p \times N_{Li} \times \Delta\Omega(\frac{d\sigma}{d\Omega})_{(p,n)} = \frac{\text{Neutron flux}(BF_3)}{\text{particle} \times \text{sr}} \tag{3.7}$$

$$f = 12.32,\ E = 1880.44 \Longrightarrow K = \frac{E}{f^2} = 12.387 \tag{3.8}$$

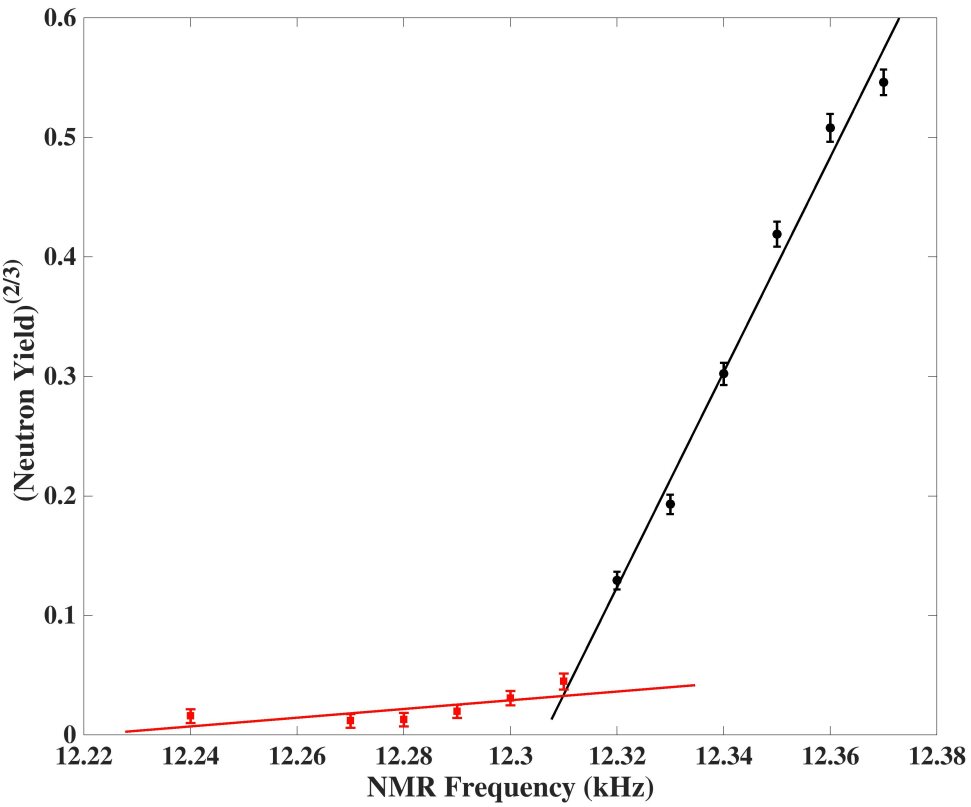

Figure 3.3: The curve of $(\text{yield})^{2/3}$ versus NMR frequency for the ^{7}Li(p,n)^{7}Be threshold reaction.

3.3.2.2 Narrow resonances (Using in INSP lab)

One of the most precise and user-friendly methods of calibration employs gamma-ray reactions with the proton incident beam. A list of commonly used resonances is also shown in Table 3.2. Usually, a thick sample containing the target nucleus is used. The yield curve obtained, usually that of a (p,γ) reaction with the gammas detected in a NaI or HPGe detector [18, 40, 52], as the beam energy is scanned across the resonance energy, then consists in a step, with the step half-height being the resonance energy. For particle energies below 2 MeV, well-defined narrow and strong resonances are shown in Table 3.3.

In INSP lab in Paris , the energy of the accelerator was read by the GVM signal and calibrated by utilizing the narrow nuclear resonances of the ^{15}N(p,$\alpha\gamma$)^{12}C reaction at 429.57 keV, the ^{27}Al (p, γ)^{28}Si reaction at 991.88 keV, and the ^{13}C(p,γ) ^{14}N reaction at 1747.6 keV. The gamma rays were detected by a BGO scintillation detector at 0° [59, 60]. For fitting the excitation curves, the SPACES code was used, because of the high resolution of the beam energy [61].

The resonance energy is measured in several steps: (a) finding the approximate value

using the thick target of Al and (b) finding the exact resonance energies by using several thin targets in the resonant energy range of the previous section. The experimental steps are described below.

First of all, the approximate GVM reading corresponding to the 429.57 keV resonance energy was quickly found using a 500-nm thick target of aluminum, with a current of I=500 nA, a beam diameter of 2mm and $1\mu C$ integrated charge. This initial prediction of resonance energy is not highly accurate since the surface is oxidized and possibly dirty, but the thick target, with high yield and a clear 'below' and 'above' resonance yield gives a rapid initial approach to the resonance energy which facilitates the use of thin targets for the subsequent measurements.

1. To increase the precision of the experiment, a 50 nm-thickness of aluminum is deposited on carbon. A current of I=500 nA, and a beam size of 2 nm was employed for finding the resonance energy of the ^{27}Al(p,γ)^{28}Si reaction with high precision.

2. For the ^{15}N(p,$\alpha\gamma$)^{12}C resonance at 429.57 keV, we used a Si_3N_4 target grown with ^{15}N by Chemical Vapour Deposition (CVD) on silicon. This resonance is very intense and a beam current of I=100 nA was adequate.

3. For the ^{13}C(p,γ)^{14}N resonance at 1747.6 keV, which is also very intense, we used an amorphous ^{13}C film deposited onto Si by to plasma deposition and a beam current of I=100nA was sufficient.

Finally, The SPACES code is used to simulate all of the excitation curves, to properly take into account the influence of the statistical nature of the energy loss on the form of the excitation curves.

3.3.2.3 Elastic and inelastic scattering

For higher energies, finding well-measured nuclear cross sections is hard but we could use non-resonant nuclear reactions with nearly any energy to calibrate the accelerator based on elastic and inelastic scattering. The basis of the non-resonant nuclear reaction calibration (NRC) technique is measurement of elastically scattered particles with two different masses but accelerated to the same potential, and nuclear reactions with positive Q-value. The accelerator energy can then be deduced from kinematics. The experimental requirements are modest, with just a multichannel Analyzer, a Silicon PIN diode or a Si surface barrier (SSB) detector and a polished target. The accuracy of this method however depends on the charged particle detector energy calibration, the uncertainty in the scattering angle, and the energy resolution of the detector and is lower than the previous two methods [62, 63].

In this thesis, only the methods (1) and (2) are used for energy calibration respectively in the VDGT lab in Tehran and INSP lab in Paris.

3.3.3 Target Preparation

The proper target preparation is one of the most important aspects of achieving accurate nuclear physics experiments for IBA and measuring the cross sections. The target must conform to the requirement in respect of thickness, composition, purity, roughness, and stability under the beam irradiation in considered situations. Practically all of the thin film preparation methods have been applied for production of targets specifically for nuclear reaction measurements, and for thick targets, in addition to sourcing pure bulk materials, pressed targets of powdered materials have been widely used. Details specific to nuclear target preparation by ion beam sputtering, mechanical rolling and electrophoresis are given in [64, 65]. Heavy-ion beam sputtering (HIBS) and electron beam evaporation/condensation making sample techniques for high-resolution nuclear spectroscopy are described in [65], and a filtration technique of hydroxide precipitates with a porous Al_2O_3 membrane filter for precious materials and radioactive materials with low contamination is given in [66–68].

In the context of this thesis, we noted that self-supported Al films can be prepared by vacuum evaporation [69, 70], and our method is described in section 3.3.3.2. We also applied vacuum evaporation for Au and Ag thin film deposition, and thermal oxidation for the preparation of $Si^{17}O_2$ films on silicon.

3.3.3.1 Preparation of reference targets for RBS and NRA measurements

In addition to the obvious requirement that the composition and thickness of the reference target be known with sufficient precision, further requirements for an acceptable reference target include: 1) The proper layer thickness, sufficiently thin for small enough energy loss of the incident beam in passing this layer and sufficiently thick to give reasonable counting rates for yield. 2) A high lateral uniformity (at least 1 cm^2) for increased lifetime of the reference targets, 3) amorphous structure to reduce channeling effects, 4) stability both under ion bombardment and during storage in the atmosphere [71].

Methods to produce reference targets, depending on the kind of material, include :1) Thin solid films of Al, B, C, Be, Si and other low-Z nuclei which can be made with following techniques: a) Vacuum evaporation, b) reactive cathodic sputtering, c) plasma and ion beam assisted deposition, d) chemically reactive vapour deposition (CVD), e) electrochemical techniques. 2) Ion -implanted targets for the noble gases is the only method for making reference target, 3) Frozen gas targets have been used for high precision measurements of several nuclear reaction cross sections at a limited number of energies [64–71].

For calibrated RBS spectra, a single thin film of a high Z element, of precisely known areal mass density on a light element target is sufficient as a reference for a simple scaling factor related to beam current integration and detector solid angle, applicable to all

samples. The ratio of differential scattering cross sections of this reference nucleus target and unknown sample can be calculated analytically from the Rutherford scattering cross section, taking care to consider electron screening effects for high Z nuclei and deviations from Rutherford scattering due to nuclear interaction, for 4 He scattering on low Z nuclei. At the usual backscattering angle near 165°, screening corrections are less than 1% for elements up to about Z=70 [72] and the alpha particle elastic scattering cross section is within 1% of Rutherford for ^{12}C up to about 1.9 MeV, ^{14}N up to about 1.7 MeV, and ^{16}O up to 2.3 MeV [1]. In this Thesis, an RBS reference target of Bi implanted into Si, traceable to [73], was used. The uncertainty in the areal density of Bi is estimated to be less than 2%.

On the other hand, for calibrated NRA spectra, precisely known reference targets are necessary for each isotope since there are no general formulae for the reaction cross sections for each isotope, and the cross sections can vary strongly with incident particle energy and with detection angle. Ideally, for NRA, a heavy substrate is desirable so that there are no interfering nuclear reactions from the substrate itself. Depending on the isotopes, their availability and physical form, various sample preparation methods need to be considered. In this thesis we have used anodic oxides of Ta for ^{16}O and ^{18}O reference targets [74, 75]. Water highly enriched in ^{17}O is not available and so the electrochemical method used to prepare the ^{16}O and ^{18}O standards cannot be applied here. We therefore explored the use of thermal oxides on Si, for which ellipsometry can provide a precise estimate of the oxide thickness and density, for ^{17}O reference samples, as described in section 3.3.3.3. This indeed proved to be successful and could also be a new method to produce ^{16}O and ^{17}O standards for NRA methods in which there are no interferences from nuclear reactions with the silicon substrate.

3.3.3.2 Al preparation for measurement the cross section of ^{27}Al(d, α) and ^{27}Al(d,p)

A technique for the preparation of thin self-supporting metallic films has been developed in Ref [76] with the evaporation of aluminum onto a microscope slide which had formerly been dipped into a detergent solution under ultra-sonic agitation. After careful drying with a warm air flow, aluminum was evaporated onto the prepared slides by physical vapor deposition (PVD model VE-770, VDGT). Through immersion in water, the obtained film can be floated from the slide onto the water, and then fished over the hole in a thin metal sheet. A thin Ag layer is then evaporated onto the self-supporting Al film. All the procedures of Al-target preparation and deposition of Ag onto it as an internal reference in the VDGT lab in Iran are shown in Figure 3.4 and Figure 3.5 in order. A similar method was employed at INSP in France for the preparation of the thin self-supporting Au/Al-targets. An EDWARDS FL 400 for Al and VINCI technologies PVD 4E for Au evaporation were used and shown in Figure 3.6 and Figure 3.7 respectively [2].

Figure 3.4: Preparation of a thin self-supporting vacuum evaporated Al film (VDGT)

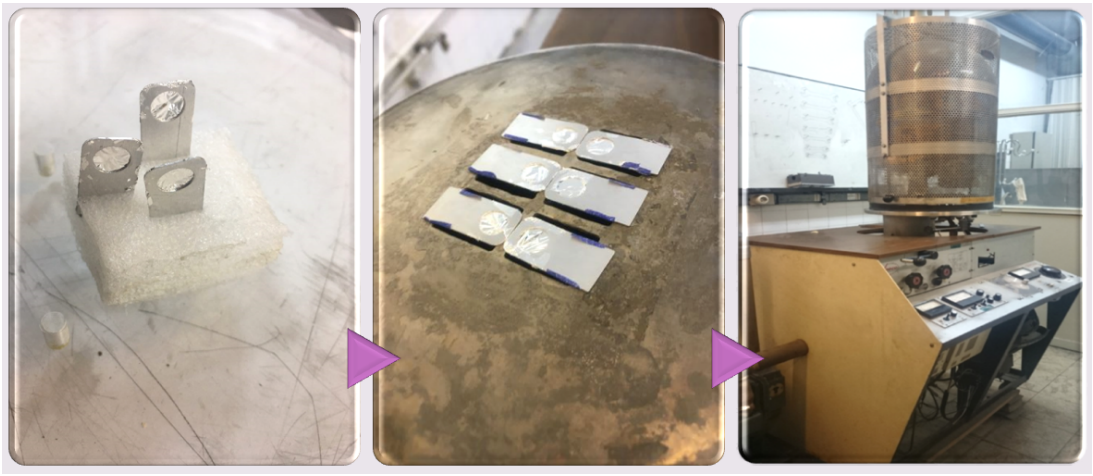

Figure 3.5: About 100nm of Ag was deposited onto the thin self-supporting vacuum evaporated Al films, as an internal reference (VDGT).

3.3.3.3 ^{17}O Sample preparation and characterization for EBS measurement of ^{17}O(p,p) reaction

Silica layers were grown on 100 oriented silicon wafers, thicknesses ranging from 355-405 μm, by thermal oxidation at 1100 °C in a $^{17}O_2$ gas in a quartz tube vacuum furnace with the base pressure of 10-6 mbar (Shown in Figure 3.8).

The total physical thickness and refractive index of the silica layers were measured by ellipsometry (Shown in Figure 3.9). The refractive index at 633 nm varied slightly between 1.47 and 1.48, and the refractive index of fused silica is 1.46. The atomic thickness was measured by RBS with a precision of 2%. The Ellipsometry and RBS thicknesses were consistent with the bulk thermal silica density of 2.21 g/cm^3 .

The small quantities of ^{18}O and ^{16}O, present as impurities in the highly enriched $^{17}O_2$ gas used to grow these films was determined by the established NRA techniques using the ^{18}O(p,α)^{15}N and ^{16}O(d, p_1)^{17}O nuclear reactions at the SAFIR platform at INSP. Absolute values of the areal densities ^{16}O and ^{18}O were specified by comparing with standard SiO_2 references with an uncertainty of 2%–3% [77, 78].

It is largely supposed in the literature that apart from a monolayer region near the

Figure 3.6: a) Outside and b) inside of the EDWARDS FL 400 for Al evaporation (INSP)

SiO_2/Si interface, thermally grown SiO_2 on Si is stoichiometric, however we could find no definitive work demonstrating this. Since this assumption underlies the determination of the ^{17}O content of the thermal silica layer, we present here the arguments that lead us to assume that the thermal silica is indeed very close to stoichiometric composition.

Firstly, of course, SiO_2 is the thermodynamically stable compound when silicon is exposed to O_2 gas, and at 1100°C the reaction rates are well known – our oxidation process indeed followed the kinetics given many decades ago in [79]. Secondly, so far as we can find, there is no evidence in the vast literature on the thermal oxidation of silicon, that the silica film prepared by oxidation of silicon in pure oxygen is NOT stoichiometric. Indeed, the whole of reference [80], which includes chapters from many experts on the thermal oxidation of silicon, assumes this.

We have therefore tried to conceive how the thermal oxide of silicon may indeed be non-stoichiometric. Sub stoichiometric silicon oxides – only available as powders - are either in fact mixtures of Si and SiO_2 particles (a stoichiometric mix of Si and SiO_2

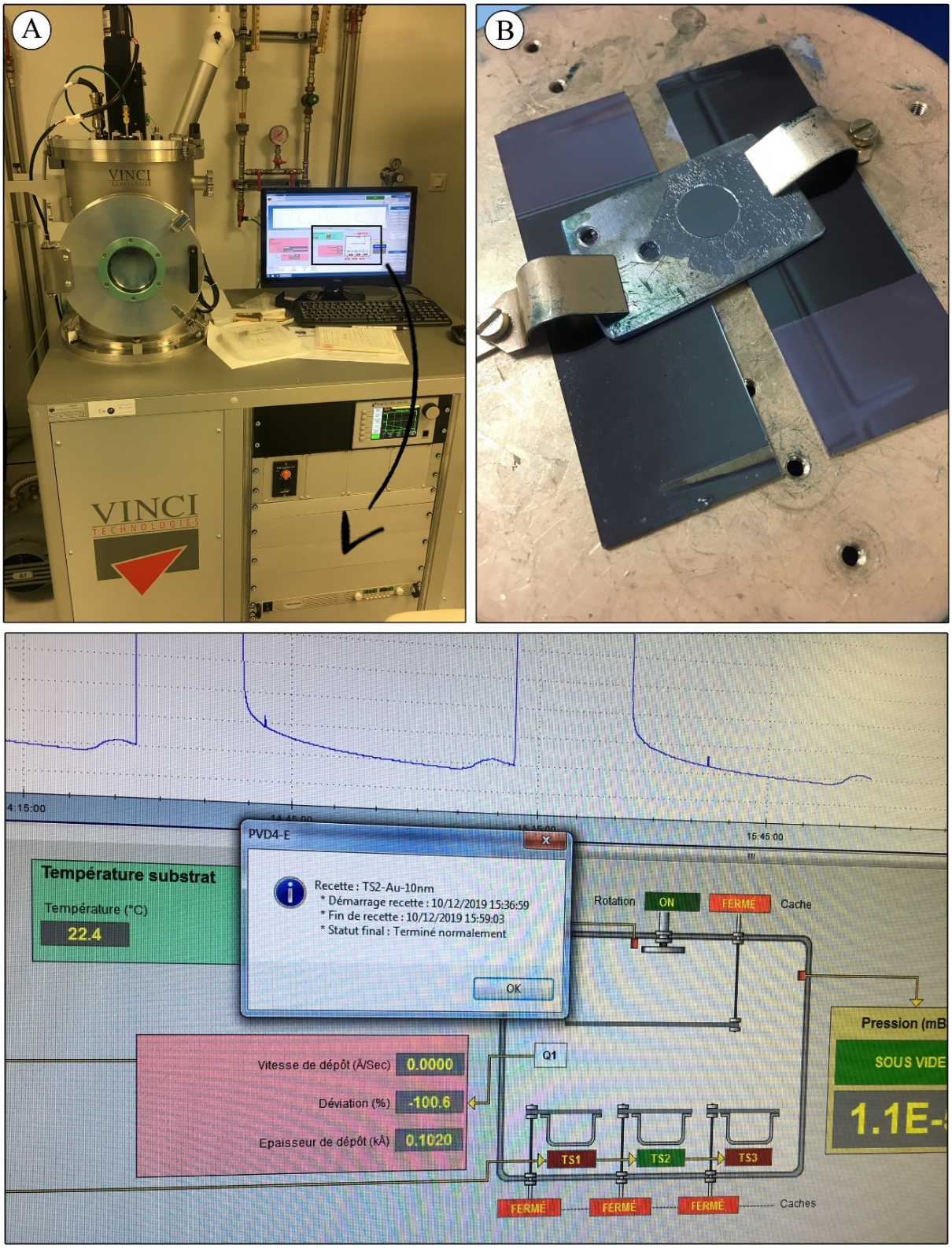

Figure 3.7: The VINCI technologies PVD 4E for Au evaporation (INSP)(a) and the sample mounting arrangement (b).

would give an overall composition of SiO), or stoichiometric SiO [81]. Solid SiO, which can only be prepared under very constrained reducing conditions, is thermodynamically

Figure 3.8: Quartz tube furnace equipped for handling isotopically enriched gases, used for ^{17}O thermal oxide growth on silicon (INSP).

unstable at all temperatures. At temperatures above 1000°C it rapidly and irreversibly disproportionate into Si and SiO_2 even in inert gasses. At room temperature and in air, the powder particle surfaces oxidise to SiO_2 forming a protective coating, like the protective native oxide of silicon. Clearly then, the thermal oxide of silicon formed in 200mb of pure oxygen at 1100°C cannot by any means be SiO.

We can also look back to some of the first reports of oxygen-deficient glasses [82]. Here it is claimed that some glasses that are prepared in the presence of carbon and in reducing atmospheres, may be 'slightly' oxygen deficient. The authors prepared such glasses, starting from pure stoichiometric silica, powdered and then mixed with some tens of ppm of Si and then reacted at 1850°C under reducing conditions, to produce glasses with controlled oxygen deficiency. We may note that only 70 ppm of silicon was used – producing a glass with only some tens of ppm deficiency in oxygen, which is the extent of oxygen deficiency expected in commercially made 'oxygen deficient' glasses.

We can also check to see whether it might be possible to have a substantial (e.g. several percent) concentration of oxygen vacancies in our silica layer. Some oxides, such as ZnO, are known to have large oxygen vacancy concentrations, certainly much higher than those in our silica. The oxygen vacancy concentration in ZnO ranges from about 10 ppm to 0.1%, which would be upper limits to the oxygen vacancy concentration in our silica film. Studies of the vacancy concentration in Germania-Silica glasses [83], materials

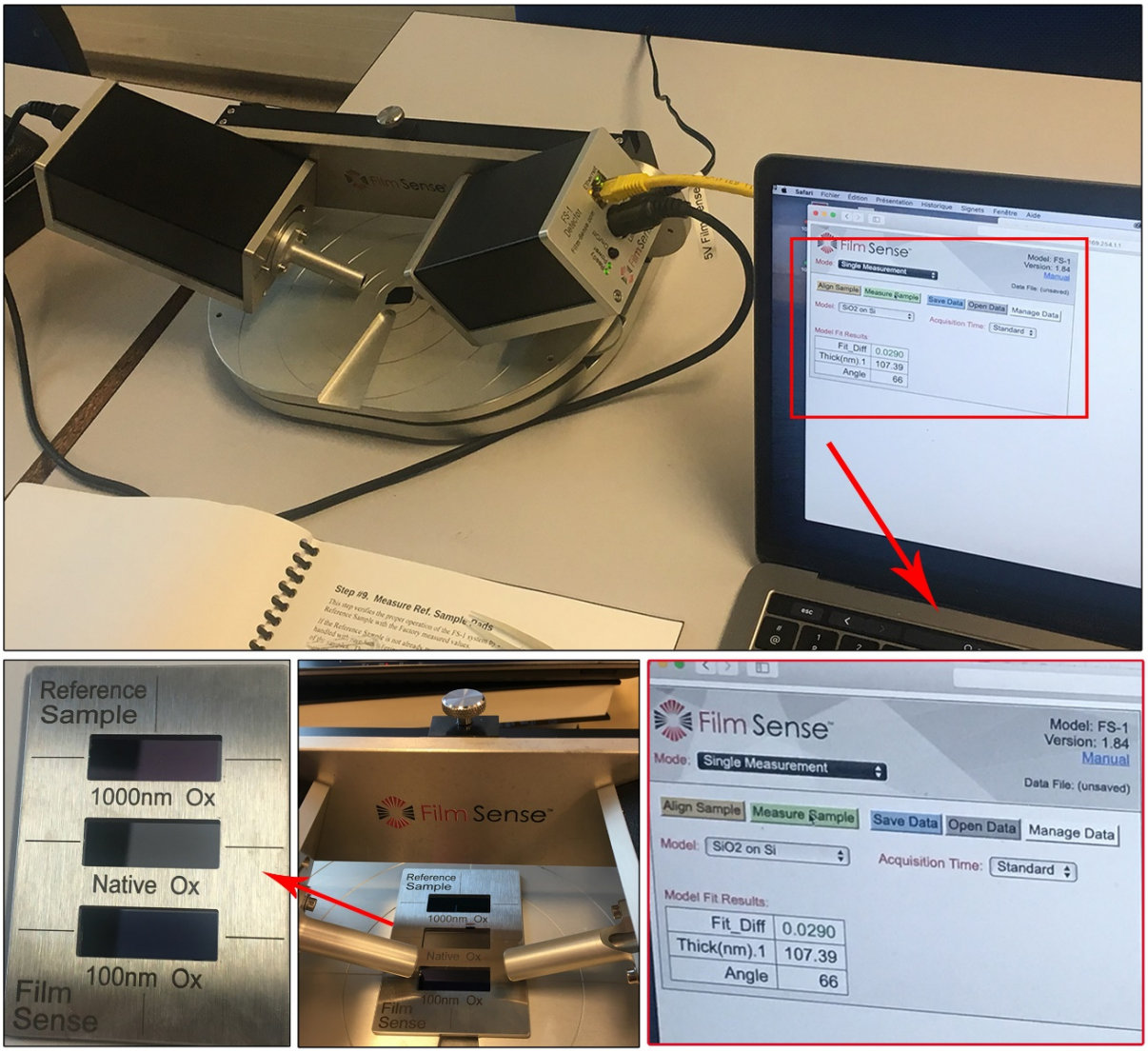

Figure 3.9: Measurement of thickness sample by Ellipsometry.

closer in properties and structure to the silica film we have produced, give values in the range of 100 ppm for 1100°C in O_2 gas.

Finally, perhaps we have a super-stoichiometric silica film, with a significant concentration of OH groups in the glass. This can occur if water is present (our thermal oxide is prepared under dry conditions). The water molecules in the glass are probably present in the form of vicinal OH groups (the H_2O molecule can break an Si-O-Si bond, to give two Si-OH bonds side by side [83]. This can be the case with silica films grown by deposition (e.g. sputtering, pulsed laser ablation ...). Thermal silica, though, contains much less than 1% of hydrogen (indeed we measured this directly in our thermal ^{17}O films by ERDA).

3.3.4 Evaluation and benchmarking of cross sections for IBA

We have followed the procedure proposed by the first technical meeting on 'Benchmarking Experiments for Ion Beam Analysis', held by the IAEA to deliberate on all the aspects related to the precision of assessed cross-section data sets [84].

Evaluation is the process of compiling, critically assessing, and parametrizing all of the experimentally measured cross section data. In some cases, data is reported without uncertainty estimates. When certainties are given, often different cross-section measurements for what should be an identical cross section show discrepancies greater than the estimated uncertainties. Also, some of the cross-sections have been measured without sufficient detail, especially those with fine structures. And finally, measurements from the same geometry as will be used for IBA measurements are the most useful because the cross section can depend strongly on the scattering angles. In some cases, slightly different angles can lead to different cross sections by a factor of 2 or even more [18]. The process of critical assessment includes searching for possible reasons for disagreements between measured cross sections and evaluating which cross section data should be retained for parametrization.

The parameterization of nuclear cross section data usually consists in optimizing adjustable free parameters in nuclear models so as to obtain an adjusted theoretical cross section that best embodies the measured cross section data and the theoretical knowledge that can be brought to bear. These cross sections are then referred to as evaluated cross sections. This semi-empirical approach can lead to justifiable extrapolations of the cross section in limited ranges beyond the angles and energies for which experimental data exist. In the case of the Al(d,p&α) cross sections studied in this thesis, the existence of many overlapping levels in the compound nucleus leads to Ericson fluctuations in the solutions of the wave equation for this scattering system, rendering impossible the establishment of a useful theoretical model. The level density is too high to allow an R-Matrix approach, but not yet sufficiently dense to justify the use of a statistical model. For this case, we have embodied the assessed experimental data in a Fourier series expansion. This provides optimal interpolation to give values of the cross section between the measured points but provides no basis for extrapolation.

Benchmarking consists of a further step to verify the fitness of the evaluated cross section for the purpose for which it is intended – in our case that of interpreting particle spectra obtained from bombarding a thick target. Benchmarking therefore usually consists in measuring thick target spectra under the best possible experimental conditions, from a perfectly characterized target, and comparing these to such spectra calculated using the best established simulation code and auxiliary data (such as stopping powers). Benchmarking also has a substantial contribution in designating and allocating logical uncertainties to the assessed differential cross section data [85].

Once satisfactorily benchmarked, a cross section may then be recommended. Many differential cross sections relevant to IBA have been measured and compiled in databases, of which the most widely used are IBANDL (Ion Beam Analysis Nuclear Data Library) and EXFOR at [1]. IBANDL also includes evaluated and recommended cross sections where they exist. For cross sections where suitable adjustable nuclear models exist, SigmaCalc, an online calculator [86] is available within IBANDL [1].

The ^{27}Al(d,p&α) cross sections are benchmarked as described in Chapter 4, however it has not been possible to make a thick homogeneous target fully, or even just highly enriched in ^{17}O and so it has not been possible to benchmark the ^{17}O(p,p) cross section.

Chapter 4

Determination and benchmarking of ^{27}Al(d,α & p) reaction cross sections for energies and angles relevant to NRA

M. Salimi[1,2], O. Kakuee[3], S.F. Masoudi[1,*], H. Rafi kheiri[3], E. Briand[2], J-J. Ganem[2], I. Vickridge[2]

[1]Department of Physics, K.N. Toosi University of Technology, P.O. Box 15875-4416, Tehran, Iran
∗Corresponding author: masoudi@kntu.ac.ir
[2]Sorbonne Université, CNRS, Institut des NanoSciences de Paris, INSP, SAFIR, F-75005 Paris, France
[3]Physics and Accelerators Research School, NSTRI, PO Box 14395-836, Tehran, Iran

Abstract

The cross-sections of deuteron-induced nuclear reactions suitable for ion beam analysis, measured in different laboratories, are often significantly different. In the present work, differential cross-sections of ^{27}Al(d,p) and ^{27}Al(d,α) reactions were measured, and the cross sections benchmarked with thick target spectra obtained from pure aluminium for the first time in two independent laboratories. The ^{27}Al(d,p) and (d,α) differential cross-sections were measured between 1.4 and 2 MeV at scattering angles of 165°, 150°, and 135° in the VDGT laboratory in Tehran (Iran), and the same measurements for detector angle of 150° were repeated from scratch, including target making, with independent equipment on the SAFIR platform at INSP in Paris (France). The results of these two measurements at 150° are in good agreement, and for the first time a fitted function is proposed to describe the Al-cross sections for which no suitable theoretical expression exists. The obtained differential cross-sections were validated through benchmarking, by fitting with SIMNRA deuteron-induced particle spectra obtained from a high purity bulk Al target at

both labs for deuteron incident energies between 1.6 and 2 MeV. The thick target spectra are well-reproduced. The evaluated and benchmarked cross sections have been uploaded to the ion beam analysis nuclear data library database (www-nds.iaea.org/ibandl/).

4.1 Introduction

Ion beam analysis (IBA) has been widely used to analyze quantitatively and with high sensitivity the composition and elemental depth profiles in the surface regions of solids. For light element analysis, suitable nuclear reactions can be found and in particular, deuteron-induced reactions, (d,p) or (d,α), often have high Q-values and appreciable cross-sections. In many cases of Nuclear Reaction Analysis (NRA) of thin films, isolated reaction particle peaks may be obtained with judicious choice of scattering angle, incident beam energy, and filtering foils in front of the charged particle detector. However, in general, NRA generates complex spectra with overlapping peaks, especially from thick samples.

Knowledge of the cross-sections for the cases of isolated peaks is already useful for designing experiments to determine elemental contents of thin films. Many such cross-sections, for example ^{16}O(d,p$_0$)^{17}O, ^{16}O(d,p$_1$)^{17}O, ^{12}C(d,p$_0$), ^{14}N(d,α_0), have been carefully measured at energy and angular ranges of analytical interest [87–90]. It is sometimes possible to analyse several light elements simultaneously by NRA. Knowledge of the cross-sections of reactions that are not necessarily of primary interest for thin film analysis, is then often needed for cases in which targets contain elements giving rise to reactions that produce particle groups that interfere with the primary analytical peak, and even more so in thick target NRA where the broadening of the particle spectra from the non-zero target thickness leads to a much greater probability of elemental interferences [26,38,91].

The need for accurate cross sections, even when not of primary interest for a specific analytical problem, or in energy ranges that are not directly analytically useful, has also recently become more acute, with the introduction of the concept of Total IBA [92–94] in which all information from IBA spectra is exploited, and the growing use of Artificial Intelligence and machine learning approaches to optimize information extraction from all parts of IBA spectra [95]. So far, Artificial Neural Networks (ANN) have been applied for the case of Rutherford Backscattering Spectrometry, where the cross sections are known analytically, however reliable extension of these advanced data treatment techniques to NRA requires the best possible nuclear reaction cross sections. Furthermore, accurate experimental nuclear reaction cross-sections are required to provide proper parameters for appropriate approximations and expressions of theoretical nuclear reaction mechanism models.

Because oxygen is the most abundant element in the earth's crust and because of the universal importance of oxides in earth sciences and materials science, accurate cross-

sections for ^{16}O and ^{18}O nuclear reactions have been determined [87, 96]. The second most abundant element is silicon, and although it is an intermediate-mass element from the point of view of IBA, it also has nuclear reactions of analytical interest that have been determined [88, 97].

Aluminium is the third most abundant element that is widely used in industry for its mechanical and electrical properties, decorative applications, and its resistance to environmental aggression especially after suitable electrochemical passivation. Aluminium is also widely present in the alumina-silicate rocks that constitute so much of the earth's upper crust. In many thin film systems, such as III-Nitrogen semiconductors developed amongst other things for UV-C light emitting diodes destined to replace UV mercury lamps in mass sterilisation applications for COVID mitigation, and thin conformal alumina films or nanolaminates grown by Atomic Layer Deposition where aluminium is an essential component, absolute determination of the Al content is paramount for developing improved materials. There is a wealth of deuteron-induced charged particle reactions on ^{27}Al with high Q-values that may be exploited in NRA for analysis of aluminum or encountered as interferences in NRA of aluminium-containing materials [98–108].

There is a further motivation for good knowledge of Al cross sections: even if analysis of Al is not the main objective of a measurement, reaction products from Al may interfere with the signals from other reactions of interest and to be able to fully fit a complex NRA spectrum, all of the cross sections involved need to be known. Detailed knowledge of the cross-sections of these reactions is thus a significant interest in the field of NRA. The compound nucleus ^{29}Si contains too many close levels to be able to be treated satisfactorily within R-Matrix theory, and too few to be able to be handled satisfactorily with a statistical approach. At present, the best we can obtain is well measured experimental cross-sections [98–104].

The first measurements of ^{27}Al(d,α) and ^{27}Al(d,p) cross-sections were made by Gadioli [109] at 150° as part of a study of the fluctuation mechanism occurring in the differential excitation functions. These cross-section curves have since been measured for deuteron energies less than 3 MeV at 90°, 135°, 150°,165°, and 173° [98, 101–104, 109–111], however significant gaps and discrepancies remain.

In this work, we have determined the cross-sections for the ^{27}Al (d,p$_{0+1,2+3,4,5+6,9,10,11,12}$) and ^{27}Al(d, $\alpha_{0,1,2,3,4}$) reactions at an energy below 2 MeV and at 150° scattering angle in two completely independent measurements in two different laboratories: the Van De Graaff Lab in Tehran (VDGT) and the SAFIR platform of the Institut des NanoSciences de Paris (INSP). The ^{27}Al(d,p) and (d,α) cross-sections were also determined at 135° and 165° at VDGT. From our measured data and a critical evaluation of previous measurements, we propose a set of recommended cross-sections for NRA and demonstrate their validity through benchmarking experiments in a thick pure aluminum target in both laboratories.

4.2 Experimental setup and procedure

The experimental setups at VDGT and INSP are significantly different. We present here the main experimental features of each laboratory.

4.2.1 Experimental setup and procedure at VDGT

4.2.1.1 Chamber and data acquisition

At VDGT, cross sections and benchmarking spectra were measured in the 30° left beamline of the 3MV Van de Graaff electrostatic accelerator, equipped with a chamber developed for accurate and reliable RBS/NRA measurements [57]. A beam of 20-40nA was directed into a beam spot of 1.5×1.5 mm^2. The energy resolution is estimated to be about 1 keV. Under these conditions, deadtime was less than 10% and pileup was minimized.

The pressure of the chamber was about 2×10^{-6} mbar during the measurements. The detection system for all of the measurements consisted of three 25 mm^2 ×300 μm thick surface barrier detectors installed at 135°, 150°, and 165° degrees from the incident beam direction. The angular spread of each detector was less than 3°, with solid angles Ω of 1-2 msr. Integrated beam charge Q of 10 μC was usually sufficient to obtain adequate statistics.

4.2.1.2 Calibration energy of the accelerator

We determined beam energy from the field strength of the analyzing magnet, measured with an NMR fluxmeter [39]. The energy calibration of the accelerator was determined from the reaction threshold energy at 1880.44 ± 0.02 keV in the ^{7}Li(p,n)^{7}Be reaction. The target was a pressed LiF pellet with a 10 $\mu g/cm^2$ silver coating for charge evacuation and neutrons were detected with a BF3 detector.

4.2.1.3 Target preparation

The thin Al target must be of appropriate thickness, stable both in atmosphere and under the beam in vacuum, and should also be amorphous to avoid unwanted channeling effects [71]. To achieve these requirements, physical vapor deposition (PVD) was chosen from amongst the different methods for thin Al target preparation [64]. Pure Al was evaporated onto a microscope slide which had been prepared by dipping into a mixture of water and detergent under ultrasonic agitation. The PVD system was a model VE-770 with a base pressure of about 10-6 mbar, equipped with a coiled tungsten filament. The obtained film was floated onto water and then fished over an 8mm diameter hole in a thin metal sheet. Finally, 10 ± 0.5 nm of Ag was deposited onto the thin self-supporting vacuum evaporated Al film as an internal reference [57, 112].

4.2.1.4 Characterization of the thin target

The thin target thickness is determined by RBS [113] with an uncertainty of less than 5%, due to uncertainties in $\Omega \times \Omega$, in possible deviations of the $^{27}Al(\alpha,\alpha)^{27}Al$ cross section from the assumed Rutherford cross section and in fitting the simulated spectrum to the measured spectrum. The thickness of target was only used for determination of deuteron beam energy loss through the target. The thickness and stoichiometry of the Al/Au target were measured at the three detection angles of 135°, 150°, and 165° by alpha particle beams of 1.8 MeV. This measurement was simulated with SIMNRA 7.03 by using the Chu and Yang straggling model and Ziegler/Biersack stopping power [23]. Typical simulated and measured spectra are shown in Figure 4.1.

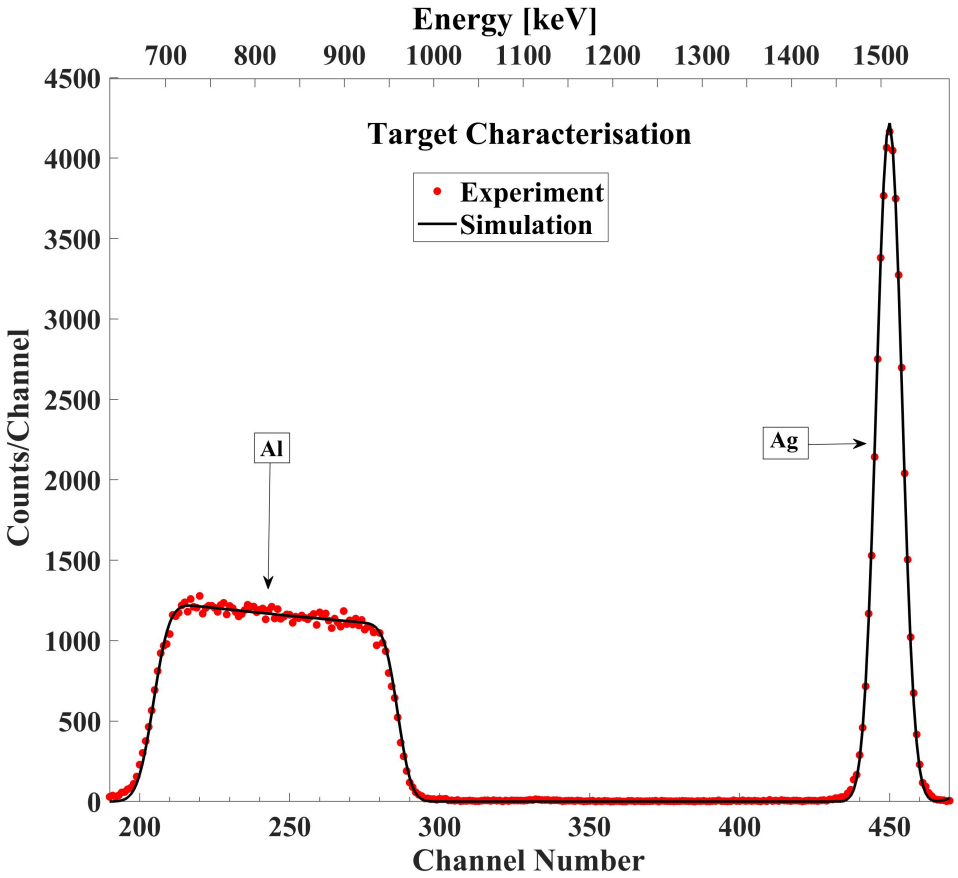

Figure 4.1: Typical simulated and measured RBS spectra from a thin Al/Ag target obtained at scattering angle 150° and E_α= 1.8 MeV.

In target characterization with the alpha beam, the areal density ratio $\frac{N_{Ag}}{N_{Al}}$ was calculated by equation 4.1:

$$\frac{N_{Ag}}{N_{Al}} = \frac{Y_{Ag}}{Y_{Al}} \times \frac{\left(\frac{d\sigma}{d\Omega}\right)^{Al}_{\theta,EBS,E=E_{Al,\alpha}}}{\left(\frac{d\sigma}{d\Omega}\right)^{"Ag"}_{\theta,Ruth,E=E_{Ag,\alpha}}} \tag{4.1}$$

where N corresponds to the areal density of the target and Y to the experimental yield (net area under the peak). Here, N_A rather than [A] is used to represent the areal density

of species A, in order to simplify the expressions. The average of these ratios from different detection angles was estimated by assuming the Rutherford cross section for reaction of alpha particles with Ag and Al, and applying a correction for the energy loss in the thin target. $\left(\frac{d\sigma}{d\Omega}\right)^{Ag}_{\theta,Ruth,E=E_{Ag,\alpha}}$ is defined as the Rutherford cross section at $E_{Ag,\alpha} = E_\alpha - \frac{(\Delta E)^{Ag}_{\theta,E_\alpha}}{2}$ for E_α= 1.8 MeV. The alpha particle elastic scattering cross section $\left(\frac{d\sigma}{d\Omega}\right)^{Al}_{\theta,EBS,E=E_{Al,\alpha}}$ can be considered to be Rutherford for the energy $E_{Al,\alpha} = \widetilde{E_{Al}} - \frac{(\Delta E)^{Al}_{\theta,E=\widetilde{E_{Al}}}}{2}$; $\widetilde{E_{Al}} = E_\alpha - (\Delta E)^{Ag}_{\theta,E=E_\alpha}$. Where E_α, $(\Delta E)^{Al}_{\theta,E=\widetilde{E_{Al}}}$ and $(\Delta E)_{\theta,E_\alpha Ag}$ are the incident alpha energy, energy loss in the Al layer for $E = \widetilde{E_{Al}}$ and energy loss in Ag layer, respectively. Using this ratio eliminates uncertainty due to solid angle, dead time, and charge measurement for the differential nuclear cross section measurements.

4.2.2 Experimental work in INSP Lab

At INSP Lab in Paris, the 30° right beamline of the 2.5 MV Van de Graaff electrostatic accelerator of SAFIR (Système d'Analyse par Faisceaux d'Ions Rapides) platform was employed for our measurement.

The accelerator energy, read from the Generating Voltmeter signal, was calibrated by using the narrow nuclear resonances of the ^{27}Al(p, γ)^{28}Si reaction at 991.88 keV, the ^{13}C(p,γ)^{14}N reaction at 1747.6 keV and the ^{15}N(p,$\alpha\gamma$)^{12}C reaction at 426.1 keV. In each case, the gamma rays were detected with a BGO scintillation detector at 0° [59, 60]. Because of the very high energy resolution of the beam – less than 250eV full width half maximum energy spread over the range reported here, excitation curves were fitted with SPACES [61] so as to compensate for small distortions of the excitation curve due to surface contaminants and oxidation. The treatment of the GVM signal has been implemented into Labview rather than in analogue electronic circuits, giving an energy calibration that is highly linear and practically independent of temperature.

A similar method to that used at VDGT was employed at INSP for preparation of the thin self-supporting targets. An EDWARDS FL 400 and VINCI technologies PVD 4E were used for Al and Au evaporation respectively. The preparation – floating and fishing - and characterization of the target were the same as at VDGT Lab in Tehran. The heavy element used as internal standard need only provide a sufficiently well separated peak of adequate intensity, and here we have used Au rather than Ag as the internal standard for the INSP targets since it was more conveniently available. Subsequently the areal density ratio was taken into account as $\frac{N_{Au}}{N_{Al}}$ in the differential cross section measurement, and of course the appropriate energy loss was calculated for the gold layer. Also, absolute values of the areal densities NAl and NAu were determined by comparing with the standard Bi-implanted Si reference with an uncertainty of 2%–3% in the same RBS measurement. Scanning electron microscopy (SEM) images of the surface of from Au/Al target, shown in Figure 4.2, confirmed the uniformity of the surface structure of samples at the nanoscale.

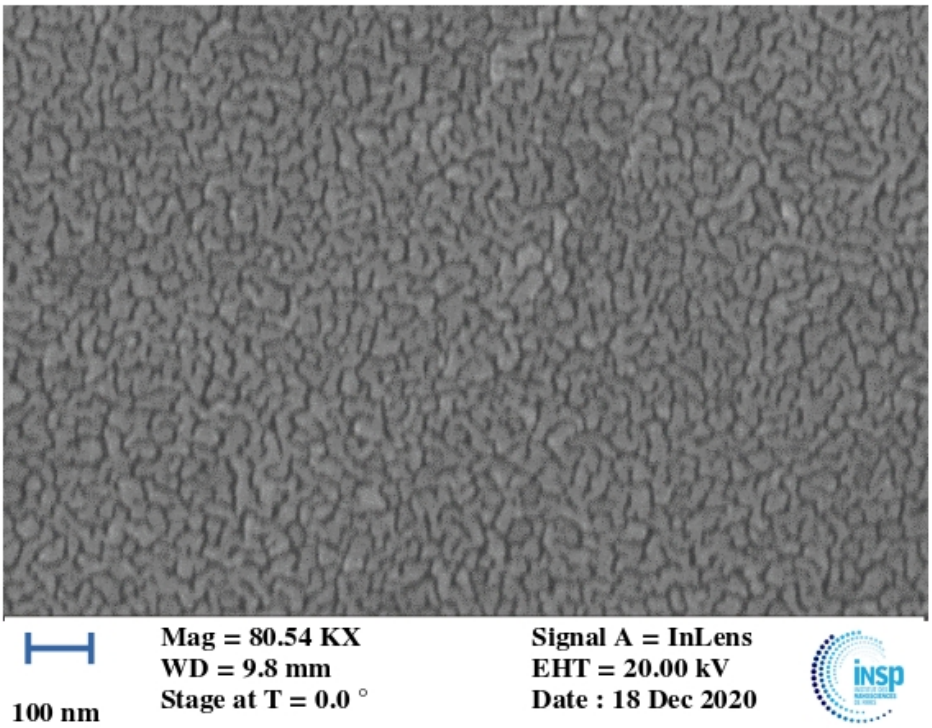

Figure 4.2: SEM images of the surface of from Au/Al target

4.3 Data analysis and results

4.3.1 The differential nuclear cross section measurement value at VDGT Lab in Tehran

Among the nuclear reactions that can be used to characterize Al, ^{27}Al(d,p$_{0+1,2+3,4,5+6,9,10,11,12}$)^{28}Al and ^{27}Al(d,$\alpha_{0,1,2,3,4}$)^{25}Mg were selected for measurements of the deuteron induced reaction cross sections since these particle groups can be identified and their intensities estimated under reasonable experimental conditions. The cross sections were measured with 10 keV steps, for energies ranging from 1.3–2 MeV.

In order to discriminate between high Q-value (d,p) and (d,α) groups in a single measurement setup, we placed a 4 μm thick mylar filter in front of the detector. The judicious choice of 4 mm mylar thickness, to minimize interferences between proton and alpha particle groups in the thin target spectra, was initially found through SIMNRA simulations. The discrimination is illustrated in Figure 4.3, comparing a real measured spectrum with 4 μm mylar, with a simulated spectrum without filter, clearly confirming experimentally that interference between the particles from ^{27}Al(d,p$_{0+1}$)^{28}Al and ^{27}Al(d,α_0)^{25}Mg, and from ^{27}Al(d,p$_4$)^{28}Al and ^{27}Al(d,α_3)^{25}Mg is eliminated.

The differential cross section values $\left(\frac{d\sigma}{d\Omega}\right)_{\theta,E(Al)}$ at the energy E$_d$ and detection angle

α were obtained from Eq. 4.2:

$$\left(\frac{d\sigma}{d\Omega}\right)_{\theta,E(Al)} = \left(\frac{d\sigma}{d\Omega}\right)^{Ag}_{(\theta,EBS,E_d(Ag)} \times \frac{Y_{Al}}{Y_{Ag}} \times \frac{N_{Ag}}{N_{Al}} \times \frac{(Q\times\Omega)^{\theta,Ag}}{(Q\times\Omega)^{\theta,Al}} \tag{4.2}$$

where E_d, Y_{AlorAg}, θ and $(\Delta E)^{Ag}_{\theta,d}$ represent incident deuteron beam energy, the experimental yield of Al or Ag (net area under the peak), scattering angle and energy loss in Ag layer, respectively. $\left(\frac{d\sigma}{d\Omega}\right)^{Ag}_{(\theta,EBS,E_d(Ag)}$ is the differential cross section of the ^{nat}Ag(d,d$_0$) reaction at $E_d(Ag) = E_{d,\theta} - \frac{(\Delta E)^{Ag}_{\theta,d}}{2}$, which is Rutherford below 2 MeV. $\frac{(Q\times\Omega)^{\theta,Ag}}{(Q\times\Omega)^{\theta,Al}}$ is equal to one since the charge (Q) and solid angle (Ω) for Al and Ag are identical at each scattering angle, eliminating the uncertainty due to Q and Ω measurement. Also $\frac{N_{Ag}}{N_{Al}}$, was measured by RBS as explained above.

The measured excitation functions at VDGT Lab at scattering angle 150° for the ^{27}Al(d,α_{0-3})^{25}Mg and ^{27}Al(d,p$_{0-12}$)^{28}Al reactions are displayed in Figures 4.4 and 4.5 and the excitation functions for the ^{27}Al(d,α)^{25}Mg and ^{27}Al(d,p)^{28}Al reactions at scattering angles 165° and 135° are shown in Figures 4.6a, 4.6b, 4.7a and 4.7b. The only previous measurements of the ^{27}Al(d,α) cross sections of which we are aware, apart from at 150° where there are several data sets that are discussed below, is that from [114] for 135°. This data is indicated on Figure 4.7a, however the values are rather sparse and show significant fluctuations. They were not further used in the present work.

4.3.2 The differential cross section measurement at INSP Lab in Paris

The experiments were done with three different experimental setups, as follows: for (d,α) reaction measurements, we used the 4 μm-thick mylar in front of the 300 μm-thick surface barrier detector and repeated these measurements without mylar in front of the detector. For (d,p) reaction measurements, in the third configuration, a 100 μm-thick mylar was chosen in front of a 500 μm-thick pin diode detector at scattering angle of 150°. Typical experimental alpha particle and proton spectra from the ^{27}Al(d,α)^{25}Mg and ^{27}Al(d,p)^{28}Al reactions are shown in Figure 4.8a and Figure 4.9a, respectively.

The differential cross-sections were determined by using equation 4.1, just replacing Ag by Au:

$$\left(\frac{d\sigma}{d\Omega}\right)_{\theta,E_d(Al)} = \left(\frac{d\sigma}{d\Omega}\right)^{Au}_{\theta,EBS,E_d(Au)} \times \frac{Y_{Al}}{Y_{Au}} \times \frac{N_{Au}}{N_{Al}} \tag{4.3}$$

where θ, $Y_{Al,\text{and}Au}$, E$_d$(Au), E$_d$(Al) correspond to the scattering angle, integrated yields (Au and Al) as obtained from the experimental spectra, the energy at the surface of the Au layer, and the energy at half of the Aluminium thickness (including energy loss in the Au film), respectively. $\frac{N_{Au}}{N_{Al}}$ represents the areal density of Au versus Al present in the

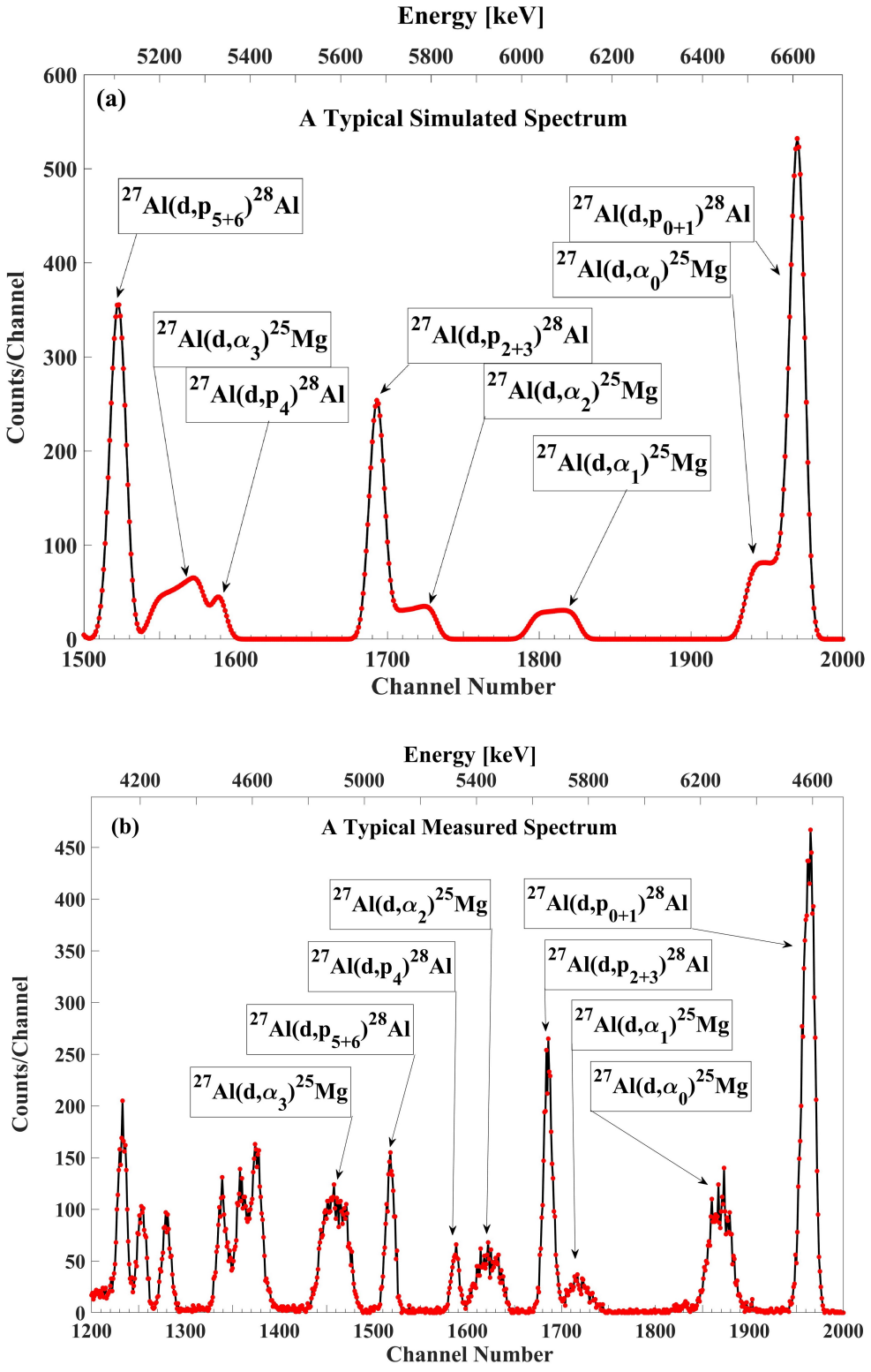

Figure 4.3: (a) The simulated spectrum without mylar and (b) the typical measured spectrum in experimental work with 4 μm mylar in front of the particle detector at the detection angle of 150° and for $E_{d,lab}$ = 1.8 MeV at VDGT Lab in Tehran. The interferences between the high energy alpha and proton groups are clearly resolved.

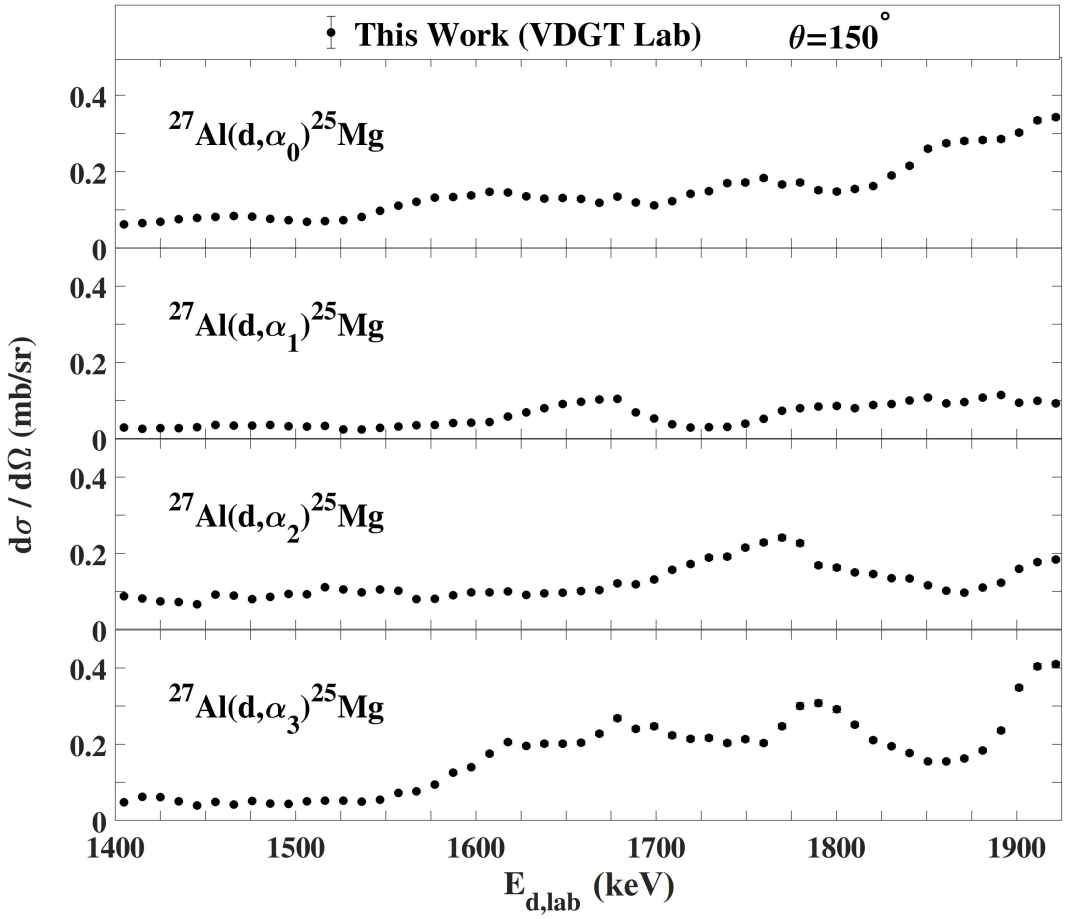

Figure 4.4: The excitation functions at scattering angle 150° at VDGT Lab in Tehran for the ^{27}Al(d,α)^{25}Mg reactions. The estimated uncertainties from counting statistics are smaller than the plotted symbols.

target, measured by RBS.

4.3.3 Uncertainties

Using the measured $\frac{N_{Au}}{N_{Al}}$ ratio and normalizing the cross section measurement to the corresponding Rutherford cross-section, the uncertainties owing to solid angle, detector angular settings, dead time, and charge measurement were eliminated [115]. The uncertainty of the $\frac{N_{Au}}{N_{Al}}$ ratio was estimated to be about 3% according to the counting statistics. The corresponding statistical uncertainties of $\left(\frac{d\sigma}{d\Omega}\right)_{\theta,E_d(Al)}$ were estimated to be 4%-9% according to the error propagation formulas. The measured differential cross section at INSP Lab with error bars at scattering angle 150° for the ^{27}Al(d,α_{0-3})^{25}Mg and ^{27}Al(d,p$_{0-6}$)^{28}Al reactions are indicated in Figure 4.8b and Figure 4.9b.

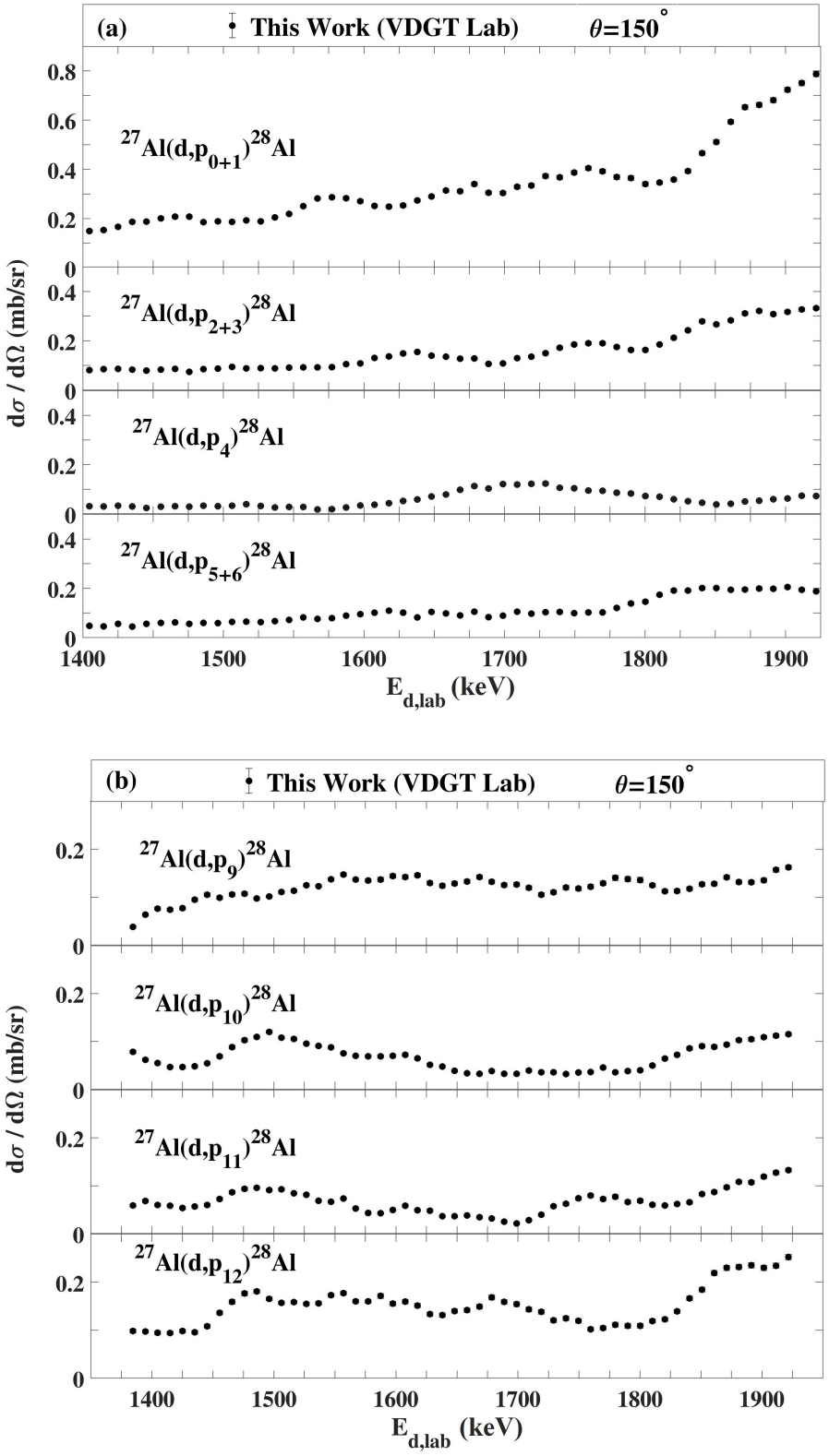

Figure 4.5: Differential cross section values for (a) ^{27}Al(d,p$_{0-6}$)^{28}Al and (b) ^{27}Al(d,p$_{9-12}$)^{28}Al reactions at scattering angle 150° at VDGT Lab in Tehran. The estimated uncertainties from counting statistics are smaller than the plotted symbols.

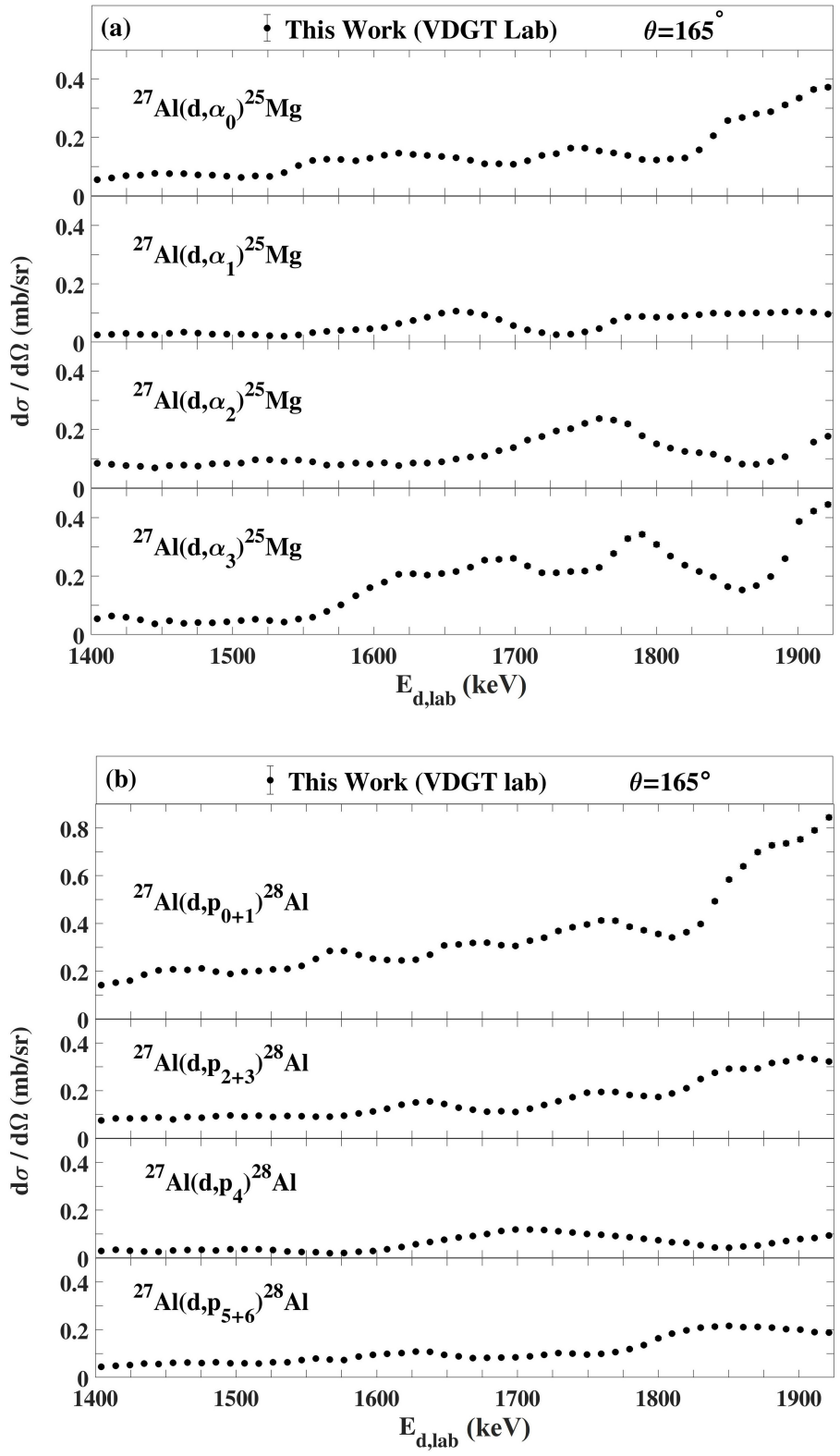

Figure 4.6: The differential cross sections at 165° measured at VDGT Lab in Tehran for the (a) ^{27}Al(d,α)^{25}Mg and (b) ^{27}Al(d,p)^{28}Al reactions. The estimated uncertainties from counting statistics are smaller than the plotted symbols.

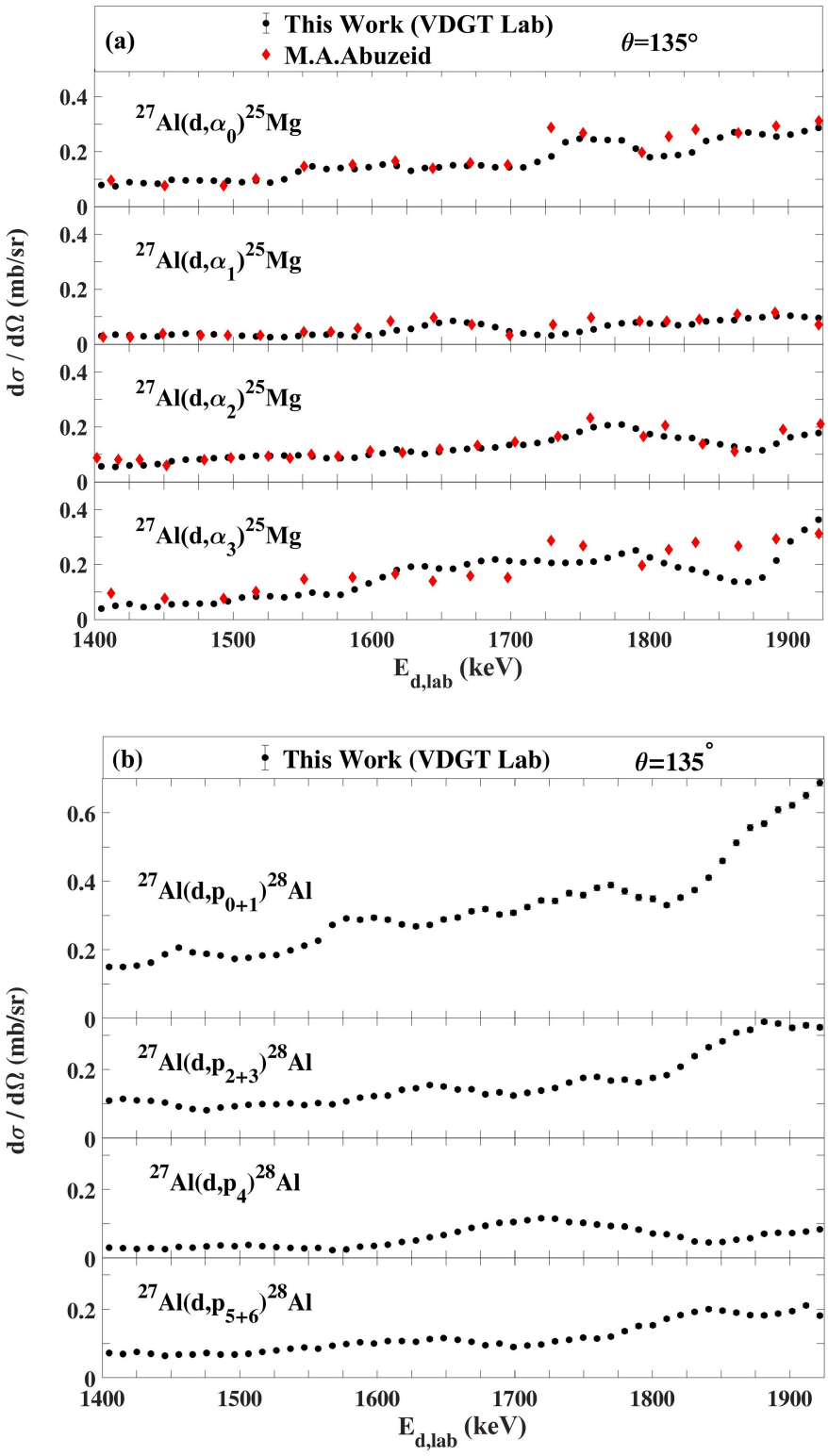

Figure 4.7: The differential cross sections measured at 135° at VDGT Lab in Tehran for the (a) ^{27}Al(d,α)^{25}Mg reactions together with the data from Ref [114] and (b) ^{27}Al(d,p)^{28}Al reactions. The estimated uncertainties from counting statistics are smaller than the plotted symbols.

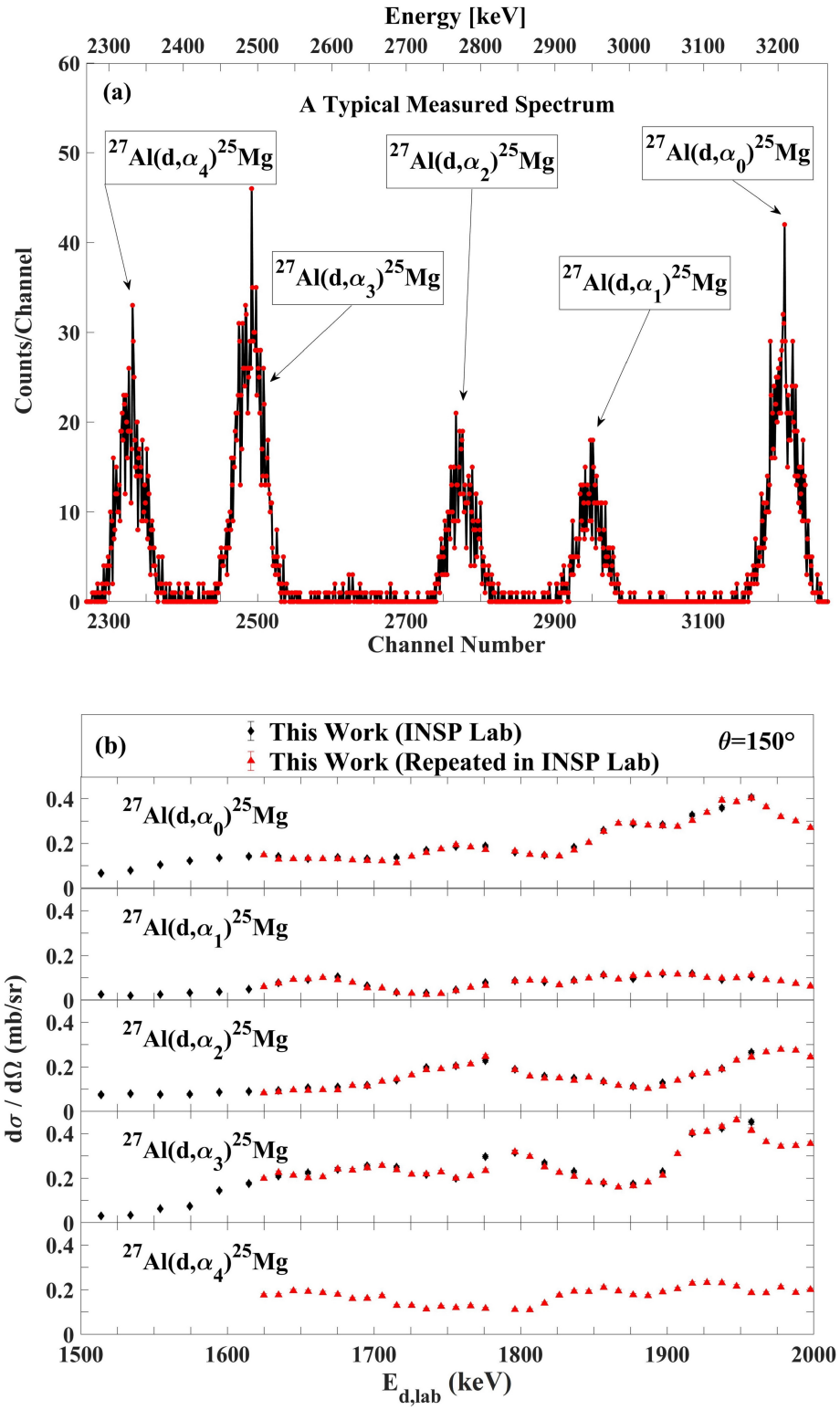

Figure 4.8: (a) A typical spectrum of alpha-particles for the ^{27}Al(d,α)^{25}Mg reaction, (b)The excitation functions for the ^{27}Al(d,α)^{25}Mg reaction at scattering angle 150° at INSP Lab in Paris. The estimated uncertainties from counting statistics are smaller than the plotted symbols.

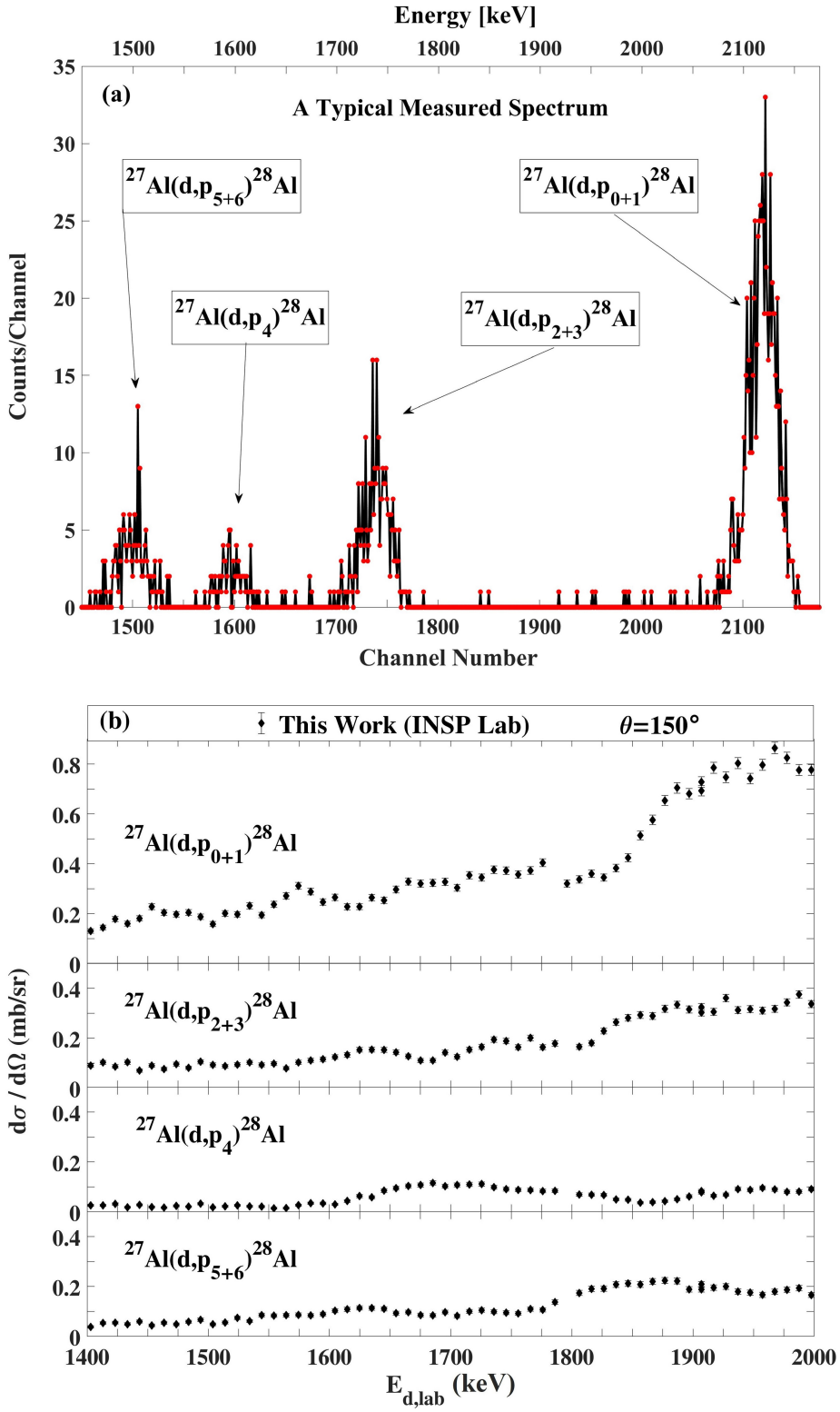

Figure 4.9: (a) A typical spectrum of protons for the ^{27}Al(d,p)^{28}Al reaction. (b) The excitation functions for the ^{27}Al(d,p)^{28}Al reaction at scattering angle 150° at INSP Lab in Paris. Where not visible, the estimated uncertainties from counting statistics are smaller than the plotted symbols.

4.4 Discussion

4.4.1 Correspondence between VDGT's data and INSP's data

Figure 4.10 shows the comparison between our data from VDGT and from INSP. The results show that the data acquired at INSP Lab in Paris for ^{27}Al(d,$\alpha_{0,1,2,3,4}$)^{25}Mg and ^{27}Al(d,p$_{0+1,2+3,4,5+6}$)^{28}Al are in acceptable agreement with data obtained at VDGT Lab at 150° scattering angle. Since these datasets were obtained under completely independent and somewhat different setups, this agreement is a strong indicator of the validity of the datasets. We further note that the measured target thicknesses correspond to deuteron energy losses of 8 to 10 keV in the Paris (INSP lab) samples and of 26-30 keV in the Teheran (VDGT lab) samples. This means that the measured cross sections are smoothed over these energy ranges. The very good correspondence between the two measurement sets also confirms that the cross sections are varying only slowly over these energy ranges.

4.4.2 Comparison with previous studies

Although we are not aware of previous measurements for 135° (other than [114], for (d,α), discussed above) and 165° scattering angles, several data sets exist for 150°. Comparison of the cross sections measured here with available aluminum (d,p) and (d,α) cross-sections at 150° is presented in Figure 4.11. As mentioned in [98], the measurements of Ref. [101] barely overlaps with previous studies, and the data from [104] are underestimated by a factor of about 2, so they are no longer considered here. The differential cross section values in Ref [109] show systematic differences from the other data, beyond the uncertainties given in the paper, both for ^{27}Al(d,p$_{0+1,2+3,4,5+6}$)^{28}Al and ^{27}Al(d, $\alpha_{0,1,2,3,4}$)^{25}Mg. Data in Ref. [98] are in acceptable agreement with our data except for a small energy shift. We attribute this energy shift to the energy loss of the incident beam in the target, which was not taken into account in [98]. The four retained datasets have been plotted in Figure 4.12 for the 150° scattering, with the data from Ref. [98] corrected for the energy loss in the target, using the target thickness supplied in that publication.

4.4.3 Evaluation of 150° cross section measurements

Since there is no suitable nuclear reaction model for these reactions, the question arises as to how to represent the best averaged values of the data to propose a single recommended cross section at any energy within the measured range. We have taken the approach of fitting a freely chosen mathematical function to all of the data, weighted inversely according to their reported uncertainties.

The four retained datasets were therefore fitted with 8-term and 20-term Fourier series,

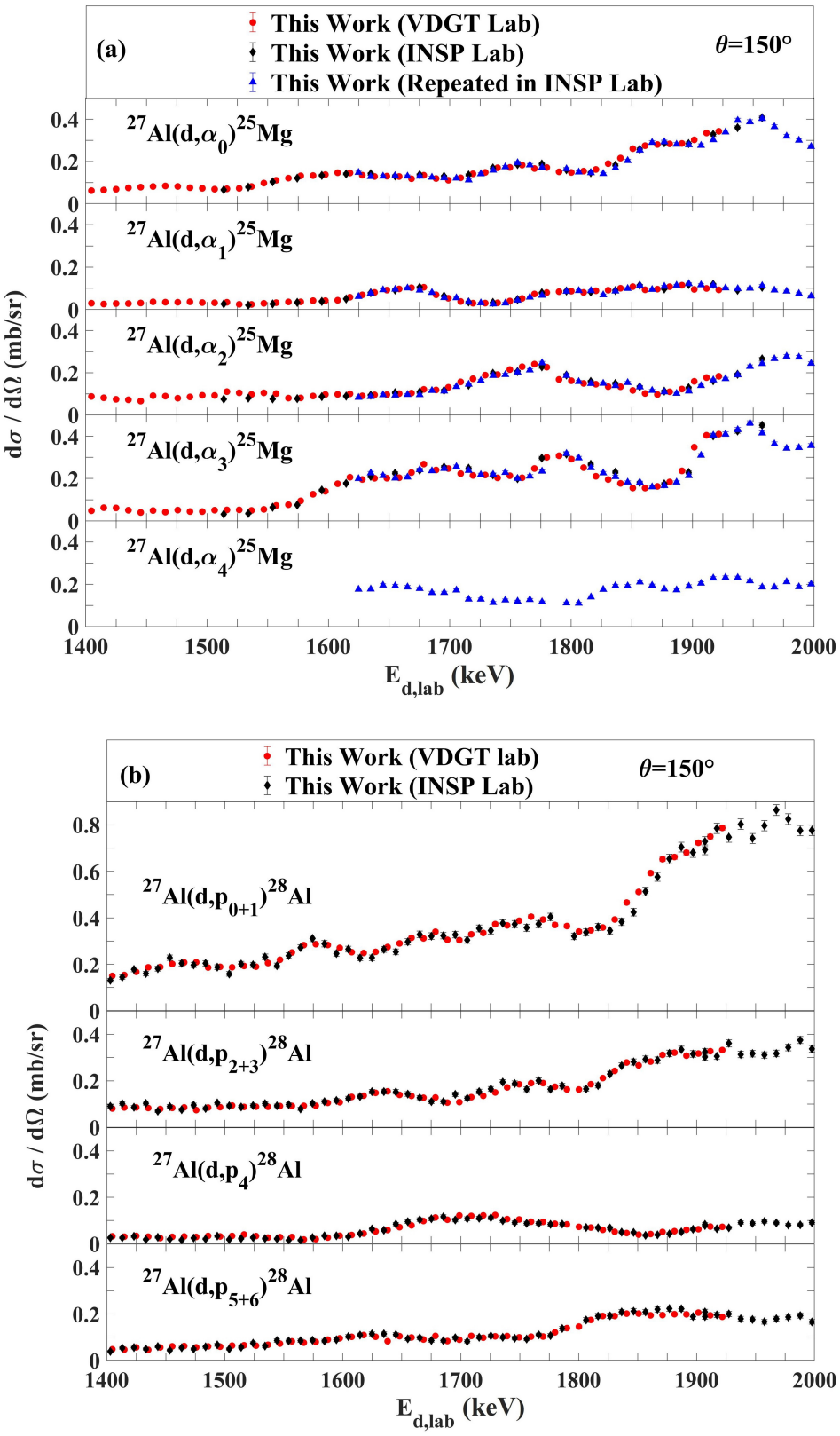

Figure 4.10: The comparison between our data from VDGT and from INSP at 150° for the (a) ^{27}Al(d,$\alpha_{0,1,2,3,4}$)^{25}Mg and (b) ^{27}Al(d,p$_{0+1,2+3,4,5+6}$)^{28}Al reactions.

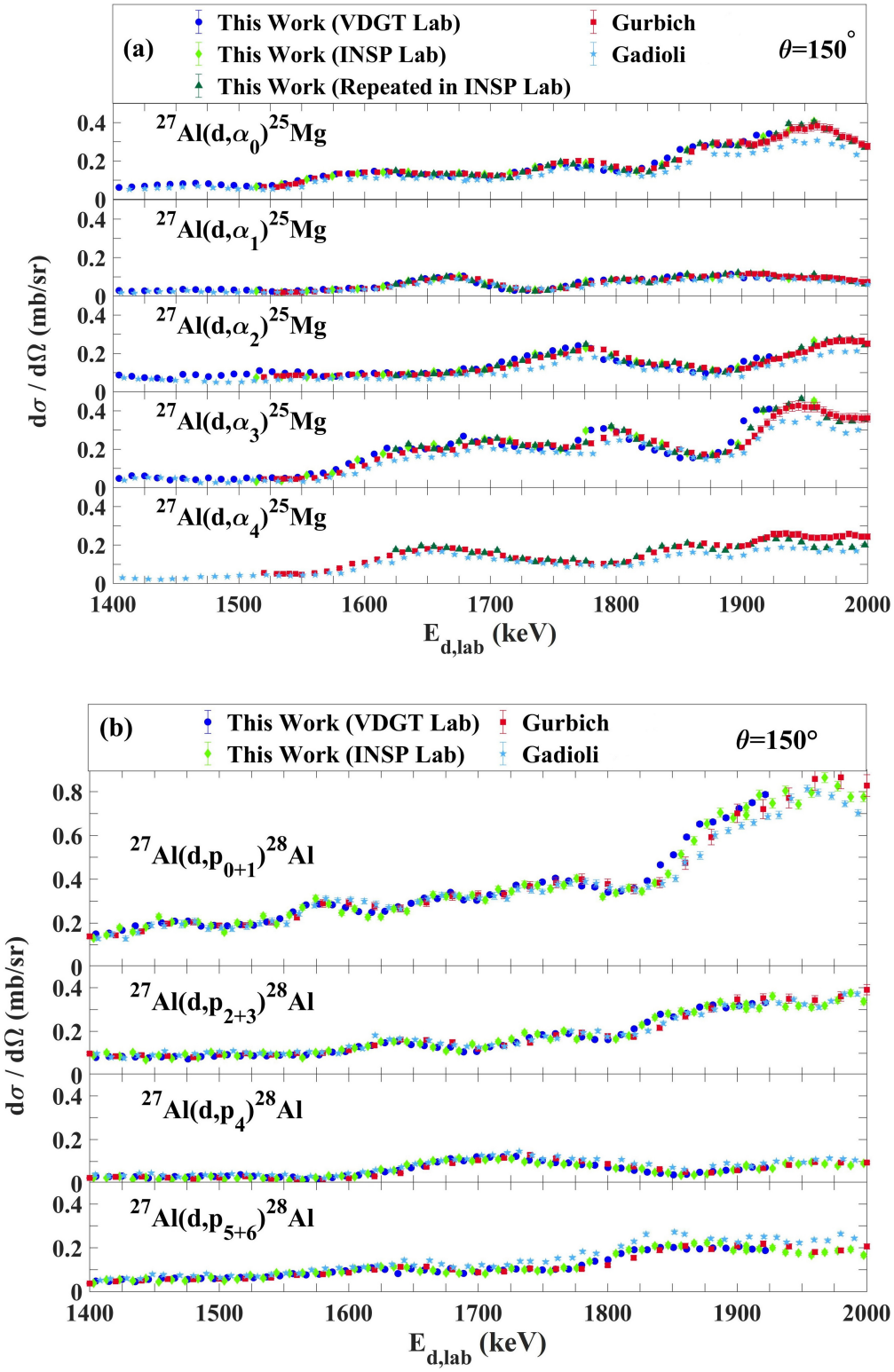

Figure 4.11: The comparison of our work with other data at 150° for (a) ^{27}Al(d,$\alpha_{0,1,2,3,4}$)^{25}Mg and (b) ^{27}Al(d,p$_{0+1,2+3,4,5+6}$)^{28}Al reactions [98, 109].

and a spline interpolation algorithm, shown in Figure 4.12, by MATLAB programming language.

The differences between the fitted functions are small but the 20-term Fourier series allows the data to be represented with good fidelity and not too many fitted parameters. This is shown in Figure 4.13.

4.4.3.1 Fourier series equations

One of the advantages of fitting the data with the Fourier series is that the theoretical function can be expressed easily and used as a reference model in future works. The actual Fourier series are written as follows [116]:

$$f(x) = a_0 + \sum_{n=1}^{N} a_n \cos(n\omega x) + b_n \sin(n\omega x) \tag{4.4}$$

Theoretically, the Fourier coefficients a_n and b_n can be evaluated as follows:

$$a_0 = \frac{1}{T}\int_T f\,(x)\,dx \tag{4.5}$$

$$a_n = \frac{2}{T}\int_T f(x)\cos(n\omega x)dx \tag{4.6}$$

$$b_n = \frac{2}{T}\int_T f(x)\sin(n\omega x)dx \tag{4.7}$$

Considering the N=20 Fourier series, the coefficients for all of the cross sections reported here (in addition to the 150° collection) were calculated and are presented in Table 4.1. The goodness of fit is given by the coefficient of correlation R which describes the proportion of the variation of the data described by the fitted function [117]. R^2 is above 0.96 for the highest cross sections, and above 0.9 even for the lower cross sections which are statistically noisier.

4.5 Benchmarking the Evaluated cross sections

The measured cross sections are validated by a benchmarking exercise [84,85], in which the cross sections are used in an independent experiment. For NRA cross sections, this almost always consists in obtaining thick target NRA spectra from a well-defined (often mono-elemental) target and verifying the extent to which the measured cross sections reproduce the observed spectra when included in an established NRA simulator such as SIMNRA. To our knowledge, only the ^{27}Al(d,p)^{28}Al cross-sections have been benchmarked, by obtaining and fitting thick target spectra, for just one incident energy and one scattering angle [98], whilst there have been no benchmarking experiments at all for ^{27}Al(d,α)^{25}Mg cross

Table 4.1: The coefficients and Goodness of fitting for final fitting.

	^{27}Al(d,α_0)^{25}Mg	^{27}Al(d,α_1)^{25}Mg	^{27}Al(d,α_2)^{25}Mg	^{27}Al(d,α_3)^{25}Mg	^{27}Al(d,α_4)^{25}Mg	^{27}Al(d,p_{0+1})^{25}Al	^{27}Al(d,p_{2+3})^{25}Al	^{27}Al(d,p_4)^{25}Al	^{27}Al(d,p_{5+6})^{25}Al
a_0	0.3102	0.1135	0.2474	0.3491	0.2877	0.753	0.3259	0.1097	0.207
a_1	-0.0212	-0.0186	-0.027	-0.0583	-0.0268	0.1395	0.0736	0.0328	0.0591
a_2	-0.0601	-0.0182	-0.0077	-0.0181	0.0684	-0.1852	-0.0587	-0.006	-0.0334
a_3	-0.0442	-0.0056	-0.0422	-0.0582	-0.0113	0.021	-0.0086	0.012	-0.0027
a_4	-0.0247	-0.0133	-0.0319	-0.0536	0.0087	0.0258	0.0107	0.0026	0.0033
a_5	-0.0155	0.0034	-0.0113	0.0047	0.0016	-0.0588	-0.0198	-0.0068	-0.0178
a_6	-0.0039	-0.0069	-0.0059	0.0019	-0.009	0.0617	0.0117	0.0059	0.0036
a_7	0.0126	0.0047	0.0033	-0.0135	0.0116	-0.0078	0.0052	-0.0014	0.0004
a_8	0.0001	-0.0002	0.0015	0.002	-0.0061	-0.017	-0.0006	-0.0041	-0.0056
a_9	0.0019	0.0009	0.0069	0.0052	-0.0021	0.0461	0.0059	0.0037	-0.0009
a_{10}	0.0043	0.0011	0.005	0.0127	0.0027	-0.0069	-0.0074	-0.0025	-0.0033
a_{11}	0.0069	-0.0005	-0.0013	0.01	-0.001	-0.017	0.0007	-0.0018	-0.0031
a_{12}	0.0021	-0.0002	0.002	0.0017	0.0033	0.0183	0.0082	0.0022	0.0039
a_{13}	0	0.0008	-0.0023	0.0056	0	-0.0098	-0.0018	-0.0031	-0.0014
a_{14}	-0.001	-0.0005	-0.0015	-0.001	-0.0022	-0.0032	-0.0011	0.0002	-0.0023
a_{15}	-0.0038	-0.0018	-0.0029	-0.0021	0.0038	0.0082	0.0038	0.0031	0.002
a_{16}	-0.0049	-0.0005	-0.0041	-0.0063	-0.0016	-0.0101	-0.0004	-0.0008	-0.0003
a_{17}	-0.0042	-0.0013	-0.0036	-0.0073	-0.0007	0.0072	0.0024	0.0002	0.0011
a_{18}	-0.004	-0.0013	-0.0039	-0.0036	0.0026	0.005	-0.0016	0.0003	0.001
a_{19}	-0.0024	-0.0008	-0.0022	-0.0034	-0.003	0.0006	0.0005	0.0014	0.0005
a_{20}	-0.0002	0.0003	-0.0013	-0.002	0.0022	0.0023	0.0009	0.0012	-0.0005
b_1	-0.0945	-0.0291	-0.0502	-0.1104	0.0425	0.2519	0.0933	0.0164	0.0501
b_2	-0.0442	-0.0097	-0.0099	-0.0662	-0.0309	0.0331	0.0389	-0.0108	0.0241
b_3	0.0088	0.0164	-0.0263	-0.0033	-0.016	-0.1105	-0.039	-0.0272	-0.0113
b_4	0.031	-0.0022	0.0238	0.0313	0.0179	0.0541	0.0216	-0.0001	0.0219
b_5	0.0098	0.0075	0.0161	0.0312	-0.016	-0.0433	-0.0028	-0.0055	0.0041
b_6	0.0208	0.0009	0.0211	0	-0.0014	-0.0438	-0.0139	0.0006	-0.0099
b_7	0.0073	0.0058	0.0126	0.0169	0.012	0.046	-0.0006	0.0081	0.0049
b_8	0.0029	0.0025	0.0082	0.0093	-0.0113	-0.0247	-0.0137	-0.0043	-0.0023
b_9	0.0058	0.0008	0.0083	0.013	0.0047	-0.0094	-0.0005	0.0017	-0.0015
b_{10}	0.0037	-0.0003	-0.0022	0.0028	-0.002	0.0257	0.0002	0.0028	0.002
b_{11}	-0.0031	-0.0011	-0.0033	-0.0082	-0.0015	-0.0204	-0.0086	-0.0036	-0.0032
b_{12}	-0.0043	0.0011	-0.0029	-0.004	0.0029	-0.0006	0.0016	0.0011	0
b_{13}	-0.0055	-0.0017	-0.0059	-0.0088	-0.0048	0.0176	0.005	0.0014	0.0021
b_{14}	-0.0052	-0.0017	-0.0049	-0.0072	0.0013	-0.0103	-0.0049	-0.0024	-0.0021
b_{15}	-0.0041	-0.0015	-0.0053	-0.0062	0.0023	0.002	0.0013	0.0016	0.0001
b_{16}	-0.0022	-0.0002	-0.0007	-0.004	-0.0041	0.0034	0.0003	0.002	0.0018
b_{17}	-0.0008	-0.001	-0.0005	0.0008	0.0045	-0.007	0.0002	-0.0008	-0.0015
b_{18}	0.0014	0.0002	0.0017	0.0017	0.0002	0.0064	0.0033	0.0003	0.0002
b_{19}	0.0018	0.0012	0.0022	0.0029	-0.0026	-0.0009	-0.0012	-0.0006	0.001
b_{20}	0.0022	0.0002	0.0004	0.002	0.0033	0.0014	0.0021	0.0009	0.0007
$\omega = 2\pi/T$									
	0.0092	0.0092	0.0092	0.0092	0.0113	0.0071	0.0071	0.0071	0.0071
Goodness of Fitting									
R^2	0.9767	0.9681	0.949	0.965	0.9139	0.9657	0.9699	0.947	0.9751

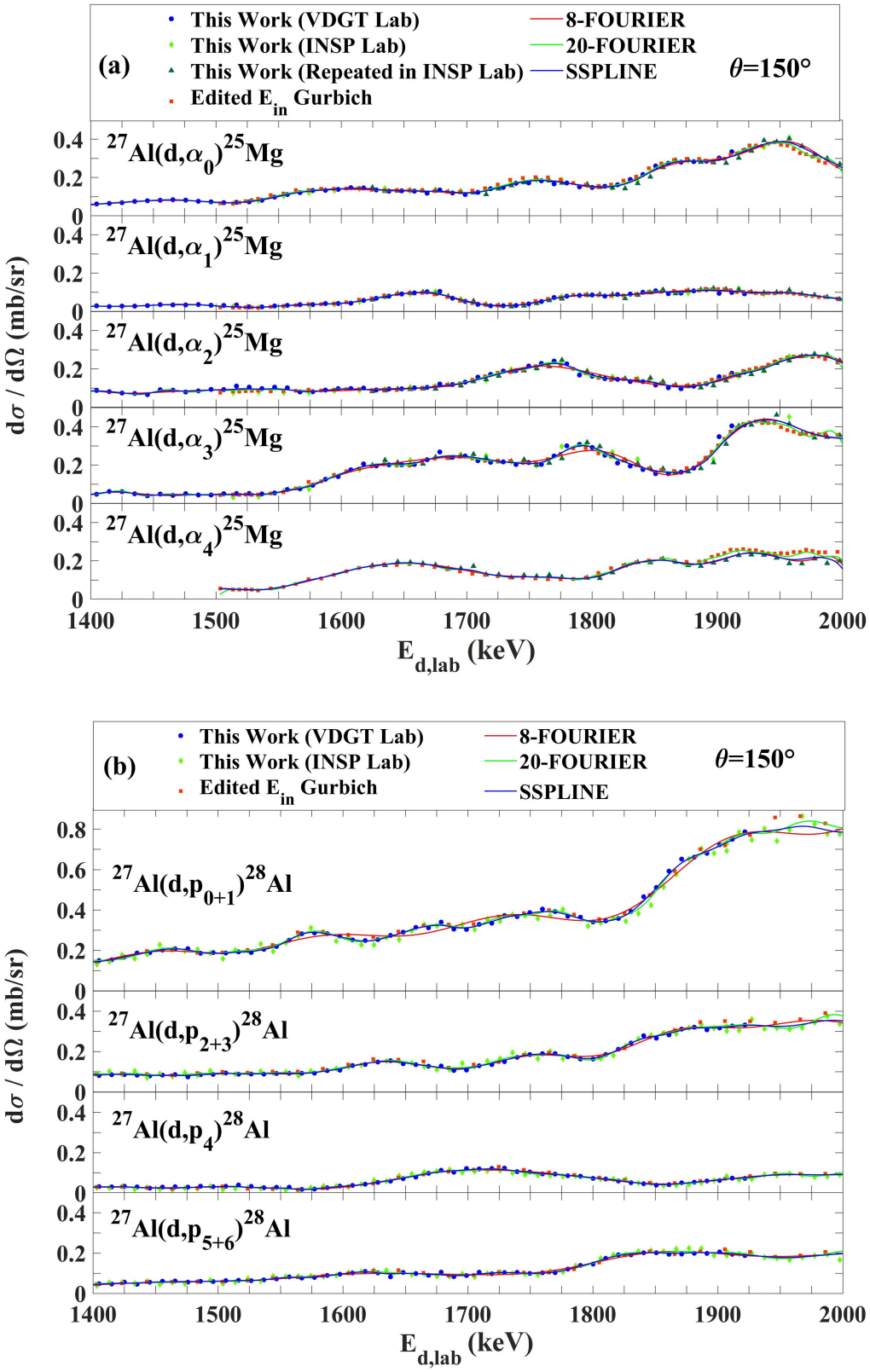

Figure 4.12: The comparison of different fitting methods for cross sections at 150° for (a) ^{27}Al(d, $\alpha_{0,1,2,3,4}$)^{25}Mg and (b) ^{27}Al (d,p$_{0+1,2+3,4,5+6}$)^{28} Al reactions.

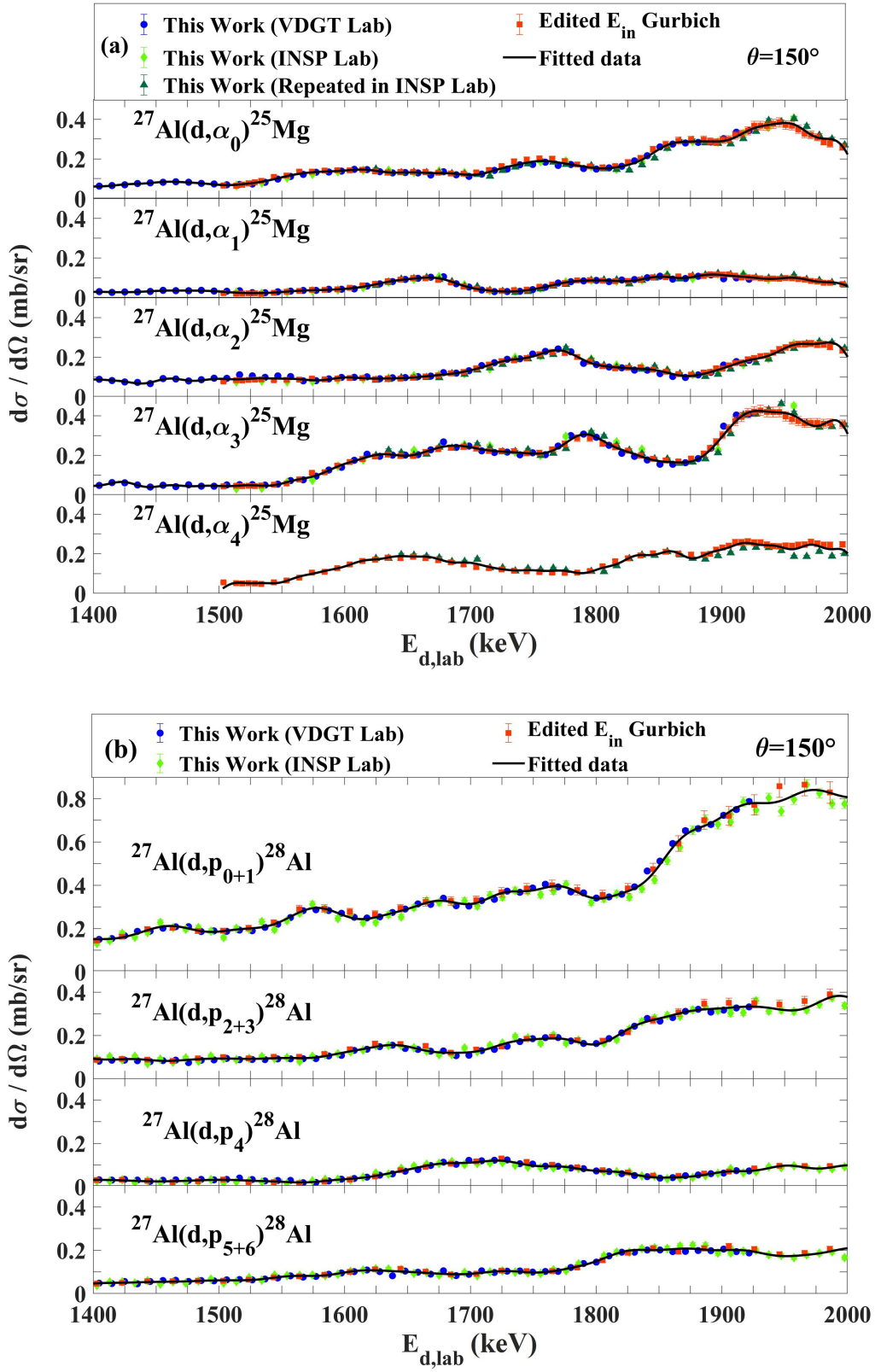

Figure 4.13: The fitted data for 150° for (a) ^{27}Al(d,$\alpha_{0,1,2,3,4}$)^{25}Mg and (b) ^{27}Al (d,p$_{0+1,2+3,4,5+6}$)^{28} Al reactions.

sections.

The goal of the present work is to benchmark the ^{27}Al(d,p)^{28}Al and ^{27}Al(d,α)^{25}Mg cross sections at three scattering angles, 135°, 150°, and 165°, and with various incident beam energies in two different laboratories.

For the experimental part of benchmarking, charged particle spectra were obtained from a thick pure aluminium target under deuteron irradiation. For the simulation part of benchmarking, the SIMNRA 7.03 code is applied with the Chu and Yang straggling model and Ziegler/Biersack stopping power.

4.5.1 Benchmarking of measured data for ^{27}Al(d,p)^{28}Al and ^{27}Al(d,α)^{25}Mg reactions at VDGT Lab in Tehran

For benchmarking the ^{27}Al(d,p)^{28}Al and ^{27}Al(d,α)^{25}Mg cross sections at VDGT Lab in Tehran, we used a thick pure Al target with a thin Ag layer deposited on it for the self-normalization process. No mylar was used in front of the detector. Other experimental parameters are as explained in section 4.2.1. The results of benchmarking for E_d=1600-1900keV at the scattering angles of 135°, 150° and165°, with an incident energy interval of 100keV, are shown in Figure 4.14, Figure 4.15, and Figure 4.16, respectively. At 150°, the three cross section data sets (VDGT data, INSP data, and fitted data) have been incorporated into the SIMNRA library. Overall, the agreement between the simulated and measured spectra is satisfying.

4.5.2 Benchmarking of measured data for ^{27}Al(d,p)^{28}Al reactions at INSP Lab in Paris

For benchmarking the ^{27}Al(d,p)^{28}Al cross sections at INSP Lab in Paris, Au rather than Ag deposited on the thick pure Aluminum target acted as the internal reference. Moreover, a new multi-holder detector at INSP lab was designed (Figure 4.17), which included three 1cm2 Hammamatsu S3590-09 PIN diodes, with depletion depth of 300 μm, as detectors at 135°, 150° and 165°. A 100 μm mylar foil in front of each detector ensured the elimination of the alpha particles from the spectrum.

The benchmarking results are displayed in Figure 4.18 for E_d=1700-2000keV with an energy step of 100keV, at the scattering angle of 150° for VDGT data, INSP data, and fitted data sets. Figures 4.19 and 4.20 present the benchmarking results for E_d=1500-1800keV with an energy step of 100keV at the scattering angles of 165° and 135°, respectively. The simulation at these angles employed the measured VDGT cross section data. In general, the correspondence between the simulations and the measured thick target spectra was very satisfying.

The range of measured cross-sections used for simulating the spectra was 1.4-2 MeV.

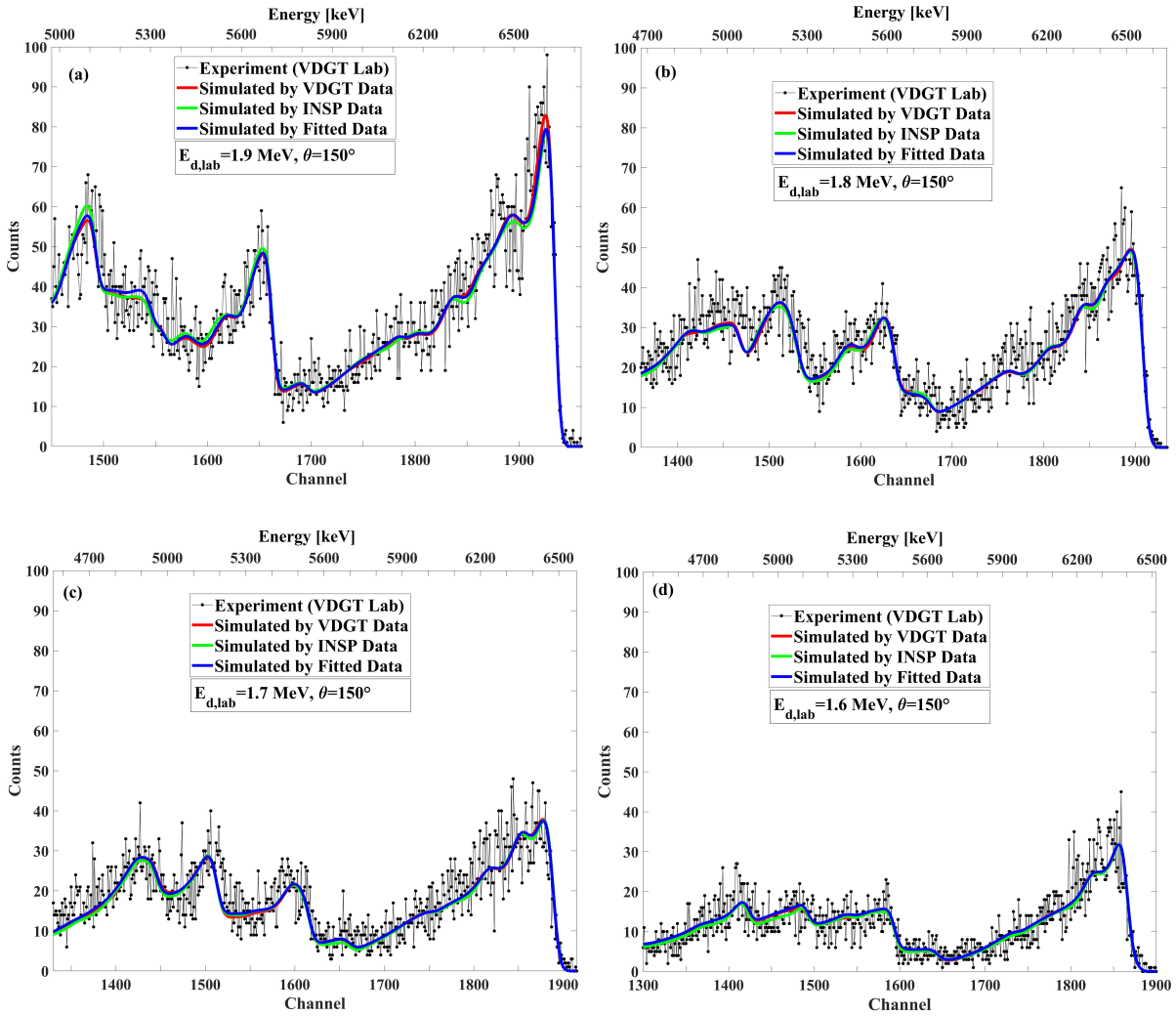

Figure 4.14: The benchmarking result at VDGT Lab in Tehran with different data sets at 150° and different incident deuteron energies, (a) 1.9 MeV, (b) 1.8 MeV, (c) 1.7 MeV and (d) 1.6 MeV.

After energy loss in the Al target, whenever $E_{d,Lab}$ falls below the minimum energy of the measured cross section (1.4 MeV), the corresponding simulation of measured cross-sections has no value and SIMNRA considers its value equal to zero. In this case, for the ^{27}Al(d,p_{0+1}) reaction we manually inserted widely spaced cross section values for energies below 1.4 MeV so that the measured thick target spectra in the energy range from 4700-5000 keV were reproduced by the simulations. Similar inclusions were made for the ^{27}Al(d,$p_{0+1,2+3,4,5+6}$) cross sections in the relevant energy ranges. These cross section values are certainly of the right amplitude, but because of the energy straggling of the incident beam at these depths in the target, in this energy range the proposed cross section would not faithfully represent any fine structure. In order to differentiate between the cross sections measured by the thin targets and incarnated by the N=20 Fourier series, from the values inferred from the benchmarking experiments, the two data sets are loaded

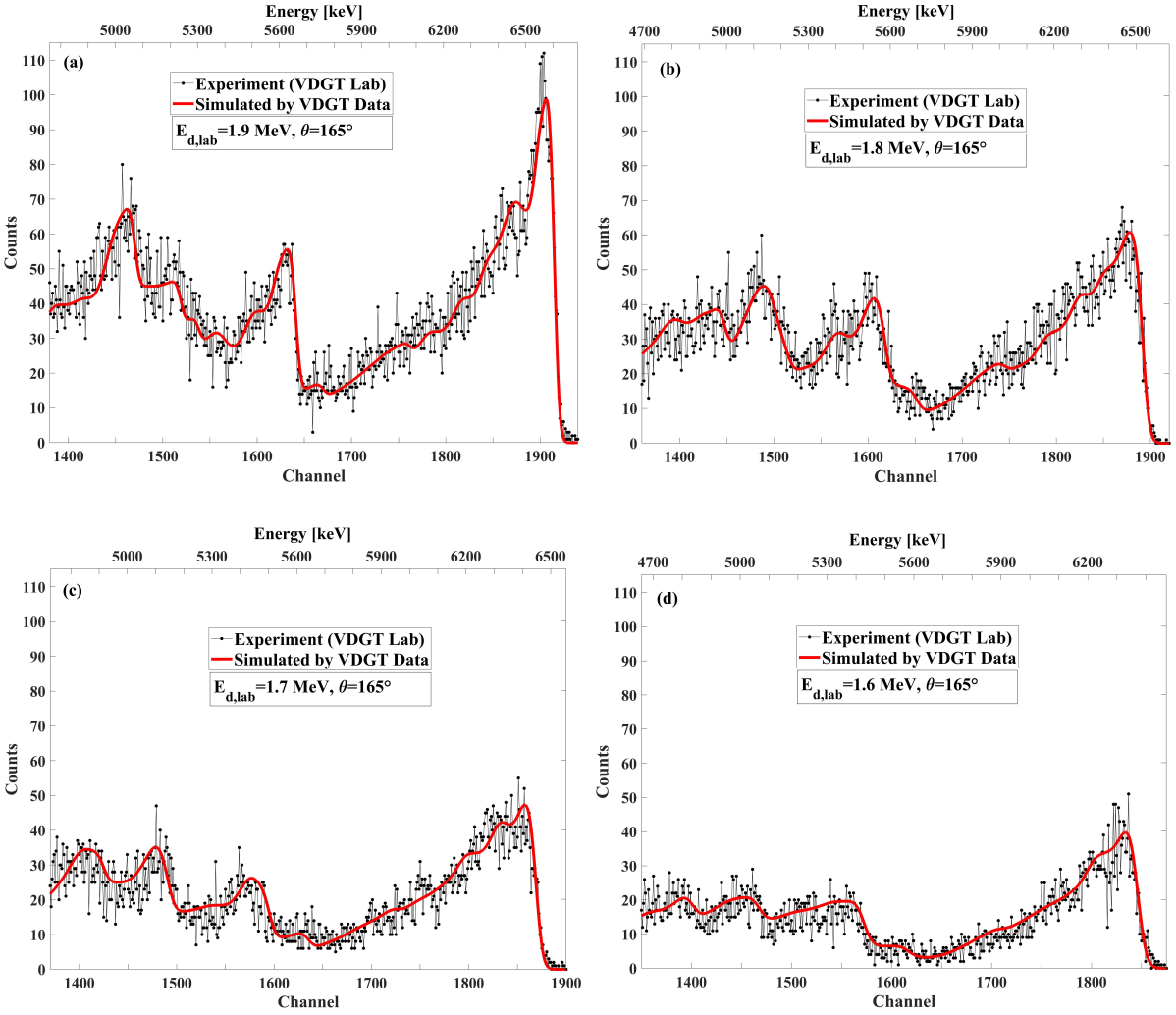

Figure 4.15: The benchmarking result at VDGT Lab in Tehran with measured VDGT data at 165° and different incident deuteron energies, (a) 1.9 MeV, (b) 1.8 MeV, (c) 1.7 MeV and (d) 1.6 MeV.

separately into IBANDL.

4.6 Conclusions

The ^{27}Al(d,p$_{0+1,2+3,4,5+6}$)^{28}Al and ^{27}Al(d, $\alpha_{0,1,2,3,4}$)^{25}Mg reaction cross sections were measured at VGDT (Tehran) on thin self-supporting aluminium targets for incident deuteron energies in the range 1.4 to 2 MeV at 135°, 150°, and 165° laboratory scattering angles. The measurements for 150° were independently repeated on the SAFIR platform at INSP and showed close agreement with the VDGT data. The cross sections at 150° were evaluated with existing data sets and an N=20 Fourier series fit is proposed to embody the evaluated cross section. The evaluated cross-sections have been benchmarked through a series of thick target spectra of charged particles induced by deuteron beams from a

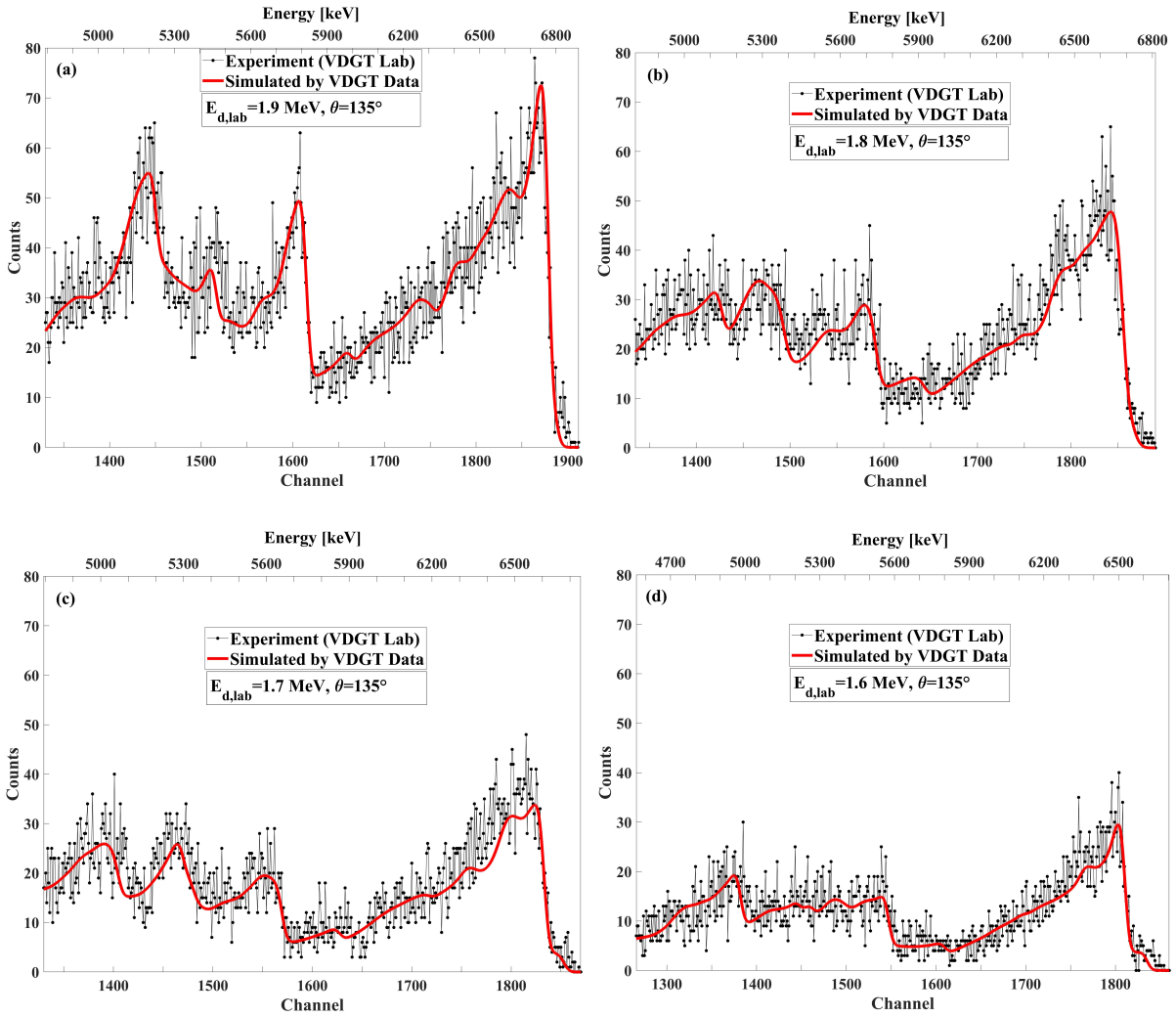

Figure 4.16: The benchmarking result at VDGT Lab in Tehran with measured VDGT data at 135° with different incident deuteron energies, (a) 1.9 MeV, (b) 1.8 MeV, (c) 1.7 MeV and (d) 1.6 MeV.

pure aluminium target, under various detection conditions at both VDGT and INSP. The overall agreement between the spectra simulated by SIMNRA and the measured benchmarking spectra is most satisfying and validates the evaluated cross sections presented here. We therefore recommend the use of these evaluated cross sections for use in NRA. We note that the recommended cross sections for 135° and 165° are the first ^{27}Al(d,p) and ^{27}Al(d,α) cross sections to be benchmarked at these angles for NRA.

4.7 Acknowledgements

We are particularly indebted to S. Steydli (INSP) for assistance in mechanical and vacuum aspects, and H. Tancrez (INSP) for electronic and command-control systems development. We also are grateful to the Electron Microscopy Platform of IMPMC, Sorbonne Université

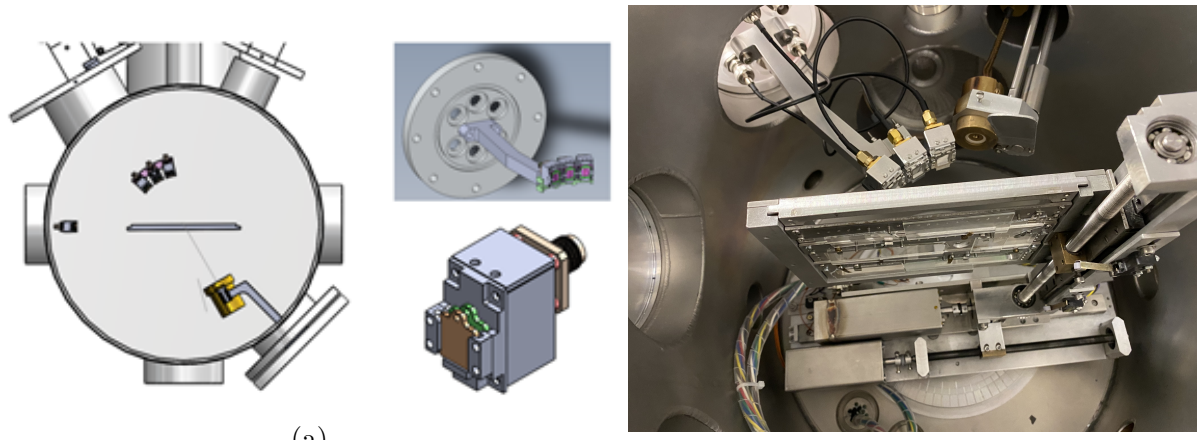

(a) (b)

Figure 4.17: (a) Simulation of multi-detector holder, (b) Set up of three pin detectors with 100 μm mylar in front of the detector.

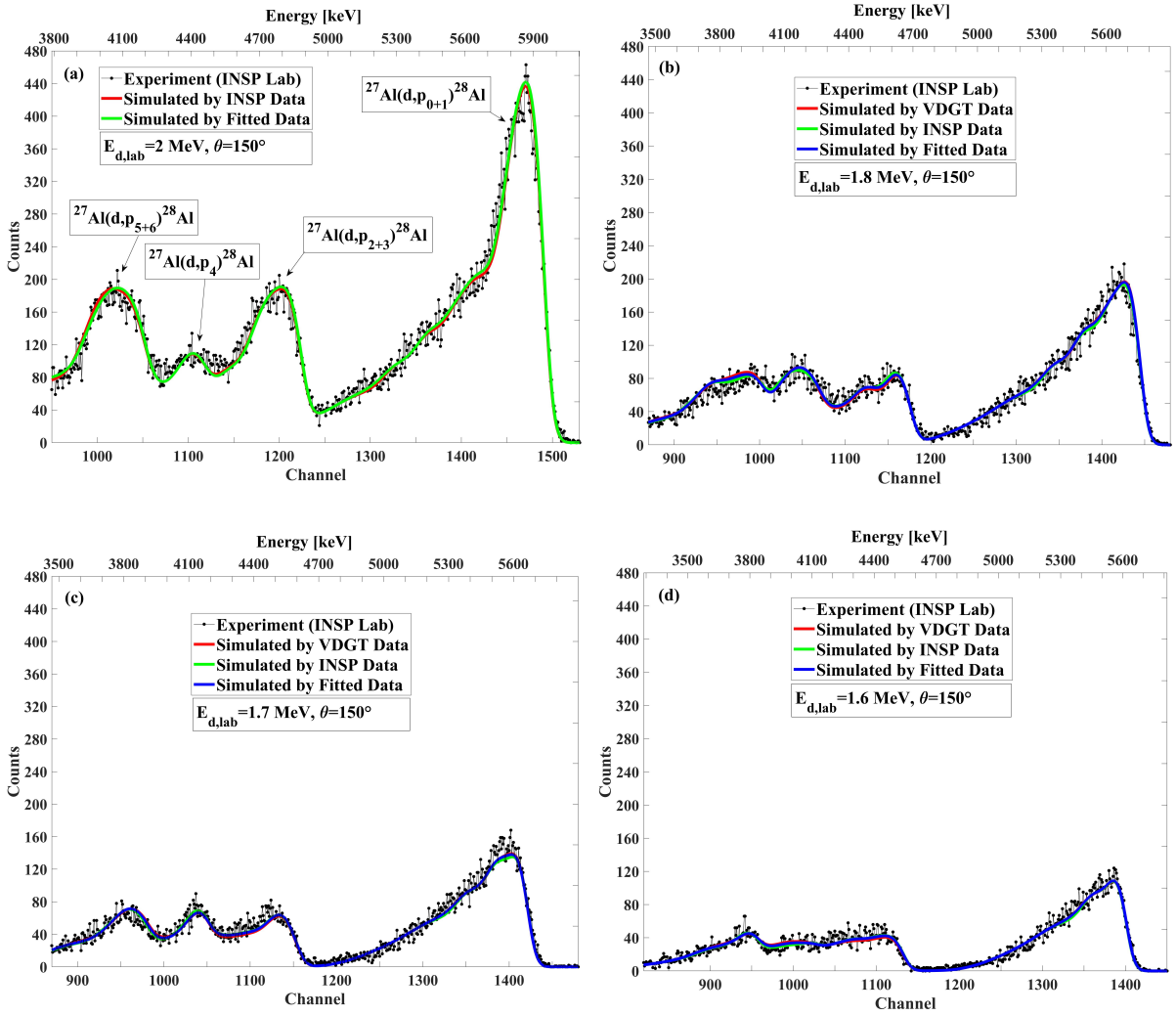

Figure 4.18: The benchmarking result at INSP Lab in Paris with different data set at 150° for incident deuteron energies of (a) 2MeV, (b) 1.8 MeV, (c) 1.7 MeV, (d)1.6MeV.

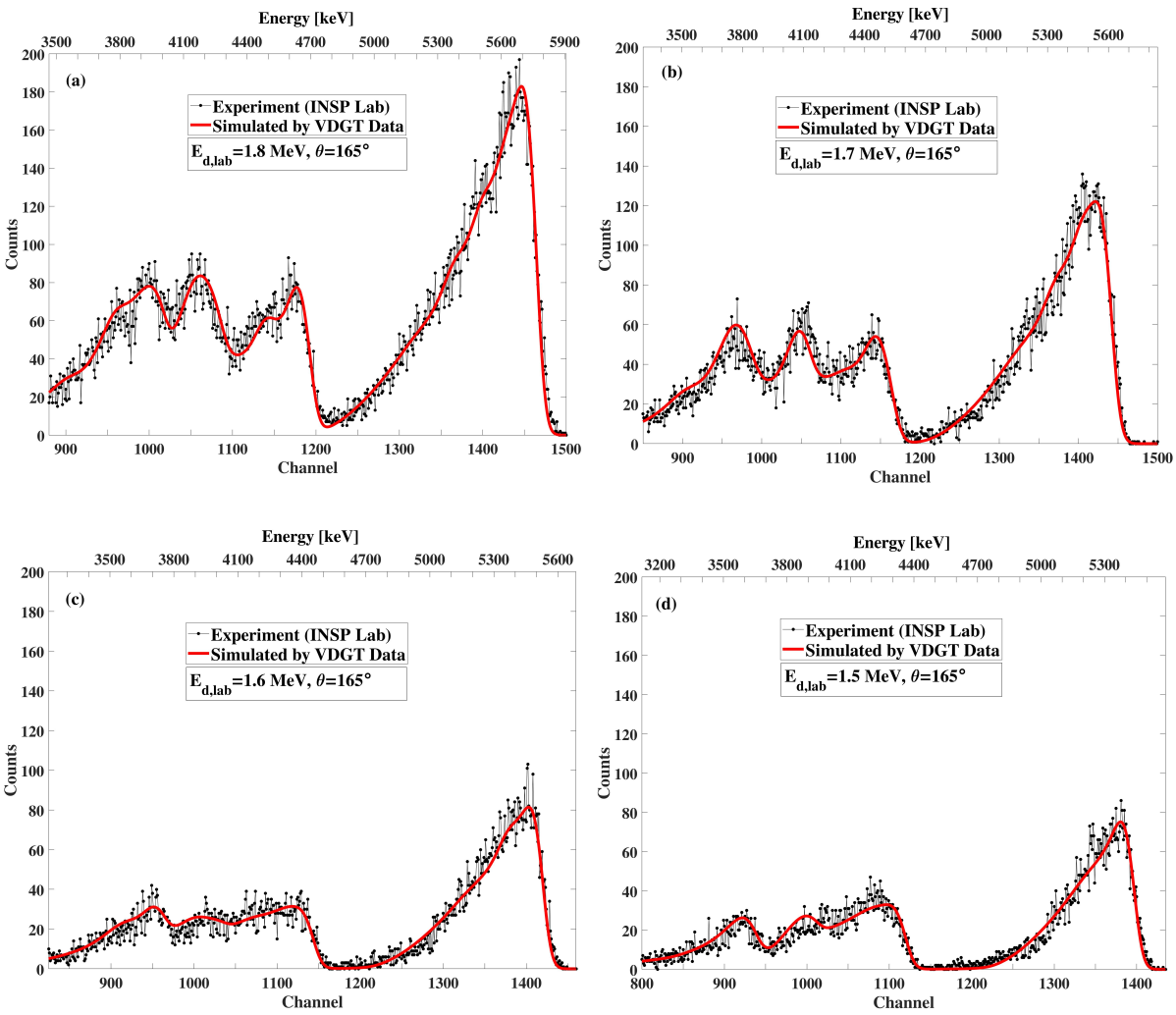

Figure 4.19: The benchmarking result at INSP Lab in Paris with measured VDGT data at 165° for different incident deuteron energies of (a) 1.8 MeV, (b) 1.7 MeV, (c) 1.6 MeV, (d)1.5 MeV.

for assistance in obtaining the image of Figure 4.2. M. Salimi would also like to express her deep appreciation of the strong support of M. Marangolo (Director of INSP) and N. Witkowski (Directrice of the Doctoral School) for her co-tutelle doctoral contract. M. Salimi gratefully acknowledges the contribution from CAMPUS FRANCE in support of her co-tutelle doctoral contract.

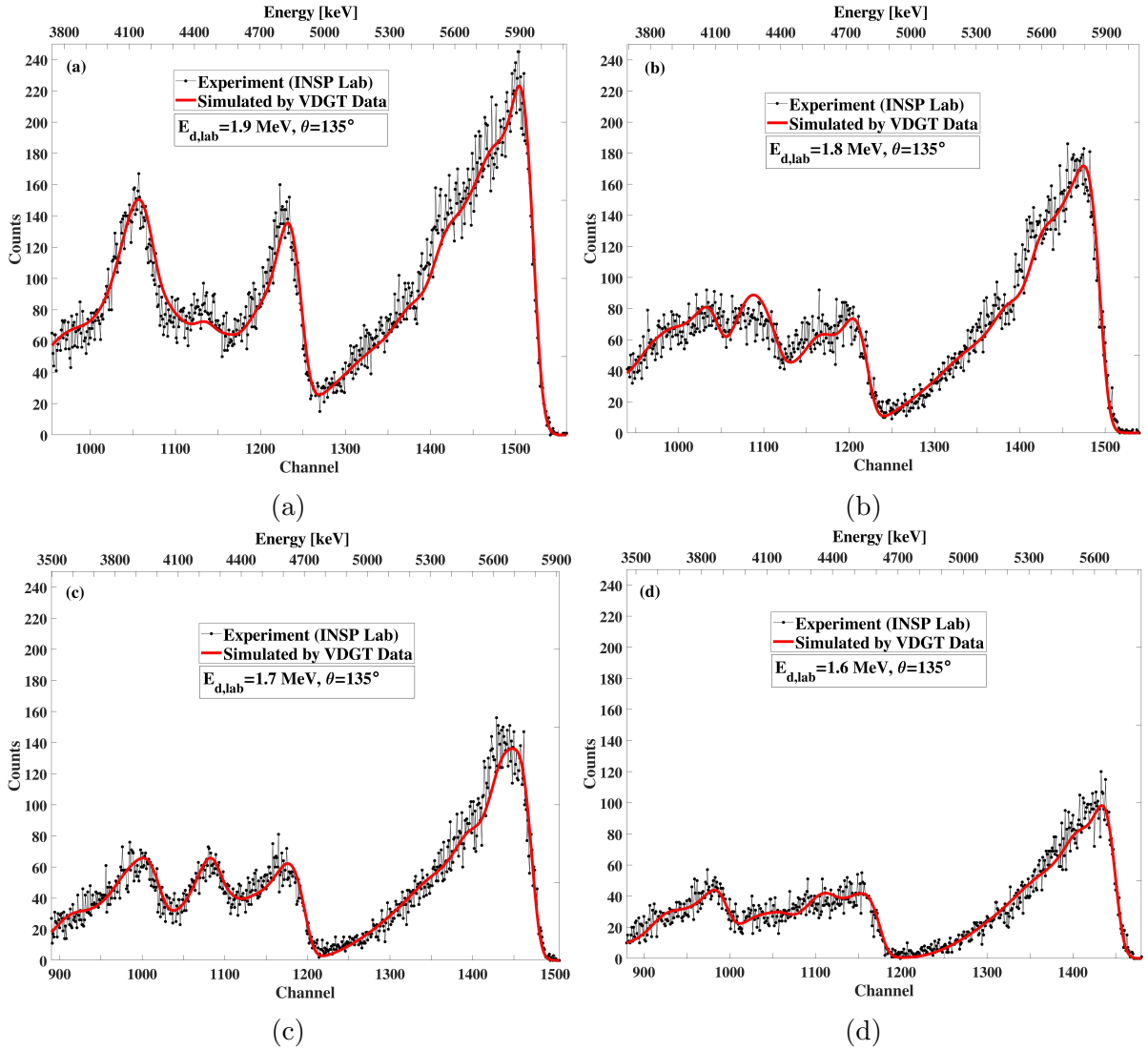

Figure 4.20: The benchmarking result at INSP Lab in Paris with measured VDGT data at 135° for different incident deuteron energies of (a) 1.9 MeV, (b) 1.8 MeV, (c) 1.7 MeV, (d)1.6 MeV.

Chapter 5

Measurement of (p,p) elastic different cross sections for ^{17}O in the 0.6-2 MeV range at 165°

This chapter is published paper by Nuclear Instruments and Methods in Physics Research Section B: Beam Interactions with Materials and Atoms (NIMB) journal [3] .

M. Salimi[1,2], O. Kakuee[3], S.F. Masoudi[1], H. Rafi kheiri[3], E. Briand[2], J-J. Ganem[2], I. Vickridge[2]

[1]Department of Physics, K.N. Toosi University of Technology, P.O. Box 15875-4416, Tehran, Iran
[2]Sorbonne Université, CNRS, Institut des NanoSciences de Paris, INSP, SAFIR, F-75005 Paris, France
[3]Physics and Accelerators Research School, NSTRI, PO Box 14395-836, Tehran, Iran

Abstract

$^{17}O(p,p)^{17}O$ elastic scattering cross sections were measured for the first time, on the INSP SAFIR platform in Paris, using thin silica films prepared by thermal oxidation of Si under $^{17}O_2$. The ^{17}O content of the film was determined by a combination of ellipsometry and IBA measurements.

The yield of elastically scattered protons was determined from the corresponding peak in the Elastic Backscattering spectra, with the underlying Si signal reduced by channeling of the incident beam in the silicon substrate. The measured $^{17}O(p,p)^{17}O$ cross section was determined with a systematic uncertainty of about 14%. The cross section consists of resonant structures superimposed on a smoothly varying component that increases from about 1.2 times the Rutherford cross section at 600 keV to about 3 times Rutherford at 2 MeV. A resonance at 1230 keV shows promise for proton Elastic Backscattering depth profiling, especially at large backscattering angles. The cross section is available on IBANDL (www-nds.iaea.org/ibandl/).

5.1 Introduction

Proton elastic backscattering spectrometry (EBS) is a powerful method which has been widely used for accurate analysis of materials, such as impurity distributions in thin layers, determination of stoichiometry and elemental areal density. Compared to alpha particle EBS, proton EBS offers useful excursions from the Rutherford cross section, such as enhancements and resonant structures, at lower beam energy than for alpha particle EBS, whilst allowing a similar analysis depth [118–120]. Non-Rutherford proton EBS may thus be used on accelerators with lower energies than those required for EBS with alpha particles. For example, the ^{16}O(α,α) and ^{18}O(α,α) elastic scattering cross sections are Rutherford below 2 MeV. Although that for ^{17}O has not been measured, it too is highly likely to be Rutherford below 2 MeV. The lower Coulomb repulsion between incident protons and the target nucleus means that the nuclear potential influences the elastic scattering cross section at lower energies than those for alpha elastic scattering, such as that of the well-known narrow resonance at 3.042 MeV in ^{16}O(α,α)^{16}O [4, 5].

The ^{16}O(p,p) EBS cross section is usefully greater than Rutherford between 1 MeV and 2 MeV (Figure 5.1) but it is slowly varying and there is no useful resonant structure below 2 MeV [86, 121]. As seen in Figure 5.2, ^{18}O(p,p) has a useful narrow resonance at about 1750 keV. Low energy narrow resonances such as ^{18}O(p,α) at 151 keV [122, 123] in reactions with high Q-values have been used for concentration depth profiling of ^{18}O so that there has been no push to apply the EBS resonance. The ^{17}O(p,α) reaction has a number of narrow resonances, however the low Q-value of 1197 keV means that it is not possible to choose an appropriate thickness for a foil in front of the detector that will allow detection of the alpha particles, but stop the large flux of elastically scattered protons from entering the detector. The higher EBS cross section and simplified equipment needs (no need for high precision beam energy scanning or specialized large area detectors) could make ^{18}O EBS attractive for wider application to stable isotopic tracing, and in this vein, we have also considered ^{17}O EBS. Whilst ^{16}O and ^{18}O have nuclear spin of zero, we note that ^{17}O has a nuclear spin of 1/2, and can also be used in electron paramagnetic tracing experiments where the spin-orbit coupling renders the response of the ^{17}O nucleus sensitive to its nearest neighbor configuration.

Although we could find no published measurements of ^{17}O(p,p) cross sections, extensive measurements of yield curves have been made using thin self-supporting SiO or gas targets [124, 125]. These measurements, aimed at nuclear physics studies, were concerned with the energies and widths of ^{18}F nuclear levels and so absolute cross sections were not required. In addition, for a significant part of the incident proton energy range of interest here, of 600 to 2000 keV [124] the authors of the work were only able to use oxygen gas enriched to 76.6% in ^{17}O, with contamination of 18.2% in ^{18}O and 5.2% in ^{16}O. Properly correcting the measured yields (the three isotopes are probably not re-

solved in the charged particle energy spectra) would require absolute measurements of the ^{17}O(p,p) cross section and knowledge of the ^{18}O(p,p) and ^{16}O(p,p) cross sections at the angles and energies where the ^{17}O(p,p) yields were measured. The authors therefore simply subtracted 23% of the counts from the non-resonant amplitude. This procedure is probably valid for extracting the level parameters in energy regions where the ^{18}O(p,p) and ^{16}O(p,p) cross sections are varying slowly, but does not guarantee that the measured shape of the yield curve from this gas target is the same as the shape of the cross section. Yield curves were also measured [125] for incident particles in the energy range of 1.4 MeV to 3 MeV, using a thin self-supporting target. The backscattered protons from the three oxygen isotopes could be resolved, at least at backward angles and for the higher incident beam energies, however this energy range does not include a major region of interest here, for the exploitation of low energy proton EBS. We therefore measured the ^{17}O(p,p) cross section in the range from 600 keV to 2 MeV at 165°, the most widely used RBS scattering angle. We will show that the yield curves from ref [124] are significantly distorted by the contribution from ^{18}O(p,p) and thus, unfortunately, cannot be simply re-scaled to be used as cross sections for accurate IBA. We will also show discrepancies between our measurements and those of ref [125].

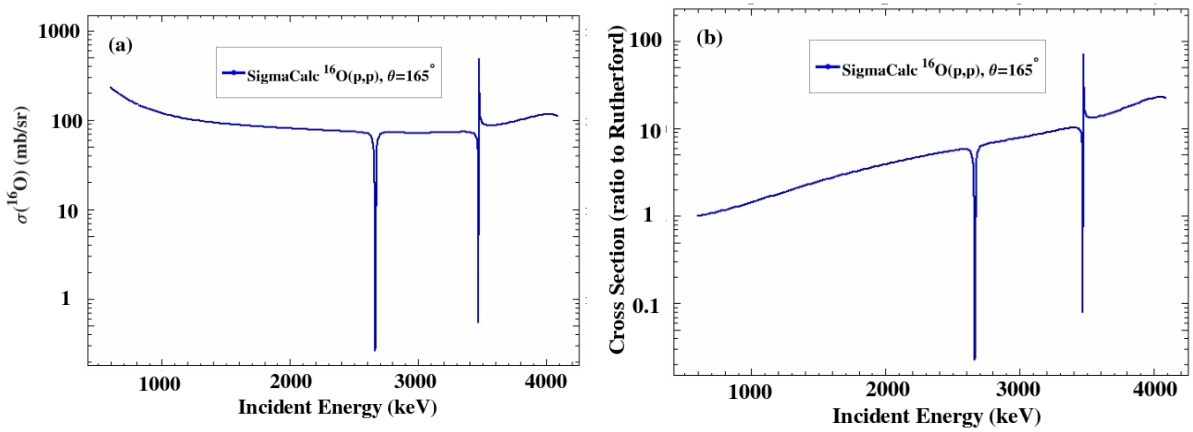

Figure 5.1: a) Cross section and b) The ratio to the Rutherford cross section of ^{16}O(p,p) ^{16}O at 165° (sigmacalc) [86]

5.2 Experimental Methods

Our experimental work was carried out in the channeling chamber on the 30° right beamline of the 2.5 MV Van de Graaff SAFIR (Système d'Analyse par Faisceaux d'Ions Rapides) platform at INSP (Institut des NanoSciences de Paris). During the measurements, the chamber pressure was about 1×10^{-6} mbar. A 300 μm thick, 300 mm^2 surface barrier detector at scattering angle of 150° was used for NRA, and a 100 μm thick, 25 mm^2

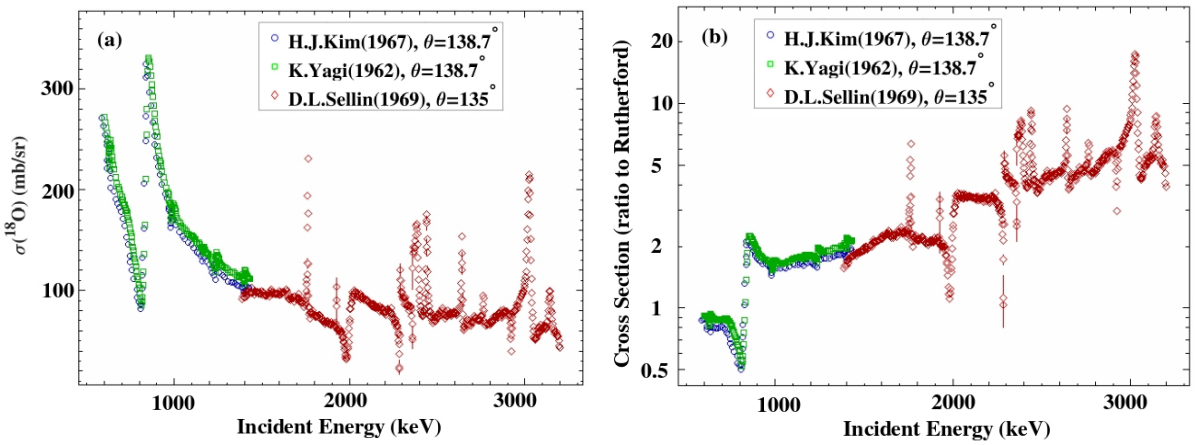

Figure 5.2: a) The differential cross section of ^{18}O(p,p)^{18}O near 135° and b) its ratio to Rutherford [126–128].

surface barrier detector at scattering angle of 165°, collimated to exclude edge effects, was used for RBS and EBS measurements. Pulses from the CAEN A1422 preamplifier were treated in a digital data acquisition system based on a CAEN DT5725 digital pulse processor to provide particle energy spectra.

5.2.1 Energy calibration of the accelerator

The accelerator energy calibration procedure, based on energies of narrow (p,γ) resonances and the signal from the generating voltmeter, is described in ref. [2].

5.2.2 Measurement of the detector solid angle-charge product

The detector solid angle-charge product was first determined by RBS, using a standard Bi-implanted Si reference (Ref Bi =5.64 $\times$ 10^{15} at/cm^2) with an uncertainty of 2%–3%. RBS measurements were performed with a 30 nA, 1.8 MeV alpha particle beam of 0.5mm, and detection at 165°. Total deadtime was less than 10% and was corrected for. The entire vacuum chamber is insulated from ground and is used as a Faraday cup for charge integration, with reproducibility better than 1%. The vacuum of the reaction chamber was about 10^{-6} mbar and the integrated beam charge for each measurement was 10 μc.

The parameter $\Omega \times Q$ was defined by RBS as eq. 5.1:

$$\Omega \times Q = \frac{Y_{Bi}}{N_{Bi}\sigma_{Bi}} \tag{5.1}$$

where Q, Ω, Y_{Bi}, N_{Bi} and σ_{Bi} represent the charge, the solid angle, the experimental yield of Bi (net area under the Bi peak), and the Rutherford cross section of Bi. as defined here will be used in the following experimental work.

5.2.3 Target preparation

Ideally, gas targets [124], or thin self-supporting targets such as those prepared by anodic oxidation by Amsel for the extensive early ^{16}O and ^{18}O nuclear reaction cross section measurements [129], should be used for these measurements, however we have neither a supply of water highly enriched in ^{17}O for anodic oxidation, nor a gas target chamber and detection system. Although it has been shown to be possible to fabricate thin self-supporting targets [125], our attempts (e.g. by oxidising Al [2]) were also unsuccessful, and so we used thermal silica layers of thicknesses near 100 nm, grown on ⟨100⟩ oriented silicon wafers by thermal oxidation at 1100 °C in dry $^{17}O_2$ gas in a quartz tube vacuum furnace with a base pressure of 10^{-6} mbar. The choice of silicon substrate has the advantage that the oxidation methods and thermal oxide characteristics are very well known [80]. The disadvantage of this target is that the protons are elastically backscattered from oxygen atoms in the thin oxide surface layer with a lower energy than those backscattered from the silicon, and so the corresponding ^{17}O peak in the spectrum sits on a large and non-Rutherford background of protons scattered from Si, as may be seen in Figure 5.3. This complicates peak area extraction. Thermal ^{17}O oxides could conceivably be made on heavier substrates where the substrate signal would at least be Rutherford, but of course in this case the substrate signal amplitude would swamp the ^{17}O elastic scattering signal.

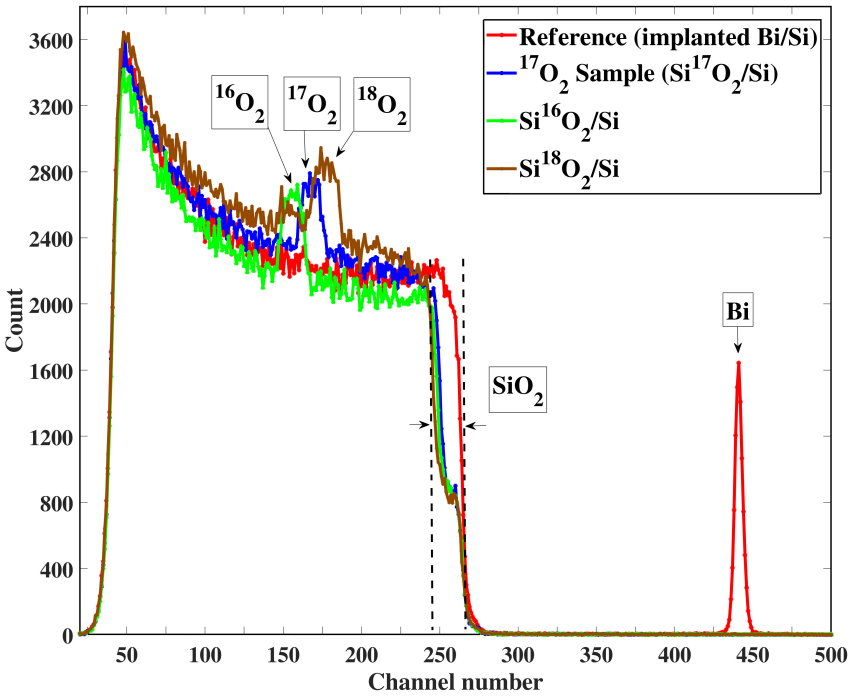

Figure 5.3: The typical measured RBS spectra of the three isotopically enriched oxide targets and the Bi reference at scattering angle 165° and E_α = 1.8 MeV.

We also made samples in $^{16}O_2$ and $^{18}O_2$ gas under the same conditions. RBS spectra

from samples highly enriched in each of the stable isotopes, together with a spectrum from the Bi reference, are shown in Figure 5.3. The signals from the three oxygen isotopes can be clearly identified, but the overlap of the signals means that RBS is not particularly well suited to determining small quantities of the adjacent masses in the wings of a major component. In our case, this is true for the determination of small quantities of ^{16}O and ^{18}O in the presence of a large majority of ^{17}O. Nevertheless, the spectra are very sensitive to the overall silica thickness, through the energy at which the silicon signal increases from that in the silica layer to that of the silicon substrate.

5.2.4 Characterization of the thin target

5.2.4.1 Measurement of the total amount of O by ellipsometry

The thermal oxide of silicon, grown at 1100°C in pure oxygen, is expected to be very close to stoichiometric [80]. We measured the physical silica thickness and refractive index by ellipsometry. The refractive index at 633 nm varied slightly between 1.47 and 1.48, very close to the refractive index of stoichiometric fused silica which is 1.46 [130]. This provides strong support of the affirmation that this thermal oxide is indeed stoichiometric SiO_2. The density of the thermally grown silica on silicon is taken to be 2.21 g/cm^3 [131]. The small variations in refractive index probably indicate small variations of density, however these would be less than 1% [130], and so an uncertainty of 1% is ascribed to the silica film density, which is used to calculate the total oxygen atomic areal density, assuming stoichiometric SiO_2. Film physical thickness was determined with about 1% uncertainty.

5.2.4.2 Measurement of the areal density of ^{18}O

The areal density of ^{18}O[N_{18_O}] was determined by NRA with the ^{18}O(p,α)^{15}N reaction [128], which has a high Q-value of 3.97 MeV, providing an isolated peak. The peak of the cross section near 830 keV was used to provide high yields. The beam lost only about 5 keV in the targets and so the cross section hardly varied across the thickness of these samples. A 10μm mylar film was used in front of the 300-μm-thick surface barrier detector, placed at detection angle of 150°, to stop the high flux of protons scattered from the silicon. Absolute values of the areal density N_{18_O} were determined by comparing yields with a standard thermal Si^{18}O$_2$/Si (Ref ^{18}O= 380 $\times$ 10^{15}at/cm^2), with an uncertainty of 2%–3%. Typical spectra are shown in Figure 5.4.

5.2.4.3 Measurement of the areal density of ^{16}O

The areal density of ^{16}O[N_{16_O}] was determined by NRA with the ^{16}O(d, p$_1$)^{17}O reaction [78, 118] with a deuteron beam of 860 keV. The protons from the reaction were detected with a 300μm thick surface barrier detector placed at 150° scattering angle. A 16 μm

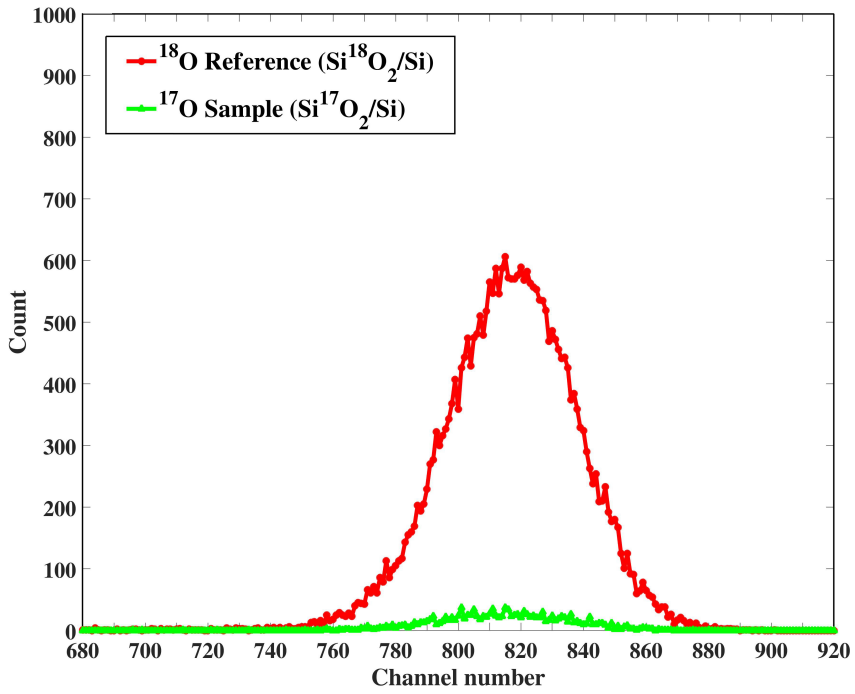

Figure 5.4: The typical measured p-NRA spectra obtained from the ^{17}O enriched silica layer used for the cross section measurements, and a reference thin silica layer of natural isotopic composition at scattering angle 150° and E_p = 830 keV.

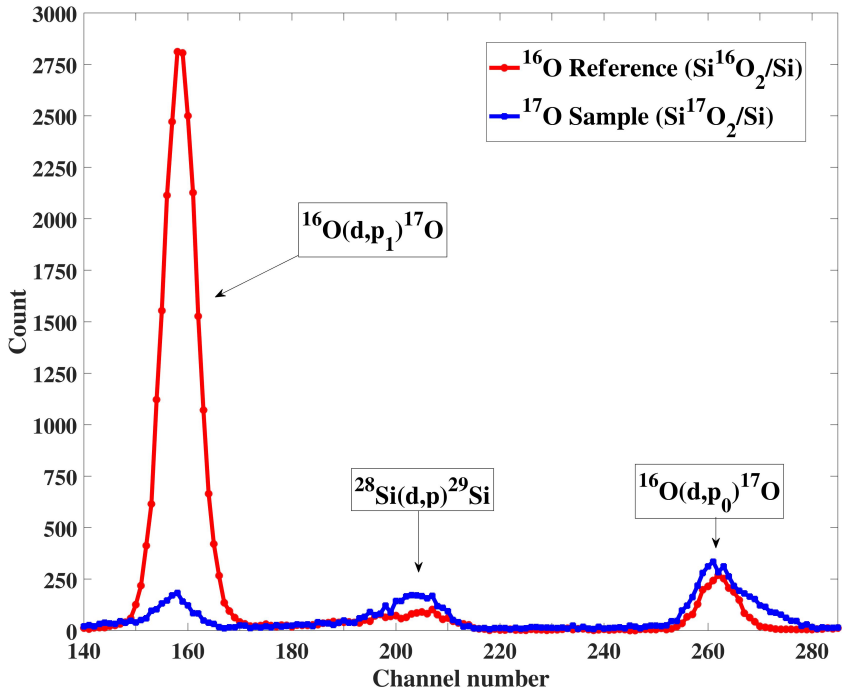

Figure 5.5: Typical NRA spectra obtained from the ^{17}O enriched silica layer used for the cross section measurements, and a reference thin silica layer of natural isotopic composition.

mylar film in front of the detector stopped elastically scattered deuterons while allowing the energetic protons into the detector.] was determined with an uncertainty of 3% by

comparing proton yields with the proton yield from a standard thermal $Si^{16}O_2/Si$ film (Ref $^{16}O = 624.8 \times 10^{15}\ at/cm^2$). Typical NRA spectra are shown in Figure 5.5. Note that in the spectrum obtained from the ^{17}O enriched sample, there is a significant interference in the $^{16}O(d,p_0)$ peak from $^{17}O(d,p_4)$, however there is no proton group from $^{17}O(d,p)$ that could interfere with the $^{16}O(d, p_1)$ peak.

5.2.4.4 Final target composition

A target of 107±1 nm silica thickness was chosen for the cross section measurements. The total oxygen content from ellipsometry was $467 \times 10^{15}\ at/cm^2$, of which $18.2 \times 10^{15}\ at/cm^2$ were ^{18}O and $33.8 \times 10^{15}\ at/cm^2$ were ^{16}O. The areal density of $^{17}O[N_{17_O}]$ in the sample was calculated to be $415 \times 10^{15}\ at/cm^2$ with an estimated uncertainty of about 5% mainly arising from counting statistics.

The film thickness deduced from RBS of this target, simulated supposing stoichiometry and a density of $2.21\ g/cm^{-3}$, is 105 nm. This is very close to the physical thickness measured by ellipsometry, indicating that the compound stopping power used in the SIMNRA calculation is reliable. Since the SIMNRA Ziegler/Biersack alpha particle stopping powers are scaled from proton stopping powers, this shows that it is reasonable to assume that the calculation of the average energy of the incident protons in the layer, for each of the incident energies chosen, is also reliable.

5.2.5 Determining the total oxygen peak area

5.2.5.1 Background suppression by ion channeling

For the ^{17}O target, which consists of a $Si^{17}O_2$ layer on a Si substrate, ion channeling is useful to suppress the background from the silicon substrate, allowing more accurate estimation of the area of the total oxygen peak (Y_{total_O}). As shown in Figure 5.6 the differential cross section of $^{nat}Si(p,p)$ around the energy 1670 keV is very high and rapidly varying. Under some conditions, this rendered determination of the oxygen peak area impossible, as may be seen in Figure 5.7c. Here, channeling the incident beam in the substrate allowed the oxygen peak to be observed and its area estimated.

The sample was first aligned with an alpha particle beam, for which the critical channeling angles, larger than those of the proton beam, facilitate alignment. The alignment was refined with the proton beam. We noted no beam damage effects on the channeling spectra during the measurements, however it is to be noted that we are not very sensitive to damage effects since the amorphous oxide layer on the surface induced significant beam angular spread and minimum silicon yields were only about 30%, rather than the typical values of a few percent for fully crystalline structures.

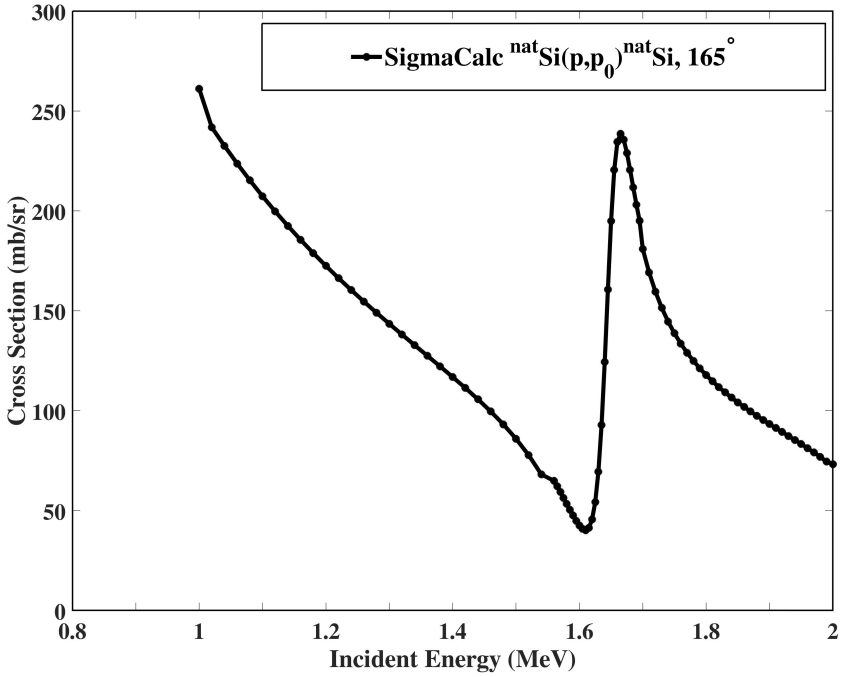

Figure 5.6: ^{nat}Si(p,p) differential cross section curve

5.2.5.2 Background subtraction

Our experiment requires extracting the area of the total oxygen peak (Y_{total_O}), which is sitting on a large Si background that cannot be analytically modelled. In order to adjust a phenomenological background, we developed a user-friendly program which allows us to adjust a polynomial of arbitrary order, defined by the shape of the background curve only outside of the peak region, as shown in the regions between the two red cursors and the two blue cursors in Figure 5.8. Because there is no a priori background shape, the goodness of the background is judged by the user. In all cases, the minimum possible polynomial order q was chosen, and uncertainties are estimated from fits based on extreme parameters for the definition of the fitting regions (outside the peak region) for which the background in the peak region is clearly erroneous, together with Monte Carlo uncertainty estimation using simulated data.

5.3 Results and discussion

The differential cross section of ^{17}O(p,p) was measured in the present work for $E_{p,lab}$ = 0.6–2 MeV with 10 keV energy steps in most regions and 2 keV steps around the resonances (in Figure 5.9).

The differential cross-sections for proton EBS on $^{17}\mathrm{O}\left(\frac{d\sigma}{d\Omega}\right)_{\theta,E(^{17}O(p,p))}$ at detection angle

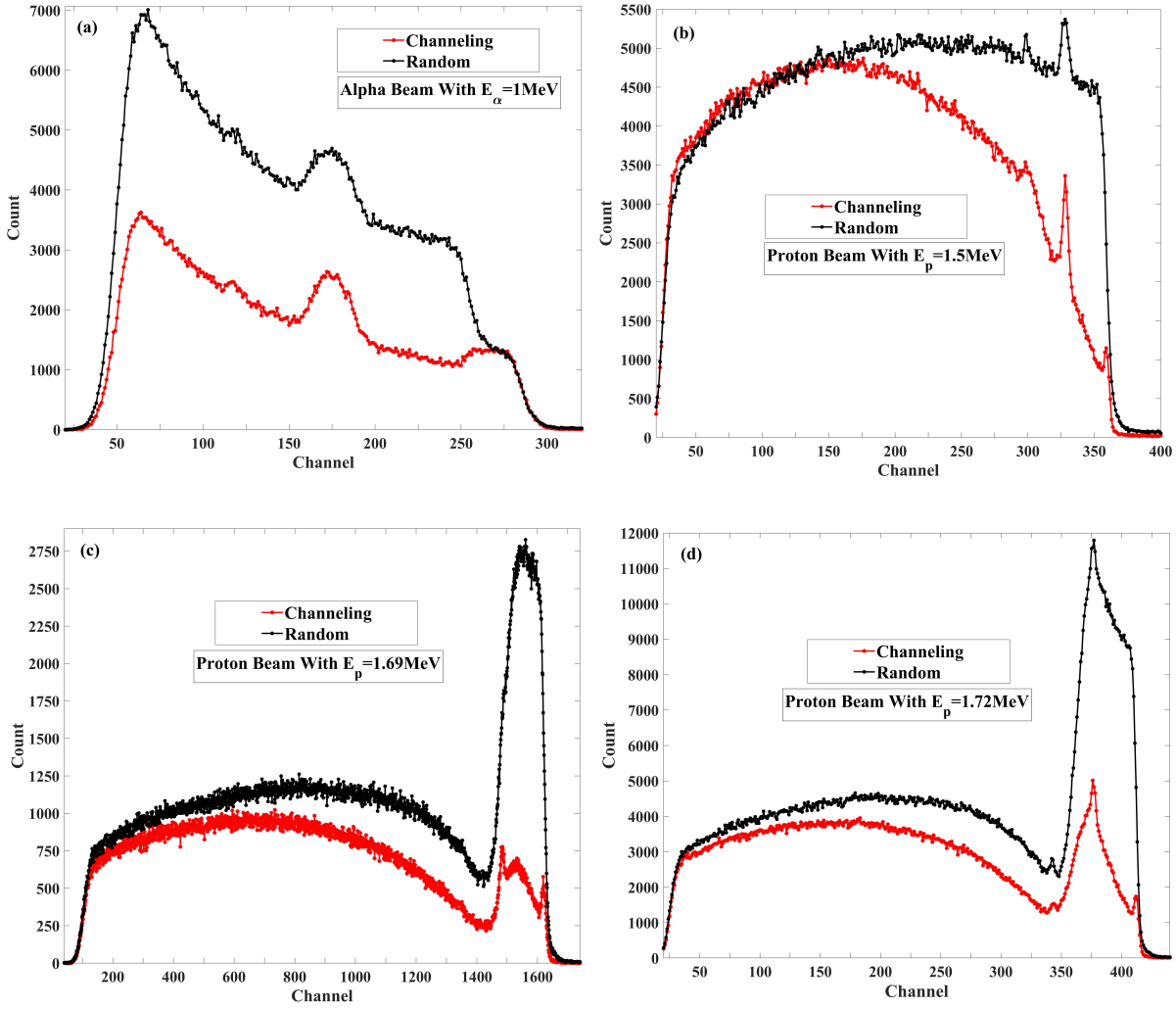

Figure 5.7: The comparison between channelling and random peak at different with a) alpha beam with E_α=1 MeV, and proton beam with b) E_p=1.5 MeV, c) E_p=1.69 MeV and d) E_p=1.72 MeV.

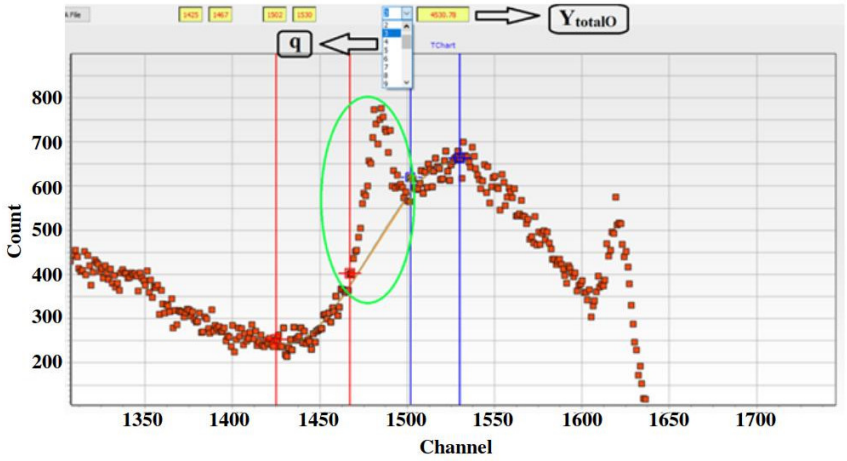

Figure 5.8: Polynomial background determined for the spectrum of Figure 5.7c, obtained with the proton beam aligned with the Si substrate < 100 > direction.

θ and incident proton energy E_p were obtained from Eq. 5.2:

$$\left(\frac{d\sigma}{d\Omega}\right)_{\theta,E(^{17}O(p,p))} = \frac{Y_{^{17}O,E_p}}{\Omega \times Q \times N_{^{17}O}} \tag{5.2}$$

with $Y_{^{17}O,E_p} = Y_{total_{O,E_p}} - Y_{^{18}O,E_p} - Y_{^{16}O,E_p}$; $Y_{^{16}O} = \Omega \times Q \times N_{16_O} \times \sigma_{16_{O(p,p)}}$, and $Y_{^{18}O} = \Omega \times Q \times N_{18_O} \times \sigma_{18_{P(p,p)}}$ where $\Omega \times Q$, N_{18_O} and N_{16_O} were measured by ellipsometry as described in section 5.2.4.1 , p-NRA in section 5.2.4.2 and d-NRA in section 5.2.4.3, respectively. $Y_{total_{O,E_p}}$ is defined in section 5.2.5.

$\sigma_{16_{O(p,p)}}$was calculated by Sigmacalc at 165° at IBANDL with an energy step of 20 keV [86]. This calculation was interpolated by MATLAB to have the cross-sections of ^{16}O(p,p) for any arbitrary range of energy between 600-2000 keV. We could find no cross section data for 165° scattering angle, and so we used the closest existing data. $\sigma_{18_{O(p,p)}}$ was therefore derived from the only two measured data in IBANDL: ref [127] in the energy range 590-1430 keV at 138.7° and ref [128] in the energy range 1.39 – 3.20 keV at 135°, also interpolated with MATLAB to give values for any required energy.

Finally, the proton scattering cross section for ^{17}O at 165° for E_p=0.6–2 MeV in the laboratory system is presented in Figure 5.9a with the ratio to the Rutherford cross section being shown in Figure 5.9b. The energy values take into account the finite energy loss in the silica layer, which ranges from 5.8 keV at 600 keV incident energy, to 2.7 keV for 2MeV incident protons. The systematic uncertainty is 14% (1σ) according to the standard error propagation formulas, including the uncertainty in identifying the contents of different isotopes of oxygen and the product . The uncertainty in the oxygen peak area determination, estimated by Monte Carlo treatment of the peak area extraction method (i.e. including variation in operator performance), is mostly between 4% and 6% and ranges from 3% to about 8% according to the peak intensity and the size and shape of the background to be estimated. The greatest uncertainty of 8% was obtained for the spectrum of Figure 5.7d.

There is an intense resonance with a maximum intensity at 1230 keV, of width about 4.5 keV after subtraction in quadrature of the target energy width of about 4 keV. We have also overlapped the scaled yield curves for θ_{cm}=161° from [124] and θ_{cm}=171° from [125]. The resonance energies are in good agreement with our measurement if the energy scale from [124] is scaled by 0.99. It is clear that the structure in the ^{18}O(p,p) cross section, unaccounted for when correcting the yield curves for the significant ^{18}O contamination in the gas used in [124] has led to marked differences between the measured yield curve and the cross section. We also note that the intensity of the resonance in the yield curve, compared to the continuous component, is smaller than that for the cross section, however the width of this resonance in the yield curve is very close to the width of 4.5 keV that we have observed in the cross section. This would give a depth resolution of around 50 nm in Si when the beam energy is scanned around the resonance energy.

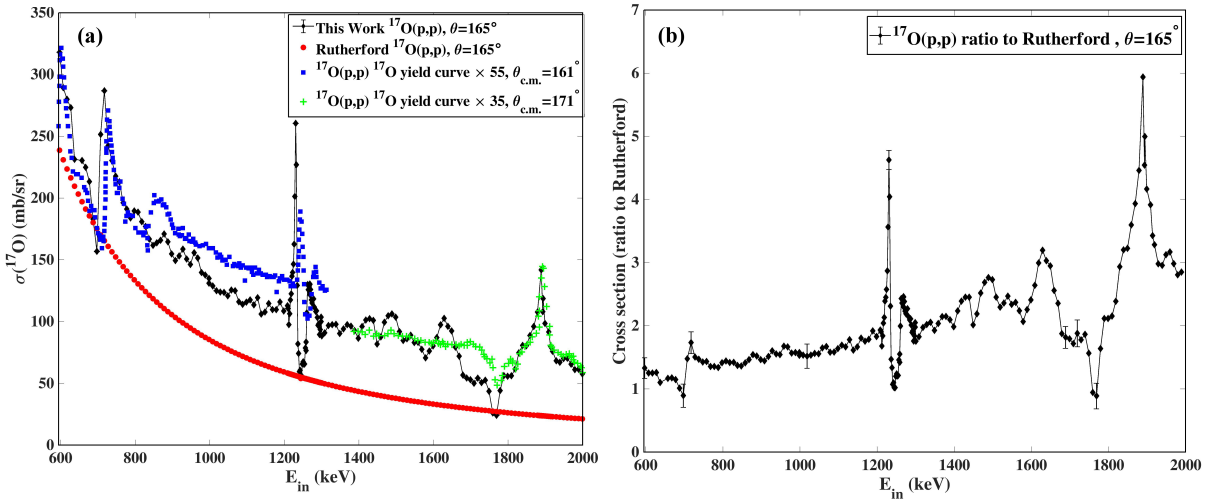

(a) (b)

Figure 5.9: a) Our measured proton elastic scattering cross section, compared with scaled yield curves from ref [124] and [125]. b) The ratio to the Rutherford cross section of ^{17}O at 165° for E$_p$=0.6–2 MeV in the laboratory system. The representative uncertainty bars in b) represent the statistical uncertainty.

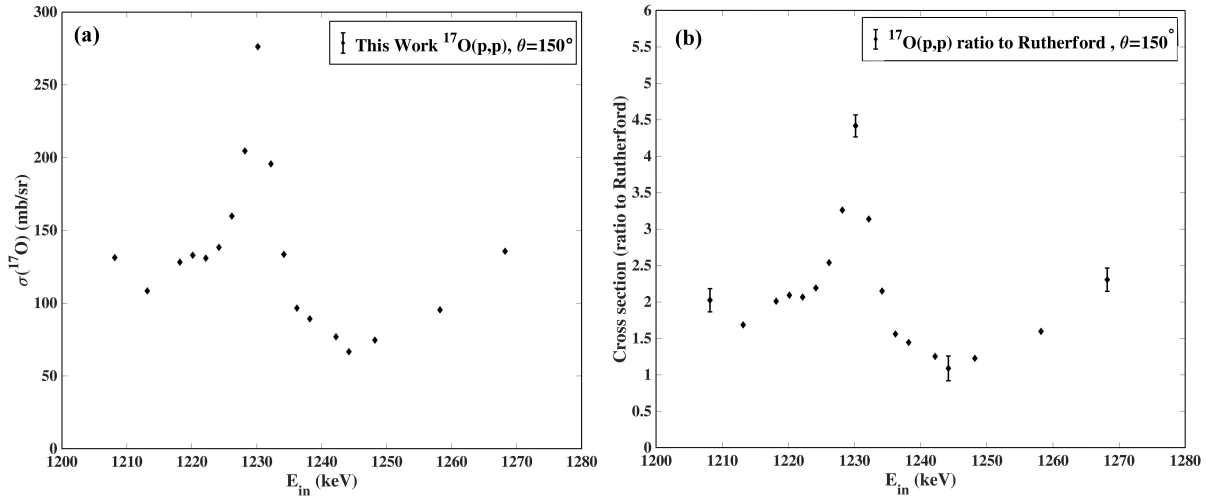

(a) (b)

Figure 5.10: a) Proton scattering cross sections and b) the ratio to the Rutherford cross section of ^{17}O(p,p)^{17}O at 150° for E$_p$=1.2–1.3 MeV in the laboratory system.

The yield curve from [125] was measured by the same group as that of [124], using a thin self-supporting target from which the protons scattered from ^{16}O and ^{18}O could be resolved from those scattered from ^{17}O. This yield curve, correctly scaled, should then represent the scattering cross section. There is a clear discrepancy between this scaled yield curve and our measurement below about 1.8 MeV. We cannot explain this discrepancy, however we note that the measured cross section is robust against possible systematic errors or bias in the delicate task of background subtraction, for which data reduction by two independent analysts yields results within the estimated random uncertainty margins.

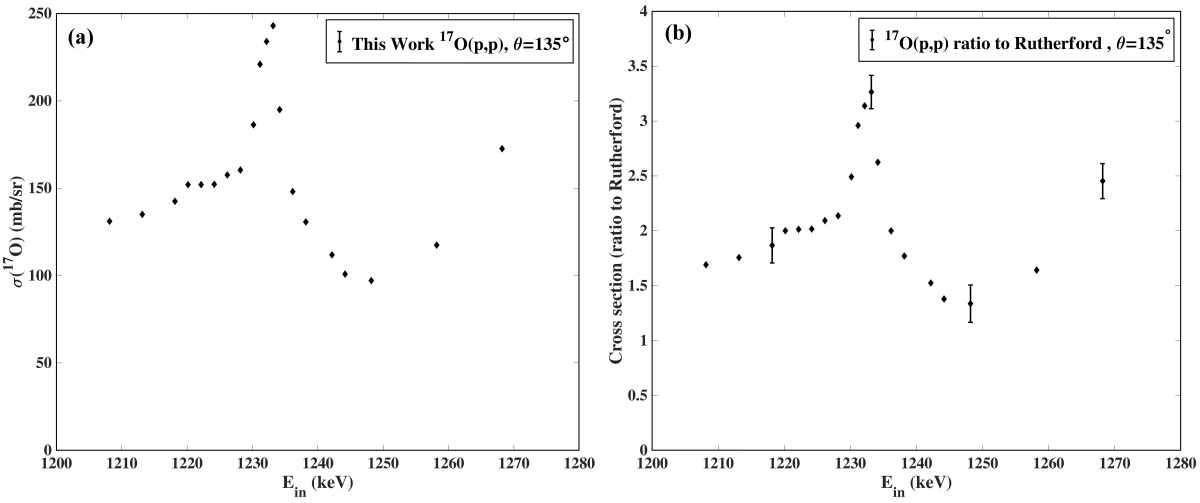

(a) (b)

Figure 5.11: a) Proton scattering cross-sections and b) the ratio to the Rutherford cross section of ^{17}O(p,p)^{17}O at 135° for E$_p$=1.2–1.3 MeV in the laboratory system.

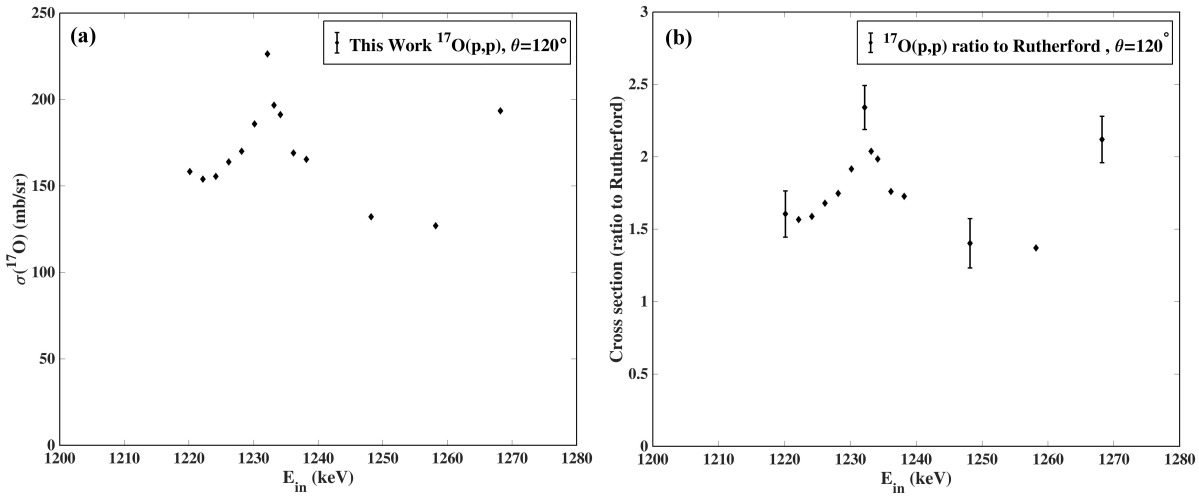

(a) (b)

Figure 5.12: a) Proton scattering cross-sections and b) the ratio to the Rutherford cross section of ^{17}O(p,p)^{17}O at 120° for E$_p$=1.2–1.3 MeV in the laboratory system.

Further experimental work will be required to resolve the difference in shape between this yield curve and our cross section measurement.

In view of possible depth profiling applications we measured the cross section of ^{17}O(p,p) in the vicinity of this resonance at back scattering angles of 150°, 135° and 120°, shown in Figure 5.10-5.12 respectively. From the comparison of the curves in Figure 4.13, it is clear that the highest backscattering angle of 165° is to be preferred for ^{17}O depth profiling by EBS with this resonance.

The elastic scattering of protons on ^{17}O could be modelled with conventional phenomenological R-matrix theory [124, 125], which could then provide a physical basis for the best estimates of cross sections for arbitrary energies and angles, however the R-matrix

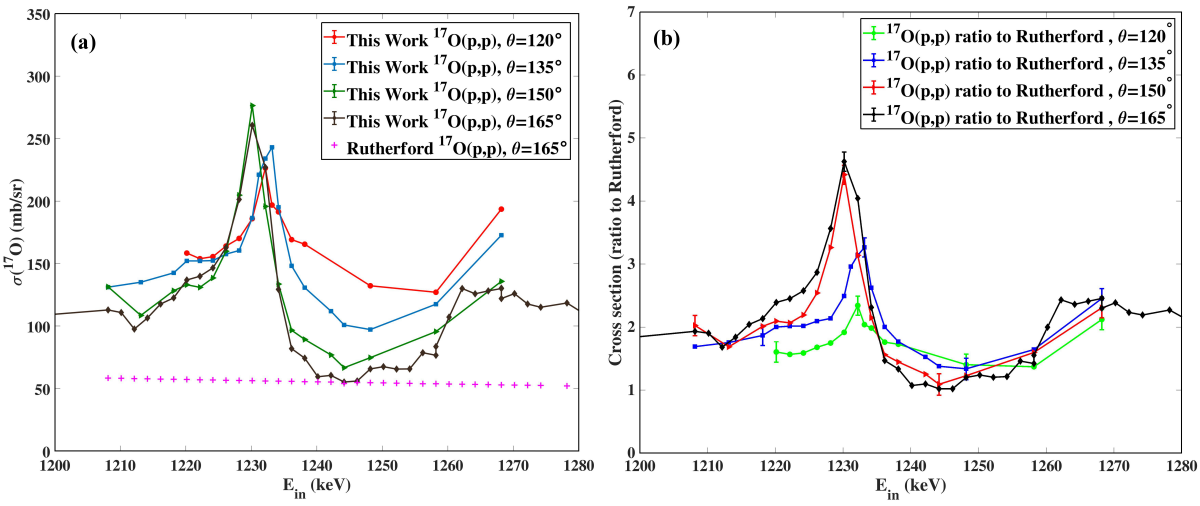

(a) (b)

Figure 5.13: Comparison of a) proton scattering cross-sections and b) the ratio to the Rutherford cross section of ^{17}O(p,p)^{17}O at different angles for E$_p$=1.2–1.3 MeV in the laboratory system.

parameters would be determined with more reliability if cross sections at a number of angles contributed to their determination. Further measurements are planned in view of establishing a reliable R-matrix formulation for the absolute value of the cross section over a range of backscattering angles.

5.4 Conclusions

The elastic backscattering (EBS) cross section for protons on ^{17}O was measured for the first time. For energies in the range 600 keV to 2 MeV, and a laboratory scattering angle of 165°, the cross section consists of a smoothly varying component increasing from 1.2 times the Rutherford cross section at 600 keV up to about 3 times the Rutherford cross section at 2 MeV, on which are superposed a number of resonance structures. Amongst these, the intense EBS resonance of 4.5 keV width with a peak at 1230 keV has the most potential for concentration depth profiling of ^{17}O by beam energy scanning, especially at high backscattering angles, and could provide a depth resolution of about 50nm in silicon.

Chapter 6

Conclusions and Suggestions

6.1 Al(d,p) and Al(d,α)

6.1.1 Conclusions

In chapter of this thesis, we measured the differential cross sections of ^{27}Al(d,p$_{0+1,2+3,4,5+6}$) ^{28}Al and ^{27}Al(d, $\alpha_{0,1,2,3,4}$)^{25}Mg reactions at VGDT (Tehran) using thin self-supporting aluminum targets for incident deuteron energies between 1.4 MeV and 2 MeV at 135°, 150°, and 165° angles of laboratory scattering. On the SAFIR platform at INSP, the independent measurements for 150° were repeated and agreed well with the VDGT data. Data from existing data sets were used to evaluate the cross sections at 150° and a Fourier series fit with 20 terms is proposed to represent the evaluated cross section. We have benchmarked the evaluated cross-sections using the thick target spectra of charged particles induced by deuteron beams from a pure aluminum target, in various detection angles at both VDGT and INSP. It would be reasonable to conclude that the overall agreement between the simulated spectra generated by SIMNRA and the measured benchmarking spectra is quite satisfying and that these evaluated cross sections are valid. The use of these evaluated cross sections is therefore recommended for the NRA. As noted, the recommended cross sections for 135° and 165° are the first ^{27}Al(d,p&α) cross sections that are benchmarked at these angles for NRA.

6.1.1.1 Exploiting the high-quality d-^{27}Al cross sections

The measurements and benchmarking of the ^{27}Al(d,p&α) cross sections are particularly robust. They have been completely repeated independently in two different laboratories; aluminium is a monoelemental target and has only a single stable isotope and is freely available in highly pure form. It is metallic, and resists radiation damage well, and since it is a conductor, there are fewer problems of current integration compared to insulating targets.

The benchmarking requires fitting NRA charged particle spectra obtained from thick targets. This is limited by knowledge of the stopping powers of the incident beam and the detected charged particles. It was remarkable to us that such good benchmarking was obtained, given that stopping powers are rarely known to better than 5% and in some cases much less well. The SIMNRA program used for the benchmarking offers several variations of semi-empirical stopping powers, and for certain ion/target combinations the differences can be significant, however for protons in Al the differences are minor. In Table 6.1, we list stopping powers from the two most modern options available in SIMNRA, which are from SRIM-97 and SRIM 2013. We see from the table that the values from SRIM2013 vary by a maximum of just under 2% from those defined 16 years earlier, for a proton energy of 500 keV and 1% or less for higher energies. In Figure 6.1, we reproduce from the SRIM website the comparison of the semiempirical proton stopping power curve with the measured data for aluminium. Note that the empirical stopping power for aluminium is determined not only from measurements on Al, but also from neighbouring elements. From the Figure, we see that for the energies of interest in this thesis, from 500 keV up, the spread of measured values around the semi-empirical fit is very small. Finally, we note that since aluminium is elemental there is no need to invoke Bragg's rule for compound stopping power. Deuteron stopping powers are simply scaled from proton stopping powers, and the situation is very similar for alpha-particle stopping powers in SRIM.

Table 6.1: list stopping powers from the two most modern options available in SIMNRA

protons			
Energy	Ziegler/Biersack (SRIM97)	SRIM2013	delta (%)
keV	eV/10^{15}at.cm^{-2}		%
100	20.4	20.2	0.99
200	16.8	16.7	0.60
500	11.4	11.2	1.79
1000	7.75	7.84	-1.15
1500	5.99	6.03	-0.66
2000	4.94	4.96	-0.40

This very robust measurement of the ^{27}Al(d,p&α) cross sections incites their use as a basis for other cross section measurements. For example using a thin AlN target, which can be grown with good stoichiometry by Molecular Beam Epitaxy on a GaAs substrate,

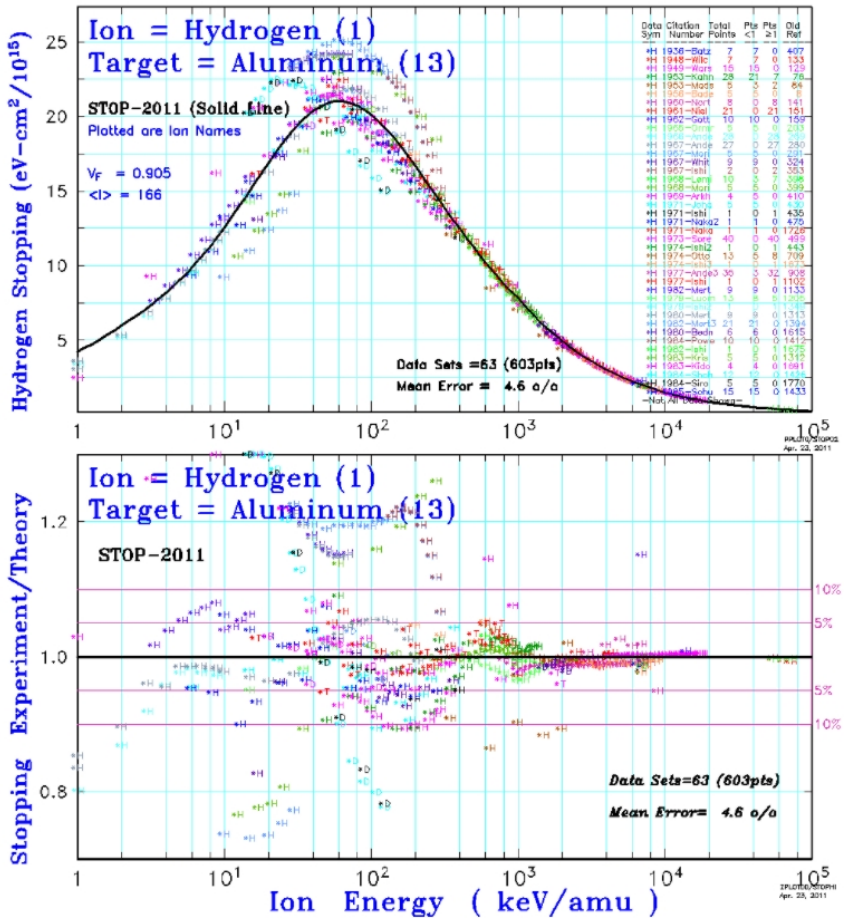

Figure 6.1: The comparison of the semiempirical proton stopping power curve with the measured data for aluminium [19]

would allow direct calibration of deuteron-induced reactions on ^{14}N against one of the ^{27}Al(d,p&α) reactions, and the d-^{14}N reaction measurements could then be completed on a heavier nitride such as GaN or InN where there would be no interferences from the d-^{27}Al reactions.

6.1.2 Future work and paper: Benchmarked ^{27}Al(d,d)^{27}Al differential cross sections

We also measured the ^{27}Al(d,d)^{27}Al differential cross sections for incident deuteron energies between 1.4 and 2 MeV at $\theta_{lab} = 135°$, 150°, and 165° at VGDT and at 150° at INSP lab for the first time. These measurements, which have not been benchmarked, are not presented here. They will be published in a future paper after further interpretation and benchmarking.

6.1.3 Perspective Obtaining cross sections from thick targets

For the d-^{27}Al benchmarking experiment, we needed the cross section value for ^{27}Al(d,p_{0+1}) at lower energies than those for which it was measured, since the low energy tail from this group, derived from deuterons that had penetrated deeply into the sample, in some cases overlapped with the high energy part of the ^{27}Al(d,p_2) group originating in the surface of the sample. We resolved this problem by artificially extending the ^{27}Al(d,p_{0+1}) to lower energies by hand, in such a way as to best fit the measured spectrum.

This raises the obvious idea of simply deducing the cross sections from measurements of charged particle spectra obtained by bombarding a thick target at the highest energy and iteratively fitting adjusted cross sections until satisfactory agreement is obtained with the measured spectrum, rather than painstakingly measuring the cross sections at many energies with a thin target. However, the limited energy resolution (at best, 10 keV) of the charged particle detector, and the energy straggling of the incident beam as it penetrates the target would limit the resolution with which the cross section could be deduced.

A series of spectra taken at a series of incident particle energies could then be envisaged, so that at least the effects of energy straggling could be to some extent mitigated, at the expense of a heavy effort to simultaneously fit multiple spectra. Indeed, we already performed the benchmarking at 4 widely spaced energies so as to test the validity of the cross sections with reasonable energy resolution across the full range of the measurement. This approach would still not circumvent the limited energy resolution of the detectors though.

At the expense of an even heavier effort to fit a large number of spectra simultaneously, thick target spectra could be taken at energy steps even smaller than the detector resolution – even the same energy steps as used for the thin target measurements. The fine details of the cross section would then be embodied in the variations of the shape of the cross section with the incident beam energy. This is illustrated hypothetically in Figure 6.2, where SIMNRA was used to calculate a series of ^{16}O EBS spectra obtained for small increments in incident beam energy near the 10 keV wide resonance near 3.045 MeV in ^{16}O(α,α)^{16}O, from a pure oxygen target. A detector resolution of 15 keV was used, and it is clear that the effects of cross section details at a rather finer detail than 15 keV are easily visible in the shape of the spectrum.

Modern computing tools and artificial intelligence approaches to treating large data sets would now make the simultaneous fitting of hundreds or even thousands of spectra feasible, and the resulting deduced cross sections should be defined even better than those measured with thin targets because each of the many spectra contains information about the cross sections for all energies below the incident particle energy.

Because aluminium is such a favourable target, as outlined above, and because we already have the cross sections measured with thin targets, the d-^{27}Al cross sections

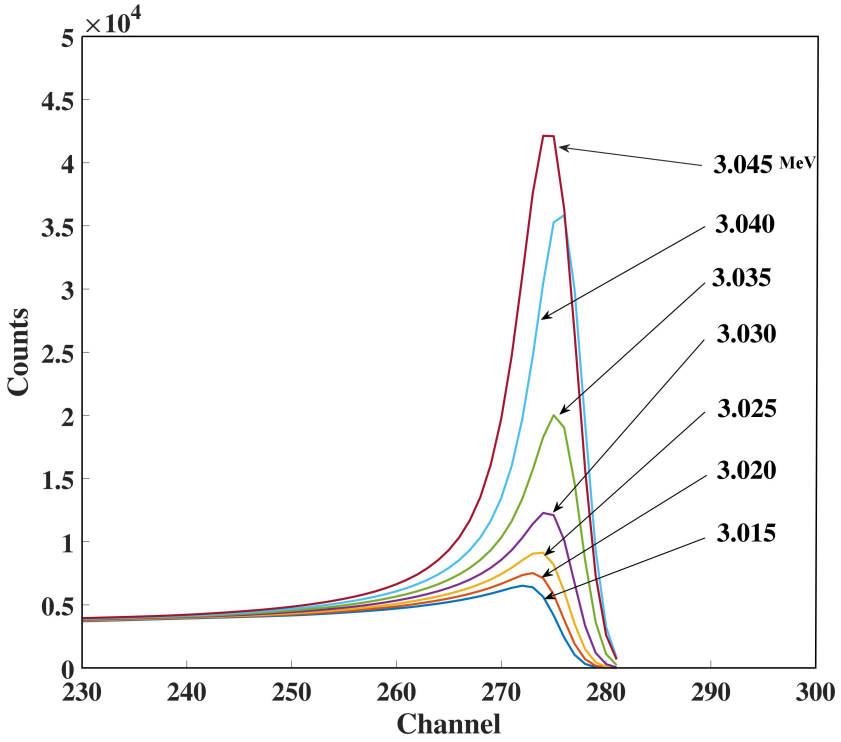

Figure 6.2: ^{16}O(α,α) Obtained spectra from a pure Oxygen target for beam energies in the vicinity of the 10 keV wide resonance near 3.045 MeV by using SIMNRA calculation

obtained from thick target spectra on pure aluminium would be an ideal test case for the multiple thick target spectra approach suggested here.

6.2 ^{17}O(p,p)

6.2.1 Conclusions

First measurements of the EBS for protons on ^{17}O were performed in the chapter of this thesis. For a laboratory scattering angle of 165°, and in the range of energies 600keV- 2 MeV, the cross section consists of a smooth varying component that increases from 1.2 times the Rutherford cross section at 600 keV up to about 3 times the Rutherford cross section at 2 MeV, over which a few resonance structures are superposed. Amongst these EBS resonances, the intense one with a peak at 1230 keV and a width of 4.5 keV could be used for concentration depth profiling of ^{17}O via beam energy scanning, specifically at high backscattering angles, and could provide a depth resolution of about 50nm in silicon.

6.2.2 Future work and papers

Our attempts to make a thin $^{27}Al_2^{17}O_3$ film by oxidising either the thin self-supporting Al films that were produced for the d-^{27}Al measurements, or a thin ^{27}Al layer on a heavy substrate, were not successful, but it would be well worth pursuing this since a thin self-

supporting ^{17}O film or such a thin film on a heavy substrate would allow careful direct cross-comparison of measured $^{17}O(d,p\&\alpha)$ cross sections with those of $^{27}Al(d,p\&\alpha)$.

We have found no reports of measurements of the cross sections of the $^{17}O(d,\alpha)^{15}N$ and $^{17}O(d,p)^{18}F$ nuclear reactions in the literature. These two reactions have high positive Q-values which leads to high energy alpha particles and protons which should be easily distinguishable in the energy spectrum of all particles emitted from a compound target under deuterium irradiation. Isotopically pure $^{nat}Si^{17}O_2$ targets were produced by dry thermal oxidation of silicon in pure $^{17}O_2$ at INSP. Initial experiments for the d-^{17}O cross sections have been performed, and we were able to observe a number of proton and alpha particle peaks from the d-^{17}O reactions, however interference from d-Si reactions in the thick ^{28}Si substrate made detailed quantitative interpretation of the spectra too uncertain to enable us to be able to propose well-characterised cross sections, and so they are not presented in this thesis.

6.2.3 Perspective

The $^{17}O(p,p)^{17}O$ cross section measured in this thesis will already open the way to three-way stable isotopic tracing experiments for the determination of thin oxide film growth mechanisms, and if applied in conjunction with the d-^{17}O reactions, could provide a powerful analytical suite for ^{17}O tracing studies The use of ^{18}O as a stable isotopic tracer for such studies, in conjunction with ^{18}O specific NRA on SAFIR, has been developed at INSP for many years, and is also available in the new Atomic Layer Deposition (ALD) system developed by the team responsible for SAFIR. Isotopically distinct nanolaminates of Alumina could be grown (for example 10nm $Al_2^{16}O_3$/10nm $Al_2^{18}O_3$) and annealed in $^{17}O_2$. Determining the amounts of each isotope incorporated or lost during the annealing process as a function of O_2 partial pressure, anneal temperature and time will allow determination of diffusion coefficients and thermodynamic properties such as activation energies that can be compared with models of the transport and exchange of oxygen during thermal annealing and used to guide the ALD growth parameters to obtain the most compact and compositionally stable alumina films. With the available ALD precursors similar studies could be envisaged for the growth of HfO_2, TiO_2 and ZnO thin films or nanolaminates.

PART II : FRENCH VERSION:
Résumé

Chapter 7

French Summary: Résumé

7.1 Introduction

L'IBA (Ion Beam Analysis) a été largement utilisée pour analyser quantitativement et avec une grande sensibilité la composition et les profils de profondeur des éléments dans les régions superficielles des solides. Pour l'analyse des éléments légers, on peut trouver des réactions nucléaires appropriées et, en particulier, les réactions induites par les deutérons, (d,p) ou (d,α), ont souvent des chaleurs de réaction Q élevées et des sections efficaces appréciables. Dans de nombreux cas de NRA (Nuclear Reaction Analysis) de films minces, des pics isolés de particules de réaction peuvent être obtenus avec un choix judicieux de l'angle de diffusion, de l'énergie du faisceau incident et des feuilles de filtrage devant le détecteur de particules chargées. Cependant, en général, la NRA génère des spectres complexes avec des pics qui se chevauchent, en particulier pour les échantillons épais.

La connaissance des sections efficaces pour les cas de pics isolés est déjà utile pour concevoir des expériences visant à déterminer les contenus élémentaires des films minces. De nombreuses sections efficaces de ce type, par exemple ^{16}O(d,p$_0$)^{17}O, ^{16}O(d,p$_1$)^{17}O, ^{12}C(d,p$_0$), ^{14}N(d,α_0), ont été soigneusement mesurées dans des gammes d'énergie et d'angle d'intérêt analytique [87–90]. Il est parfois possible d'analyser plusieurs éléments légers simultanément par NRA. La connaissance des sections efficaces des réactions qui ne sont pas nécessairement d'un intérêt primordial pour l'analyse des couches minces, est alors souvent nécessaire pour les cas où les cibles contiennent des éléments donnant lieu à des réactions produisant des groupes de particules qui interfèrent avec le pic analytique primaire, et encore plus dans le cas de la NRA sur cible épaisse où l'élargissement des spectres de particules dû à l'épaisseur non nulle de la cible entraîne une probabilité beaucoup plus grande d'interférences élémentaires [26, 38, 91].

La nécessité de disposer de sections efficaces précises, même lorsqu'elles ne présentent pas un intérêt primordial pour un problème analytique spécifique, ou dans des gammes d'énergie qui ne sont pas directement utiles sur le plan analytique, s'est également ac-

centuée récemment, avec l'introduction du concept d'IBA totale [92–94], dans lequel toutes les informations des spectres IBA [95] sont exploitées, et l'utilisation croissante de l'intellig-ence artificielle et des approches d'apprentissage automatique pour optimiser l'extraction d'informations de toutes les parties des spectres IBA. Jusqu'à présent, les réseaux neuronaux artificiels (ANN) ont été appliqués au cas de la spectrométrie de rétrodiffusion de Rutherford, où les sections efficaces sont connues analytiquement, mais l'extension fiable de ces techniques avancées de traitement des données à la NRA nécessite les meilleures sections efficaces de réaction nucléaire possibles. En outre, des sections efficaces de réaction nucléaire expérimentale précises sont nécessaires pour fournir des paramètres appropriés pour les approximations et les expressions appropriées des modèles théoriques de mécanismes de réaction nucléaire.

L'oxygène étant l'élément le plus abondant de la croûte terrestre et en raison de l'importance universelle des oxydes dans les sciences de la terre et des matériaux, des sections efficaces précises pour les réactions nucléaires sur ^{16}O et ^{18}O ont déjà été déterminées [87, 96]. Le deuxième élément le plus abondant est le silicium, et bien qu'il s'agisse d'un élément de masse intermédiaire du point de vue de l'IBA, il y a également des réactions nucléaires d'intérêt analytique qui ont été déterminées [88, 97].

L'aluminium, troisième élément le plus abondant, est largement utilisé dans l'industrie pour ses propriétés mécaniques et électriques, ses applications décoratives et sa résistance aux agressions environnementales, notamment après une passivation électrochimique appropriée. L'aluminium est également largement présent dans les roches d'alumino-silicate qui constituent une grande partie de la croûte terrestre supérieure. Dans de nombreux systèmes à couche mince, tels que les semi-conducteurs III-azote développés entre autres pour les diodes électroluminescentes UV-C destinées à remplacer les lampes UV au mercure dans les applications de stérilisation de masse pour l'atténuation du COVID, et les films ou nanolaminés minces d'alumine conforme obtenus par dépôt de couche atomique où l'aluminium est un composant essentiel, la détermination absolue de la teneur en Al est primordiale pour développer des matériaux améliorés. Il existe une multitude de réactions de particules chargées induites par les deutons sur ^{27}Al avec des valeurs Q élevées, qui peuvent être exploitées dans la NRA pour l'analyse de l'aluminium ou rencontrées comme interférences dans la NRA des matériaux contenant de l'aluminium [98–109].

La connaissance détaillée des sections efficaces de ces réactions constitue donc un intérêt important dans le domaine de la NRA aussi bien pour leur exploitation en analyse de l'aluminium, que pour la prise en compte quantitative de leurs interférences pour l'analyse d'autres éléments légers dans des matériaux contenant de l'aluminium [99–104].

Le premier objectif de la thèse est de mesurer avec précision sur le VDGT (accélérateur Van de Graaff à Téhéran) en Iran les sections efficaces des réactions nucléaires induites par les deutérons sur ^{27}Al, pour lesquelles les mesures de la littérature présentent des différences importantes. Il est remarquablement difficile de mesurer avec précision les

sections efficaces - il faut des cibles de différentes épaisseurs, dont la composition est connue à environ 1% près, ainsi qu'un calibrage très précis de l'énergie de l'accélérateur et un haut degré de maîtrise de l'électronique de détection. En plus d'un mauvais étalonnage de l'énergie de l'accélérateur et de cibles insuffisamment bien caractérisées, des effets tels que le temps mort électronique non contrôlé, la dégradation de la cible sous le faisceau et les fluctuations du courant du faisceau incident, entre autres, sont probablement à l'origine de la variabilité des sections efficace publiées précédemment. Les mesures de section efficace de l'aluminium ont été répétées à l'INSP (Institut de Nanoscience) de Paris. C'est la première fois que de telles sections efficaces ont été mesurées dans un seul projet sur deux systèmes indépendants.

En plus de ce travail métrologique minutieux, la thèse a permis de déterminer pour la première fois les sections efficaces des réactions $^{17}O(p,p)^{17}O$, pour lesquelles il n'existe pas de données bibliographiques. Les cibles $^{nat}Si^{17}O_2$ isotopiquement pures ont été produites par oxydation thermique sèche du silicium dans du $^{17}O_2$ pur à l'INSP, qui dispose du gaz isotopiquement pur et des installations de four dédiées à la manipulation de ce gaz coûteux. Toutes les sections efficaces mesurées sont incorporées dans la base de données IBANDL [1] hébergée et maintenue par l'Agence Internationale de l'Energie Atomique à Vienne.

7.2 Mesurés

7.2.1 Préparation des échantillons

La préparation correcte de la cible est l'un des aspects les plus importants pour réaliser des expériences de physique nucléaire précises pour IBA et mesurer les sections efficaces. Dans cette thèse, des couches d'aluminium autoportées très minces peuvent être préparées par évaporation sous vide [69,70]. Nous avons également appliqué l'évaporation sous vide pour le dépôt de films minces d'Au et d'Ag, et l'oxydation thermique pour la préparation de films de $Si^{17}O_2$ sur du silicium.

7.2.1.1 ^{27}Al

La cible mince en Al doit avoir une épaisseur appropriée, être stable à la fois dans l'atmosphère et sous le faisceau dans le vide et doit également être amorphe pour éviter les effets de canalisation indésirables [71]. Pour répondre à ces exigences, le dépôt physique en phase vapeur (PVD) a été choisi parmi les différentes méthodes de préparation de cibles minces en aluminium [64]. L'aluminium pur a été évaporé sur une lame de microscope préalablement préparée par immersion dans un mélange d'eau et de détergent sous agitation ultrasonique. Le système PVD était un modèle VE-770 avec une pression de base d'environ 10-6 mbar, équipé d'un filament de tungstène enroulé. Le film obtenu a été

mis à flotter sur l'eau, puis repêché sur un trou de 8 mm de diamètre dans une fine feuille de métal. Enfin, 10 ± 0.5 nm d'Ag ont été déposés sur le mince film d'Al autoportant évaporé sous vide comme référence interne [57, 58].

7.2.1.2 ^{17}O

Idéalement, il faudrait utiliser pour ces mesures des échantillons de gaz [124], ou des échantillons minces autoportants tels que ceux préparés par oxydation anodique par Amsel pour les mesures approfondies de sections efficaces des réactions nucléaires ^{16}O et ^{18}O [129] Cependant nous ne disposons ni d'une réserve d'eau hautement enrichie en ^{17}O pour l'oxydation anodique, ni d'une chambre à cible gazeuse et d'un système de détection. Bien qu'il ait été démontré qu'il était possible de fabriquer des cibles minces autoportantes [125], nos tentatives (par exemple en oxydant l'aluminium [2]) ont également échoué, et nous avons donc utilisé des couches de silice thermique d'une épaisseur proche de 100 nm, formées sur des plaquettes de silicium orientées ¡100¿ par oxydation thermique à 1100 °C dans du $^{17}O_2$ gazeux dans un four à vide en quartz, ayant une pression de base de 10-6 mbar. Le choix d'un substrat de silicium présente l'avantage que les méthodes d'oxydation thermique et les caractéristiques de l'oxyde sont très bien connues [80], L'inconvénient de cette cible est que les protons sont rétrodiffusés élastiquement par les atomes d'oxygène de la fine couche de surface d'oxyde avec une énergie inférieure à celle des protons rétrodiffusés par le silicium, et donc le pic ^{17}O correspondant dans le spectre se trouve sur un fond important et non Rutherford de protons diffusés par le Si. Cela complique l'extraction de la surface du pic. Les oxydes ^{17}O thermiques pourraient être fabriqués sur des substrats plus lourds où le signal du substrat serait au moins Rutherford, mais bien sûr, dans ce cas, l'amplitude du signal du substrat écraserait le signal de diffusion élastique du ^{17}O.

L'oxyde thermique de silicium, formé à 1100°C dans de l'oxygène pur, devrait être très proche de la stœchiométrie [80]. Nous avons mesuré l'épaisseur physique de la silice et son indice de réfraction par ellipsométrie. La densité surfacique de ^{18}O[N_{18_O}] a été déterminée par NRA avec la réaction ^{18}O(p,α)^{15}N [128], qui a une valeur Q élevée de 3.97 MeV, fournissant un pic isolé. La densité surfacique de ^{16}O] a été déterminée par NRA avec la réaction ^{16}O(d, p_1)^{17}O [78, 118] avec un faisceau de deutons de 860 keV.

7.2.2 Etalonnage en énergie de l'accélérateur

7.2.2.1 Au laboratoire VDGT à Téhéran (Iran)

Nous avons déterminé l'énergie du faisceau à partir de l'intensité du champ de l'aimant d'analyse, mesurée avec un fluxmètre NMR [39]. L'étalonnage en énergie de l'accélérateur a été déterminé à partir de l'énergie du seuil dans la réaction ^{7}Li(p,n)^{7}Be à 1880.44 ± 0.02 keV. La cible était une pastille de poudre de LiF comprimée recouvert d'un revêtement

d'argent de 10 $\mu g/cm^2$ pour l'évacuation des charges. Les neutrons ont été détectés avec un détecteur BF3.

7.2.2.2 Au laboratoire de l'INSP à Paris (France)

L'énergie de l'accélérateur, lue à partir du signal du voltmètre rotatif, a été étalonnée en utilisant les résonances nucléaires étroites de la réaction ^{13}C(p,γ)^{14}N à 1747.6 keV, de la réaction ^{27}Al(p,γ)^{28}Si à 991.88 keV, et de la réaction ^{15}N(p,$\alpha\gamma$)^{12}C à 426.1 keV. Dans chaque cas, les rayons gamma ont été détectés avec un détecteur à scintillation BGO à 0° [59,60]. En raison de la très haute résolution en énergie du faisceau - moins de 250eV de largeur totale à mi-hauteur d'énergie sur la gamme rapportée ici, les courbes d'excitation ont été ajustées avec SPACES [61] afin de compenser les petites distorsions de la courbe d'excitation dues aux contaminants de surface et à l'oxydation. Notons que traitement du signal brut sortie du GVM a été implémenté numériquement dans Labview plutôt que dans des circuits électroniques analogiques, ce qui donne un étalonnage en énergie qui est hautement linéaire et pratiquement indépendant de la température.

7.3 Résultats

Les sections efficaces mesurées dans cette thèse ont été publiées dans deux articles, une concernant ^{27}Al(d,p&α) reproduite dans le chapitre 4, et pour la diffusion élastique des protons ^{17}O(p,p)^{17}O dans la chapitre 5. Nous décrivons brièvement ci-dessous ces mesures.

7.3.0.1 Ajustements de Fourier pour ^{27}Al

Les sections efficaces ont été mesurées à 165° (VDGT), 150° (VDGT et SAFIR) et 135° (VDGT) pour des deutons entre 1.4 et 2.0 MeV, et sont présentées dans les Figures 4.10 – 4.13. Comme il n'existe pas de modèle de réaction nucléaire approprié pour ces réactions, la question se pose de savoir comment représenter les meilleures valeurs moyennes des données pour proposer une section efficace unique recommandée à n'importe quelle énergie dans la gamme mesurée. Nous avons adopté l'approche consistant à ajuster une fonction mathématique librement choisie à toutes les données, pondérées inversement en fonction de leurs incertitudes déclarées.

Nos données, ainsi que certaines sélectionnées de la littérature ont donc été ajustés avec des séries de Fourier à 8 et 20 termes, ainsi qu'avec un algorithme d'interpolation spline, illustré dans la Figure 4.12, par le langage de programmation MATLAB.

Les différences entre les fonctions ajustées sont faibles, mais la série de Fourier à 20 termes permet de représenter les données avec une bonne fidélité et sans trop de paramètres ajustés.

7.3.1 Benchmarking pour ^{27}Al

La justesse des sections efficaces est testée, dans un processus appelé 'benchmarking' en anglais, par leur utilisation pour la reproduction de la forme des spectres des particules chargées obtenu par irradiation d'une cible épaisse d'aluminium pur, recouverte d'une fine couche d'Ag/Au pour le processus d'auto-normalisation. Des spectres ont été obtenus pour des deutérons d'énergie incidente Ed=1600-1900keV par intervalle de 100keV, pour des angles de diffusion 135°, 150° et 165°. Pour la partie simulation du benchmarking, le code SIMNRA 7.03 est appliqué avec le modèle de straggling de Chu et Yang et le pouvoir d'arrêt de Ziegler/Biersack.

Nous avons benchmarké les sections efficaces ^{27}Al(d,p)^{28}Al et ^{27}Al(d,α)^{25}Mg à trois angles de diffusion, 135°, 150° et 165°, dans deux laboratoires différents. À 150°, les trois ensembles de données de section efficace (données VDGT, données INSP et données ajustées) ont été incorporés dans la bibliothèque SIMNRA. Globalement, l'accord entre les spectres simulés et mesurés est très satisfaisant.

La gamme des sections efficace mesurées utilisées pour la simulation des spectres était de 1.4-2 MeV. Après la perte d'énergie dans la cible Al, chaque fois que Ed,Lab tombe en dessous de l'énergie minimale de la section efficace mesurée (1.4 MeV), la simulation correspondante des section efficace mesurées n'a pas de valeur et SIMNRA considère sa valeur égale à zéro. Dans ce cas, pour la réaction ^{27}Al(d,p$_{0+1}$), nous avons inséré manuellement des valeurs de sections efficaces très espacées pour des énergies inférieures à 1.4 MeV, de sorte que les spectres mesurés de la cible épaisse dans la gamme d'énergie de 4700-5000 keV soient reproduits par les simulations. Des inclusions similaires ont été faites pour les sections efficaces du ^{27}Al(d,p$_{2+3,p4,p5+6}$) dans les plages d'énergie pertinentes. Ces valeurs de section efficace sont certainement de la bonne amplitude, mais en raison de la dispersion de l'énergie du faisceau incident à ces profondeurs dans la cible, dans cette gamme d'énergie, la section efficace proposée ne représenterait fidèlement aucune structure fine. Afin de différencier les sections efficaces mesurées par les cibles minces et incarnées par la série de Fourier N=20, des valeurs déduites des expériences de référence, les deux ensembles de données sont chargés séparément dans IBANDL [1].

7.3.2 Résultat de la mesure de ^{17}O(p,p)

La section efficace de diffusion des protons pour ^{17}O à 165° pour E$_p$=0.6-2 MeV dans le système de laboratoire est présentée dans la Figure 5.9a, le rapport avec la section efficace de Rutherford étant présenté à la Figure 5.9b. Les valeurs d'énergie tiennent compte de la perte d'énergie finie dans la couche de silice, qui varie de 5.8 keV pour une énergie incidente de 600 keV, à 2.7 keV pour des protons incidents de 2 MeV. L'incertitude systématique est de 14% (1σ) selon les formules de propagation d'erreur standard, y compris l'incertitude dans les mesures de la teneur des différents isotopes de l'oxygène, et du produit $\Omega \times Q$.

L'incertitude sur la détermination de la surface du pic d'oxygène, estimée par traitement de Monte Carlo de la méthode d'extraction de la surface du pic (c'est-à-dire incluant la variation de la performance de l'opérateur), est majoritairement comprise entre 4% et 6% et varie de 3% à environ 8% selon l'intensité du pic et la taille et la forme du fond à estimer. La plus grande incertitude de 8% a été obtenue pour le spectre de la Figure 5.7d.

Il existe une résonance intense avec une intensité maximale à 1230 keV, de largeur d'environ 4.5keV après soustraction en quadrature de la largeur de l'énergie de la cible d'environ 4 keV. Nous avons également superposé les courbes de rendement à l'échelle pour de [124] et de [125]. Les énergies de résonance sont en bon accord avec nos mesures si l'échelle d'énergie de [124] est ajustée par un facteur de 0.99. En revanche, la forme de la courbe de rendement de [124] est sensiblement différente de notre mesure. Nous proposons que la contamination en ^{18}O du gaz utilisé comme cible dans [124], pas pris en compte par les auteurs, est à l'origine de cette différence. Nous notons également que l'intensité de la résonance dans la courbe de rendement [124], comparée à la composante continue, est plus faible que celle de la section efficace que nous avons mesuré. Cependant la largeur de cette résonance dans la courbe de rendement est très proche de la largeur de 4.5 keV que nous avons observée dans la section efficace. Cette largeur donnerait une résolution en profondeur d'environ 50nm dans le Si lorsque l'énergie du faisceau est balayée autour de l'énergie de résonance.

La courbe de rendement de [125] a été mesurée par le même groupe que celle de [124], en utilisant une cible mince autoportante à partir de laquelle les protons diffusés par ^{16}O et ^{18}O peuvent être séparés de ceux diffusés par ^{17}O. Cette courbe de rendement, correctement mise à l'échelle, devrait alors représenter la section efficace de diffusion. Il y a une nette divergence entre cette courbe de rendement mise à l'échelle et notre mesure en dessous d'environ 1.8 MeV. Nous ne pouvons pas expliquer cette divergence, mais nous notons que la section efficace mesurée est robuste contre les erreurs systématiques ou les biais possibles dans la tâche délicate de la soustraction du fond, pour laquelle la réduction des données par deux analystes indépendants donne des résultats dans les marges d'incertitude aléatoires estimées. D'autres travaux expérimentaux seront nécessaires pour résoudre la différence de forme entre cette courbe de rendement et notre mesure de section efficace.

En vue d'éventuelles applications de profilage en profondeur, nous avons mesuré la section efficace du ^{17}O(p,p) au voisinage de cette résonance à des angles de rétrodiffusion de 150^{o}, 135^{o} et 120^{o}, présentés respectivement sur les Figure 5.10-Figure 5.12. D'après la comparaison des courbes de la Figure 5.13, il est clair que l'angle de rétrodiffusion le plus élevé, 165°, est à privilégier pour le profilage en profondeur du ^{17}O par EBS avec cette résonance.

7.4 Conclusions et travaux futurs

7.4.1 Al(d,p) et Al(d,α)

7.4.1.1 Conclusions sur l'Al

Dans le chapitre de cette thèse, nous avons mesuré les sections efficaces différentielles des réactions ^{27}Al(d,p$_{0+1,2+3,4,5+6}$)^{28}Al et ^{27}Al(d, $\alpha_{0,1,2,3,4}$)^{25}Mg au VGDT (Téhéran) en utilisant des cibles minces autoportantes en aluminium pour des énergies incidentes de deutons comprises entre 1.4 et 2 MeV à des angles de 135°, 150° et 165° de la diffusion de laboratoire. Sur la plateforme SAFIR de l'INSP, les mesures indépendantes pour 150° ont été répétées et ont bien concordé avec les données du VDGT. Des données provenant d'ensembles de données existants ont été utilisées pour évaluer les sections efficaces à 150° et un ajustement de série de Fourier à 20 termes est proposé pour représenter la section efficace évaluée. Nous avons comparé les sections efficaces évaluées à l'aide des spectres de cibles épaisses de particules chargées induites par des faisceaux de deutons provenant d'une cible en aluminium pur, dans différents angles de détection au VDGT et à l'INSP. Il serait raisonnable de conclure que l'accord global entre les spectres simulés générés par SIMNRA et les spectres de référence mesurés est tout à fait satisfaisant et que ces sections efficaces évaluées sont valides. L'utilisation de ces section efficace évaluées est donc recommandée pour la NRA. Par ailleurs, les sections croisées recommandées pour 135° et 165° sont les premières sections croisées de ^{27}Al(d,p&α) qui sont étalonnées à ces angles pour le NRA.

7.4.1.2 Exploitation des section efficace d-^{27}Al de haute qualité

Les mesures et l'étalonnage des sections croisées de ^{27}Al(d,p&α) sont particulièrement robustes. Elles ont été entièrement répétées indépendamment dans deux laboratoires différents. L'aluminium est une cible monoélémentaire, il ne possède qu'un seul isotope stable et il est disponible facilement sous une forme très pure. Il est métallique et résiste bien aux dégâts causés par les rayonnements. Comme c'est un conducteur, il y a moins de problèmes d'intégration du courant par rapport aux cibles isolantes.

L'évaluation comparative nécessite l'ajustement des spectres de particules chargées de l'ANR obtenus à partir de cibles épaisses. Cette opération est limitée par la connaissance des pouvoirs d'arrêt du faisceau incident et des particules chargées détectées. Il nous a semblé remarquable d'obtenir un si bon accord entre nos spectres et les simulation issuées de SIMNRA, étant donné que les pouvoirs d'arrêt sont rarement connus à plus de 5% et dans certains cas, beaucoup moins bien. Le programme SIMNRA utilisé pour l'analyse comparative offre plusieurs options de pouvoirs d'arrêt semi-empiriques, et pour certaines combinaisons ion/cible, les différences peuvent être importantes, mais pour les protons

dans Al, les différences sont mineures. Dans le Table 6.1, nous donnons les pouvoirs d'arrêt des deux options les plus modernes disponibles dans SIMNRA, qui sont celles de SRIM-97 et de SRIM 2013. Nous voyons dans le tableau que les valeurs de SRIM2013 varient au maximum d'un peu moins de 2% par rapport à celles définies 16 ans plus tôt, pour une énergie de proton de 500 keV et de 1% ou moins pour des énergies plus élevées. Dans la Figure 6.1, nous reproduisons à partir du site Web du SRIM la comparaison de la courbe semi-empirique du pouvoir d'arrêt des protons avec les données mesurées pour l'aluminium. Notons que le pouvoir d'arrêt empirique pour l'aluminium est déterminé non seulement à partir des mesures sur l'Al, mais aussi sur les éléments voisins. Sur la figure, nous voyons que pour les énergies qui nous intéressent dans cette thèse, à partir de 500 keV, l'écart des valeurs mesurées autour de l'ajustement semi-empirique est très faible. Enfin, nous notons que puisque l'aluminium est élémentaire, il n'est pas nécessaire d'invoquer la règle de Bragg pour le pouvoir d'arrêt des composés. Les pouvoirs d'arrêt du deutéron sont simplement mis à l'échelle à partir des pouvoirs d'arrêt du proton, et la situation est très similaire pour les pouvoirs d'arrêt des particules alpha dans SRIM.

Cette mesure très robuste des sections efficaces de ^{27}Al(d,p&α) incite à les utiliser comme base pour d'autres mesures de sections efficaces. Par exemple, l'utilisation d'une cible mince d'AlN, qui peut être élaborée avec une bonne stœchiométrie par épitaxie par faisceaux moléculaires sur un substrat de GaAs, permettrait de calibrer directement les réactions induites par les deutérons sur le ^{14}N par rapport à l'une des réactions de ^{27}Al(d,p&α), et les mesures de la réaction d-^{14}N pourraient alors être complétées sur un nitrure plus lourd comme le GaN ou l'InN, où il n'y aurait pas d'interférences des réactions d-^{27}Al.

7.4.1.3 Travaux futures et article

Nous avons également mesuré pour la première fois les sections efficaces différentielles ^{27}Al(d,d)^{27}Al pour des énergies incidentes de deutron comprises entre 1.4 et 2 MeV à θ_{lab} = 135°, 150° et 165° au VGDT et à 150° au laboratoire INSP. Ces mesures, qui n'ont pas été étalonnées, ne sont pas présentées ici. Elles seront publiées dans un prochain article après une interprétation et un étalonnage plus poussé.

7.4.1.4 Perspective : Obtention de section efficace à partir de cibles épaisses

Pour l'expérience de référence d-^{27}Al, nous avions besoin de la valeur de la section efficace de ^{27}Al(d,p$_{0+1}$) à des énergies inférieures à celles pour lesquelles elle a été mesurée, car la queue à basse énergie de ce groupe, dérivée des deutérons qui ont pénétré profondément dans l'échantillon, chevauche dans certains cas la partie à haute énergie du groupe ^{27}Al(d,p$_2$) provenant de la surface de l'échantillon. Nous avons résolu ce problème en étendant artificiellement à la main le groupe ^{27}Al(d,p$_{0+1}$) à des énergies plus basses,

de manière à ajuster au mieux le spectre mesuré.

Cela soulève l'idée évidente de déduire simplement les sections efficaces des mesures des spectres de particules chargées obtenues en bombardant une cible épaisse à l'énergie la plus élevée et en ajustant itérativement les sections efficaces ajustées jusqu'à ce qu'un accord satisfaisant soit obtenu avec le spectre mesuré, plutôt que de mesurer minutieusement les section efficace à de nombreuses énergies avec une cible mince. Cependant, la résolution énergétique limitée (au mieux, 10 keV) du détecteur de particules chargées, et l'élargissement de la distribution en énergie du faisceau incident lorsqu'il pénètre dans la cible, limiteraient la résolution avec laquelle la section efficace pourrait être déduite.

Une série de spectres pris à une série d'énergies de particules incidentes pourrait alors être envisagée, de sorte qu'au moins les effets de la dispersion des énergies pourraient être atténués dans une certaine mesure, au prix d'un plus lourd effort pour ajuster simultanément plusieurs spectres. En effet, nous avons déjà effectué le benchmarking à 4 énergies très espacées afin de tester la validité des sections efficaces avec une résolution en énergie raisonnable sur toute la gamme de mesures. Cette approche ne permettrait cependant pas de contourner la résolution en énergie limitée des détecteurs.

Au prix d'un effort encore plus important pour ajuster un grand nombre de spectres simultanément, les spectres de cibles épaisses pourraient être pris à des pas d'énergie encore plus petits que la résolution du détecteur, voire aux mêmes pas d'énergie que ceux utilisés pour les mesures de cibles minces. Les détails fins de la section efficace seraient alors incorporés dans les variations de la forme de la section efficace avec l'énergie du faisceau incident, comme c'est illustré de manière hypothétique à la figure 6.2, où SIMNRA a été utilisé pour calculer une série de spectres EBS de ^{16}O obtenus pour de petits incréments d'énergie du faisceau incident près de la résonance de 10 keV de large près de 3.045 MeV dans le ^{16}O(α,α)^{16}O, à partir d'une cible d'oxygène pur. Une résolution du détecteur de 15 keV a été utilisée, et il est clair que les effets des détails de la section efficace à un niveau de détail plus fin que 15 keV sont facilement visibles dans la forme du spectre.

Les outils informatiques modernes et les approches d'intelligence artificielle pour le traitement de grands ensembles de données rendraient maintenant possible l'ajustement simultané de centaines, voire de milliers de spectres, et les sections efficaces déduites qui en résultent devraient être définies encore mieux que celles mesurées avec des cibles minces, car chacun des nombreux spectres contient des informations sur les sections efficaces pour toutes les énergies inférieures à l'énergie de la particule incidente.

Étant donné que l'aluminium est une cible très favorable, comme indiqué ci-dessus, et que nous disposons déjà des sections efficaces mesurées avec des cibles minces, les sections efficaces d-^{27}Al obtenues à partir de spectres de cibles épaisses sur de l'aluminium pur constitueraient un cas d'école idéal pour tester l'approche des spectres de cibles épaisses multiples proposée ici.

7.4.2 ^{17}O(p,p)

7.4.2.1 Conclusions

Les premières mesures de l'EBS pour les protons sur ^{17}O ont été effectuées dans le chapitre de cette thèse. Pour un angle de diffusion de laboratoire de 165°, et dans la gamme d'énergies de 600keV- 2 MeV, la section efficace consiste en une composante variable régulière qui augmente de 1.2 fois la section efficace de Rutherford à 600 keV jusqu'à environ 3 fois la section efficace de Rutherford à 2 MeV, sur laquelle quelques structures de résonance sont superposées. Parmi ces résonances EBS, celle qui est intense, avec un pic à 1230 keV et une largeur de 4.5 keV, pourrait être utilisée pour le profilage en profondeur de la concentration de ^{17}O par balayage de l'énergie du faisceau, spécifiquement à des angles de rétrodiffusion élevés, et pourrait fournir une résolution en profondeur d'environ 50 nm dans le silicium.

7.4.2.2 Travaux et articles futurs

Nos tentatives pour fabriquer un film mince de $^{27}Al_2^{17}O_3$ en oxydant soit les films minces d'Al autoportants qui ont été produits pour les mesures de d-^{27}Al, soit une couche mince de ^{27}Al sur un substrat lourd, n'ont pas été couronnées de succès, mais cela vaudrait la peine de poursuivre cette démarche car un film mince de ^{17}O autoportant ou un film aussi mince sur un substrat lourd permettrait une comparaison croisée directe et minutieuse des section efficace mesurées de ^{17}O(d,p&α) avec celles de ^{27}Al(d,p&α).

Nous n'avons trouvé aucun rapport de mesures des sections efficaces des réactions nucléaires ^{17}O(d,α)^{15}N et ^{17}O(d,p)^{18}F dans la littérature. Ces deux réactions ont des valeurs Q positives élevées qui conduisent à des particules alpha et des protons de haute énergie qui devraient être facilement distinguables dans le spectre d'énergie de toutes les particules émises par une cible composée sous irradiation au deutérium. Les cibles nat$Si^{17}O_2$ isotopiquement pures ont été produites par oxydation thermique sèche du silicium dans du $^{17}O_2$ pur à l'INSP. Des expériences initiales pour les sections efficaces d-^{17}O ont été réalisées, et nous avons pu observer un certain nombre de pics de protons et de particules alpha provenant des réactions d-^{17}O, cependant l'interférence des réactions d-Si dans l'épais substrat ^{28}Si a rendu l'interprétation quantitative détaillée des spectres trop incertains pour nous permettre de proposer des sections efficaces bien caractérisées, et elles ne sont donc pas présentées dans cette thèse.

7.4.2.3 Perspective

La section efficace ^{17}O(p,p)^{17}O mesurée dans cette thèse ouvre déjà la voie à des expériences de traçage isotopique stable à trois voies pour la détermination des mécanismes de croissance des films d'oxydes minces, et si elle est appliquée conjointement avec les réactions

d-^{17}O, L'utilisation du ^{18}O comme traceur isotopique stable pour de telles études, en conjonction avec la NRA spécifique au ^{18}O sur SAFIR, a été développée à l'INSP depuis de nombreuses années, et est également disponible dans le nouveau système de dépôt par couche atomique (ALD) développé par l'équipe responsable de SAFIR. Des nanolaminés d'alumine isotopiquement distincts pourraient être élaborés (par exemple 10nm $Al_2^{16}O_3$/10nm $Al_2^{18}O_3$) et recuits dans $^{17}O_2$. La détermination des quantités de chaque isotope incorporé ou perdu pendant le processus de recuit en fonction de la pression partielle d'O_2, de la température de recuit et du temps permettra de déterminer les coefficients de diffusion et les propriétés thermodynamiques telles que les énergies d'activation qui peuvent être comparées aux modèles de transport et d'échange d'oxygène pendant le recuit thermique et utilisées pour guider les paramètres de croissance ALD afin d'obtenir les films d'alumine les plus compacts et les plus stables en termes de composition. Avec les précurseurs ALD disponibles, des études similaires pourraient être envisagées pour la croissance de films minces ou de nanolaminés de HfO_2, TiO_2 et ZnO.

PART III : FARSI VERSION

چکیده فارسی Persian abstract

امروزه فیزیک هسته‌ای انرژی‌های پایین، به‌عنوان یک زمینه تحقیقاتی به نسبت توسعه یافته شناخته می‌شود. اگر چه سازوکار واکنش‌های مربوط به آن مشخص شده است و مدل‌های مناسبی نیز با توجه به فیزیک آن به خوبی توسعه یافته‌اند.با این حال علی رغم همخوانی‌های قابل قبولی که بین داده‌های اندازه‌گیری شده و نظریه‌های موجود است، هنوز یک مدل هسته‌ای کامل و قابل اطمینان با امکان محاسبه سطح‌مقطع واکنش‌ها با دقت مورد نیاز در زمینه‌های اختر فیزیک هسته‌ای یا کاربرد فناوری هسته‌ای در فیزیک نوترون و آنالیز با باریکه یونی وجود ندارد. همواره برای ارائه سطح مقطع یک واکنش خاص می‌بایست از برازش پارامترهای مدل بهره جست. به این منظور دسترسی به داده‌های دقیق مربوط به سطح‌مقطع واکنش هسته‌ای ضروری است. هدف از انجام این رساله دوره دکتری، گسترش دانش اندازه‌گیری سطح مقطع واکنش هسته‌ای در انرژی‌های پایین است.

در این کار پژوهشی هدف نازک خودنگهدار Al ساخته شد و با عناصر سنگین Ag یا Au پوشش داده شد و هدف‌های ساخته شده مشخصه‌یابی شدند. برای کالیبراسیون تعداد یون‌های برخوردی به هدف از سطح مقطع پراکندگی رادرفورد هم زمان با اندازه‌گیری سطح مقطع استفاده شده است. برای دسترسی به داده‌های سطح مقطع دقیق، کالیبراسیون مناسب شتابدهنده در دو آزمایشگاه واندوگراف تهران و نیز واندوگراف پاریس انجام شد. برای پوشش زاویه‌ای بیشتر، زیر ساخت مناسب برای اندازه گیری در زاویه‌های ۱۵۰°، ۱۳۵° و ۱۶۵° در آزمایشگاه پاریس ایجاد شده است. در نهایت سطح مقطع واکنش‌های القایی پرتابه دوترون روی هدف آلومینیوم در زوایای ۱۵۰°، ۱۳۵° و ۱۶۵°، بازه‌های انرژی و گام‌های انرژی مناسب جهت استفاده در آنالیز باریکه یونی در دو آزمایشگاه ایران و فرانسه اندازه گیری، مقایسه، ارزیابی و با هدف ضخیم آزمایش معیارشد.

در ادامه، سطح مقاطع پراکندگی پروتون الاستیک روی ^{17}O برای اولین بار در SAFIR در INSP در پاریس اندازه گیری شد. لایه‌های نازک ^{17}O با اکسیداسیون حرارتی Si در دمای ۱۱۰۰ درجه سانتی‌گراد تحت گاز $^{17}O_2$ تهیه شد. ضخامت فیزیکی سیلیس توسط الیپسومتری و ضخامت اتمی توسط روش آنالیز با باریکه یونی با عدم قطعیت ۳ درصد تعیین شد. مقادیر کمی از ^{16}O و ^{18}O، موجود به

عنوان ناخالصی در گاز O_2 ^{17}بسیار غنی شده مورد استفاده برای رشد این فیلم‌ها، توسط تکنیک‌های NRA با استفاده از واکنش‌های هسته‌ای $^{18}O(p,\alpha)^{15}N$ و $^{16}O(d, p_1)^{17}O$ تعیین شد. در این آزمایش بهره زیاد حاصل از زیرلایه ضخیم سیلیسیومی، با تابش پرتو فرودی در راستای محور (۱۰۰) سیلیسیوم توسط اثر کانال‌زنی یونی فرو نشانده شد. سطح مقطع $^{17}O(p,p)$ اندازه‌گیری شده، با عدم قطعیت سیستماتیک حدود ۱٤٪ ، شامل چندین ساختار رزونانسی است که بر روی یک جزء کاملاً متغیر قرار گرفته‌اند که از حدود ۱,۲ برابر سطح مقطع رادرفورد درانرژی ٦۰۰ کیلوالکترون ولت تا حدود ۳ برابر رادرفورد درانرژی ۲ مگاالکترون ولت افزایش می‌یابد. رزونانس در انرژی ۱۲۳۰ کیلوالکترون ولت نویدبخش پروفایل عمقیEBS ، به ویژه در زوایای پراکندگی بزرگ است.

“ “

Appendix I

Unit conversion for energy, velocity, thickness, areal density, stopping power, and stopping cross section [18]

Multiply units	**by**	**For units**	**Example**
MeV	$\frac{1}{M_1[amu]}$	MeV/amu	$4MeV\,^4He \sim 1MeV/amu$
V/V_0	0.1581	$(MeV/amu)^{1/2}$	$v/v_0 = 1 \sim 0.025$ MeV/amu ^{1}H
$(MeV/amu)^{1/2}$	1.389×10^7	m/s	2MeV ^{4}He $\sim$ V_{Hg}=9.82$\times$ 10^6 m/s
$10^{15}\,atoms/cm^2$	$\frac{1.66\times10^{-2}M_2[amu]}{\rho[g/cm^3]}$	nm	10^{18} atoms/cm^2 for Au $\sim$ 170 nm
$\mu g/cm^2$	$\frac{10}{\rho[g/cm^3]}$	nm	100μ g/cm^2 for C$\sim$ 285 nm
μ/cm^2	$\frac{10^3}{1.661\,M_2[amu]}$	$10^{15}\,atoms/cm^2$	$100\mu g/cm^2$ for $Au \sim 305 \times 10^{15}\ atoms/cm^2$
eV cm^2/10^{15} atoms	$\frac{1}{1.661\,M_2[amu]}$	MeV/(mg/cm^2)	100 eV cm^2/10^{15} atoms for Al_2O_3 $\sim$ 2.95 MeVcm^2/mg [M$_2$=(2M$_{Al}$+3M$_o$)/5; M$_{Al}$=26.98, M$_o$=16.00)]
eV cm^2/10^{15} atoms	$\frac{10^2\rho[g/cm^3]}{1.661M_2[amu]}$	keV/μm	30 eV cm^2/10^{15} atoms for Si$\sim$ 150 keV/μm

Appendix II

Kinematics of nuclear reactions

In IBA experiments, the target nucleus is in the laboratory frame where the detector is located. For a projectile of mass (M_1) and coordinate (x_1) moving along the x axis toward a target nucleus of mass (M_2) and coordinate (x_2), where the center of mass (CM) of the system comprising these two particles, the point with coordinate x_C explained as Eq. 1:

$$x_C = \frac{M_1 x_1 + M_2 x_2}{M_1 + M_2} \tag{1}$$

For projectile velocity ($\vec{v_1}$), x_C moves with the velocity Eq. 2 in the laboratory frame.

$$\vec{V_c} = \frac{M_1 \vec{v_1}}{M_1 + M_2} \tag{2}$$

A CM reference frame is one in which the origin is fixed at the point x_C in Eq. 1, but the target nucleus is not at rest in this frame. However, it has the advantage that before and after the collision, the sum of the momenta of all colliding particles in the CM frame is zero, which simplifies calculations.

It can be seen from Konig's kinetic theorem that the kinetic energy of a projectile and a target is the combined kinetic energy associated with the movement of the particle's center of mass and the particle's movement relative to the center of mass. For kinetic energy of the projectile (E_o) in the laboratory frame and the kinetic energy of a colliding particles (E_{rel}) particles in their relative motion in the CM system, this means that Eq. 3

$$E_1 = \frac{(M_1 + M_2) \times V_c^2}{2} + E_{rel} \tag{3}$$

Substituting Eq. 2 into Eq. 3 gives Eq. 4 as the relationship between E_{rel} and E_o :

$$E_{rel} = \frac{M_2}{M_1 + M_2} \times E_1 \tag{4}$$

An example is determining the correspondence between the resonance energy of the laboratory system and that of the center-of-mass system. From Eq. 4 we can also infer

that the endoergic reaction is only possible for beam energies as in Eq. 5.

$$E_1 \geq \frac{M_1 + M_2}{M_2} \times |Q| \tag{5}$$

There is a need to develop explicitly expressed formulae for the angle transformation between the laboratory frames and CM, including the projectile energy (E_o) as an expression in the laboratory frame only Eqs. 6-9.

$$\tan\theta = \frac{\sin\theta_c}{\gamma_i + \cos\theta_c} \tag{6}$$

$$\cos\theta_c = \left[\cos^2\theta \times \left(1 - \gamma_i^2 \times \sin^2\theta\right)\right]^{1/2} - \gamma_i \times \sin^2\theta \tag{7}$$

where

$$\gamma_3 = \left(\frac{M_1 \times M_3}{M_2 \times M_4}\right)^{\frac{1}{2}} \left(1 + \frac{M_1 + M_2}{M_2}\frac{Q}{E_0}\right)^{-1/2} \tag{8}$$

$$\gamma_4 = \left(\frac{M_1 \times M_4}{M_2 \times M_3}\right)^{\frac{1}{2}} \left(1 + \frac{M_1 + M_2}{M_2}\frac{Q}{E_0}\right)^{-1/2} \tag{9}$$

With $i = 3$ represents the outgoing particle, and $i = 4$ represents the residual nucleus.

There is no change in the total cross sections under the reference transformations frame. Nevertheless, the differential cross sections ($\frac{d\sigma}{d\Omega}$) relies on the frame. The relation between differential cross sections expressed in CM and laboratory frames resulted from the similar number of particles emitted in the respective solid angles in the two frames as Eqs. 10 and 11.

$$\frac{d\sigma}{d\Omega} d\Omega = \frac{d\sigma}{d\Omega}|_c d\Omega_c \tag{10}$$

$$\frac{d\sigma}{d\Omega} \times \sin\theta \times d\theta \times d\phi = \frac{d\sigma}{d\Omega}|_c \sin\theta_c \times d_c \times d\phi_c \tag{11}$$

The azimuth angles ϕ and ϕ_c are identical, so Eqs. 6 and 7 give the transformation relations for polar angles.

Then, the Eqs. 12 and 13 can be derived for the transformation of the differential cross section:

$$\frac{d\sigma}{d\Omega} = \frac{d\sigma}{d\Omega}|_c \frac{(1 + \gamma_i^2 + 2 \times \gamma_i \times \cos\theta_c)^{\frac{3}{2}}}{1 + \gamma_1 \times \cos\theta_c} \tag{12}$$

$$\frac{d\sigma}{d\Omega}|_c = \frac{d\sigma}{d\Omega} \frac{(1 - \gamma_i^2\theta)^{\frac{1}{2}}}{\left[(1 - \gamma_i^2 \times \theta)^{\frac{1}{2}} + \gamma_i \times \cos\theta\right]^2} \tag{13}$$

where γ_i are defined by Eq. 8 and 9.

Bibliography

[1] IBANDL, "Ion beam analysis nuclear data library." https://www-nds.iaea.org/exfor/ibandl.htm.

[2] M. Salimi, O. Kakuee, S. F. Masoudi, H. Rafi-Kheiri, E. Briand, J.-J. Ganem, and I. Vickridge, "Determination and benchmarking of ^{27}Al(d, α) and ^{27}Al(d, p) reaction cross sections for energies and angles relevant to NRA," *Scientific Reports*, vol. 11, no. 1, pp. 1–19, 2021.

[3] M. Salimi, O. Kakuee, S. Masoudi, H. Rafi-kheiri, E. Briand, J.-J. Ganem, and I. Vickridge, "Measurement of (p,p) elastic differential cross sections for ^{17}O in the 0.6–2 MeV range at 165°," *Nuclear Instruments and Methods in Physics Research Section B: Beam Interactions with Materials and Atoms*, vol. 516, pp. 15–22, 2022.

[4] N. Bohr, *The penetration of atomic particles through matter*. Munksgaard Copenhagen, 1948.

[5] W. Whaling, "The energy loss of charged particles in matter," in *Corpuscles and Radiation in Matter II/Korpuskeln und Strahlung in Materie II*, pp. 193–217, Springer, 1958.

[6] U. Fano, "Penetration of protons, alpha particles, and mesons," *Annual review of nuclear science*, vol. 13, no. 1, pp. 1–66, 1963.

[7] P. Sigmund, "Energy loss of charged particles in solids," in *Radiation damage processes in materials*, 1975.

[8] P. Sigmund, *Stopping of heavy ions: a theoretical approach*, vol. 204. Springer Science & Business Media, 2004.

[9] American Institute of Physics and Gray, Dwight E, *American Institute of Physics Handbook: 3d Ed.* McGraw-Hill, 1972.

[10] M. Inokuti, "Inelastic collisions of fast charged particles with atoms and molecules—the Bethe theory revisited," *Reviews of modern physics*, vol. 43, no. 3, p. 297, 1971.

[11] S. P. Ahlen, "Theoretical and experimental aspects of the energy loss of relativistic heavily ionizing particles," *Reviews of modern physics*, vol. 52, no. 1, p. 121, 1980.

[12] A. Wambersie, J. Zoetelief, H. G. Menzel, and H. Paretzke, "The ICRU (International Commission on Radiation Units and Measurements): its contribution to dosimetry in diagnostic and interventional radiology," *Radiation protection dosimetry*, vol. 117, no. 1-3, pp. 7–12, 2005.

[13] J. F. Ziegler, "Stopping Cross-section For Energetic Ions In AU Metals, vol. 5," 1980.

[14] J. F. Ziegler and J. P. Biersack, "The stopping and range of ions in matter," in *Treatise on heavy-ion science*, pp. 93–129, Springer, 1985.

[15] J. D. Jackson, "Classical electrodynamics," 1999.

[16] L. C. Northcliffe, "Passage of heavy ions through matter," *Annual review of nuclear science*, vol. 13, no. 1, pp. 67–102, 1963.

[17] H.-D. Betz, "Charge states and charge-changing cross sections of fast heavy ions penetrating through gaseous and solid media," *Reviews of modern physics*, vol. 44, no. 3, p. 465, 1972.

[18] Y. Wang and M. A. Nastasi, *Handbook of modern ion beam materials analysis*. Materials Research Society Pittsburgh, PA, 2009.

[19] J. F. Ziegler, M. D. Ziegler, and J. P. Biersack, "SRIM (http://www. srim. org/)," *Last Accessed*, pp. 12–13, 2014.

[20] N. Bohr, " II. On the theory of the decrease of velocity of moving electrified particles on passing through matter ," *The London, Edinburgh, and Dublin Philosophical Magazine and Journal of Science*, vol. 25, pp. 10–31, jan 1913.

[21] H. Bethe, "Bremsformel für elektronen relativistischer geschwindigkeit," *Zeitschrift für Physik*, vol. 76, no. 5, pp. 293–299, 1932.

[22] B. Firsov, "NUMBER 5 NOVEMBER," *J. Exptl. Theoret. Phys. (U.S.S.R.)*, vol. 36, no. 9, pp. 1517–1523, 1959.

[23] M. Mayer, "SIMNRA, a simulation program for the analysis of NRA, RBS and ERDA," in *AIP conference proceedings*, vol. 475, pp. 541–544, American Institute of Physics, 1999.

[24] B. Wilken and T. A. Fritz, "Energy distribution functions of low energy ions in silicon absorbers measured for large relative energy losses," *Nuclear Instruments and Methods*, vol. 138, no. 2, pp. 331–343, 1976.

[25] C. Tschalär, "Straggling distributions of large energy losses," *Nuclear Instruments and Methods*, vol. 61, pp. 141–156, may 1968.

[26] D. Jalabert, I. Vickridge, and A. Chabli, *Swift Ion Beam Analysis in Nanosciences*. John Wiley & Sons, 2017.

[27] A. Gurbich, "On the concept of an actual Coulomb barrier," *Nuclear Instruments and Methods in Physics Research Section B: Beam Interactions with Materials and Atoms*, vol. 217, no. 1, pp. 183–186, 2004.

[28] R. Eisberg and R. Resnick, *Quantum physics of atoms, molecules, solids, nuclei, and particles*. 1985.

[29] K. S. Krane, *Introductory nuclear physics*. John Wiley & Sons, 1991.

[30] H. R. Verma, *Atomic and nuclear analytical methods*. Springer, 2007.

[31] D. Benzeggouta, I. Vickridge, N. P. Barradas, M. Doebeli, C. Jeynes, and A. Vantomme, "Handbook on Best Practice for Minimising Beam Induced Damage during IBA," no. March, 2011.

[32] F. Garrido, H. Khodja, N. Moncoffre, C. Pacheco, and Eds., "Conference on Ion Beam Analysis," *IBA 2019 International Conference on Ion Beam Analysis NIMB Virtual Special Issue*, 2019.

[33] G. Deconninck, *Introduction to radioanalytical physics*, vol. 1. Elsevier, 2016.

[34] I. Mitchell and K. Barfoot, "Particle induced x-ray emission analysis application to analytical problems," *Nucl. Sci. Appl., Sect. B*, vol. 1, no. 2, pp. 99–162, 1981.

[35] T. Trojek, T. Čechák, and L. Musílek, "Recognition of pigment layers in illuminated manuscripts by means of K_α/K_β and L_α/L_β ratios of characteristic X-rays," *Applied Radiation and Isotopes*, vol. 68, no. 4-5, pp. 871–874, 2010.

[36] T. Calligaro, J. C. Dran, and J. Salomon, "Chapter 5 Ion beam microanalysis," *Comprehensive Analytical Chemistry*, vol. 42, pp. 227–276, jan 2004.

[37] G. Dollinger, A. Bergmaier, T. Faestermann, and C. Frey, "High resolution depth profile analysis by elastic recoil detection with heavy ions," *Fresenius' journal of analytical chemistry*, vol. 353, no. 3, pp. 311–315, 1995.

[38] M. Kokkoris, "Nuclear Reaction Analysis (NRA) and Particle-Induced Gamma-Ray Emission (PIGE)," *Characterization of Materials*, pp. 1–18, 2002.

[39] A. Jokar, O. Kakuee, and M. Lamehi-Rachti, "Differential cross sections measurement of ^{31}P (p, pγ1) 31P reaction for PIGE applications," *Nuclear Instruments and Methods in Physics Research Section B: Beam Interactions with Materials and Atoms*, vol. 383, pp. 152–155, 2016.

[40] P. Dimitriou, H.-W. Becker, I. Bogdanović-Radović, M. Chiari, A. Goncharov, A. P. Jesus, O. Kakuee, A. Z. Kiss, A. Lagoyannis, and J. Räisänen, "Development of a reference database for particle-induced gamma-ray emission spectroscopy," *Nuclear Instruments and Methods in Physics Research Section B: Beam Interactions with Materials and Atoms*, vol. 371, pp. 33–36, 2016.

[41] J. R. Tesmer and M. Nastasi, "Handbook of modern ion beam materials analysis," *Materials Research Society, 9800 McKnight Rd, Suite 327, Pittsburgh, PA 15237, USA, 1995. 700*, 1995.

[42] M. Wang, G. Audi, F. G. Kondev, W. J. Huang, S. Naimi, and X. Xu, "The AME2016 atomic mass evaluation," *Chin. Phys. C*, vol. 41, p. 30003, 2017.

[43] J. B. Marion and F. B. Hagedorn, "1.75-Mev Resonance in ^{13}C(p, γ)^{14}N," *Physical Review*, vol. 104, no. 4, p. 1028, 1956.

[44] J. W. Maas, E. Somorjai, H. D. Graber, C. A. Van Den Wijngaart, C. Van Der Leun, and P. M. Endt, "Investigation of 28Si levels with the (α, γ) and (p, γ) reactions," *Nuclear Physics A*, vol. 301, no. 2, pp. 213–236, 1978.

[45] P. M. Endt and C. Van der Leun, "Energy levels of A= 21 44 nuclei (V)," *Nuclear Physics A*, vol. 214, pp. 1–625, 1973.

[46] S. A. Brindhaban, P. H. Barker, M. J. Keeling, and W. B. Wood, "Accelerator beam energy calibration with the ^{27}Al(p,n) and ^{27}Al(p, γ) reactions," *Nuclear Instruments and Methods in Physics Research Section A: Accelerators, Spectrometers, Detectors and Associated Equipment*, vol. 340, no. 3, pp. 436–441, 1994.

[47] S. Harissopulos, C. Chronidou, K. Spyrou, T. Paradellis, C. Rolfs, W. H. Schulte, and H. W. Becker, "The ^{27}Al(p, γ)^{28}Si reaction: direct capture cross-section and resonance strengths at E p= 0.2-1.12 MeV," *The European Physical Journal A-Hadrons and Nuclei*, vol. 9, no. 4, pp. 479–489, 2000.

[48] J. B. Marion, "Accelerator calibration energies," *Reviews of modern physics*, vol. 38, no. 4, p. 660, 1966.

[49] F. Ajzenberg-Selove, "Energy levels of light nuclei A= 18–20," *Nuclear Physics A*, vol. 475, no. 1, pp. 1–198, 1987.

[50] P. H. Barker, P. D. Harty, M. J. Keeling, W. B. Wood, and P. A. Amundsen, "Determination of the energy of the 1.75 MeV resonance in the ^{13}C (p, γ)^{14}N reaction in terms of a one-volt standard," *Metrologia*, vol. 39, no. 4, p. 371, 2002.

[51] R. O. Bondelid and C. A. Kennedy, "Precise determination of nuclear reaction energies and measurements of resonance widths," *Physical Review*, vol. 115, pp. 1601–1612, sep 1959.

[52] J. Räisänen and P. O. Tikkanen, "Calibration of accelerator proton energy by the ^{14}N(p,p'γ)^{14}N reaction resonances," *Nuclear Instruments and Methods in Physics Research Section A: Accelerators, Spectrometers, Detectors and Associated Equipment*, vol. 723, pp. 5–7, 2013.

[53] P. Rao, S. Kumar, S. Vikramkumar, and V. S. Raju, "Measurement of differential cross-sections and widths of resonances in ^{32}S(p, p'γ)^{32}S reaction in the 3.0–4.0 MeV region," *Nuclear Instruments and Methods in Physics Research Section B: Beam Interactions with Materials and Atoms*, vol. 269, no. 21, pp. 2557–2562, 2011.

[54] T. Osipowicz, K. P. Lieb, and S. Brüssermann, "Frozen target measurements of the 430 kev ^{15}N (p, $\alpha\psi$) resonance," *Nuclear Instruments and Methods in Physics Research B*, vol. 18, no. 1, pp. 232–235, 1986.

[55] J. B. MARION, "JL FOWLER Fast neutron physics," *Interscience Publiahers New York*, 1960.

[56] J. H. Kelley, R. S. Canon, S. J. Gaff, R. M. Prior, B. J. Rice, E. C. Schreiber, M. Spraker, D. R. Tilley, E. A. Wulf, and H. R. Weller, "The ^{11}B(p, γ)^{12}C reaction below 100 keV," *Physical Review C*, vol. 62, no. 2, p. 25803, 2000.

[57] O. Kakuee, V. Fathollahi, and M. Lamehi-Rachti, "Development of a versatile user-friendly IBA experimental chamber," *Nuclear Instruments and Methods in Physics Research Section B: Beam Interactions with Materials and Atoms*, vol. 371, pp. 156–160, 2016.

[58] H. Rafi-Kheiri, O. Kakuee, and M. Lamehi-Rachti, "Differential cross section measurement of the ^{nat}O(d,d$_0$) reaction at energies and angles relevant to EBS," *Nuclear Instruments and Methods in Physics Research Section B: Beam Interactions with Materials and Atoms*, vol. 373, pp. 40–43, 2016.

[59] G. Amsel, E. D'Artemare, and E. Girard, "A simple, digitally controlled, automatic, hysteresis free, high precision energy scanning system for Van de Graaff type accelerators: Part I: Principle, results and applications," *Nuclear Instruments and Methods in Physics Research*, vol. 205, no. 1-2, pp. 5–26, 1983.

[60] G. Amsel, E. D'Artemare, G. Battistig, E. Girard, L. G. Gosset, and P. Révész, "Narrow nuclear resonance position or cross section shape measurements with a high precision computer controlled beam energy scanning system," *Nuclear Instruments and Methods in Physics Research Section B: Beam Interactions with Materials and Atoms*, vol. 136, pp. 545–550, 1998.

[61] I. Vickridge and G. Amsel, "SPACES: A PC implementation of the stochastic theory of energy loss for narrow-resonance depth profiling," *Nuclear Instruments and Methods in Physics Research Section B: Beam Interactions with Materials and Atoms*, vol. 45, no. 1-4, pp. 6–11, 1990.

[62] D. Bachiller-Perea, A. Munoz-Martin, P. Corvisiero, D. Jimenez-Rey, V. Joco, A. Maira, A. Nakbi, A. Rodriguez, J. Narros, and A. Zucchiatti, "New energy calibration of the CMAM 5MV tandem accelerator," *Energy Procedia*, vol. 41, pp. 57–63, 2013.

[63] D. M. Scott and B. M. Paine, "Accelerator energy calibration using nonresonant nuclear reactions," *Nuclear Instruments and Methods in Physics Research*, vol. 218, no. 1-3, pp. 154–158, 1983.

[64] P. S. Morrall, "The target preparation laboratory at daresbury," *Nuclear Instruments and Methods in Physics Research Section A: Accelerators, Spectrometers, Detectors and Associated Equipment*, vol. 590, no. 1-3, pp. 118–121, 2008.

[65] I. Sugai, "An application of a new type deposition method to nuclear target preparation," *Nuclear Instruments and Methods in Physics Research Section A: Accelerators, Spectrometers, Detectors and Associated Equipment*, vol. 397, no. 1, pp. 81–90, 1997.

[66] K. Takamiya, T. Ohtsuki, H. Yuki, T. Mitsugashira, N. Sato, T. Suzuki, M. Fujita, T. Shinozuka, Y. Kasamatsu, and H. Kikunaga, "Target preparation by the precipitation method for nuclear reactions," *Applied radiation and isotopes*, vol. 65, no. 1, pp. 32–35, 2007.

[67] G. Sletten and P. Knudsen, "Preparation of isotope targets by heavy ion sputtering," *Nuclear Instruments and Methods*, vol. 102, no. 3, pp. 459–463, 1972.

[68] L. Yaffe, "Preparation of thin films, sources, and targets," *Annual review of nuclear science*, vol. 12, no. 1, pp. 153–188, 1962.

[69] N. Sarma, "THE CARBON FILMS FOR USE WITH ELECTROSTATIC ACCELERATORS," *Nuclear Instr.*, vol. 2, 1958.

[70] Y. A. Bin'kovskii, O. F. Nemets, and V. A. Stepanenko, "PREPARATION OF FREE FILMS BY VACUUM EVAPORATION METHOD," *Pribory i Tekh. Ekspt.*, vol. 6, no. 5, 1961.

[71] G. Amsel and J. A. Davies, "Precision standard reference targets for microanalysis by nuclear reactions," *Nuclear Instruments and Methods in Physics Research*, vol. 218, no. 1-3, pp. 177–182, 1983.

[72] H. H. Andersen, F. Besenbacher, P. Loftager, and W. Möller, "Large-angle scattering of light ions in the weakly screened Rutherford region," *Physical review A*, vol. 21, no. 6, p. 1891, 1980.

[73] C. Cohen, J. Davies, A. Drigo, and T. Jackman, "Intercomparison of absolute standards for RBS studies," *Nuclear Instruments and Methods in Physics Research*, vol. 218, no. 1-3, pp. 147–148, 1983.

[74] G. Amsel, J. P. Nadai, C. Ortega, and J. Siejka, "Precision absolute thin film standard reference targets for nuclear reaction microanalysis of oxygen isotopes. Part II: ^{18}O and ^{17}O standards," *Nuclear Instruments and Methods*, vol. 149, no. 1-3, pp. 713–720, 1978.

[75] G. Amsel, J. P. Nadai, C. Ortega, S. Rigo, and J. Siejka, "Precision absolute thin film standard reference targets for nuclear reaction microanalysis of oxygen isotopes. Part I: ^{16}O standards," *Nuclear Instruments and Methods*, vol. 149, no. 1-3, pp. 705–712, 1978.

[76] F. E. Carpenter and J. A. Curcio, "Preparation of Unbacked Metallic Films," *Review of Scientific Instruments*, vol. 21, no. 7, p. 675, 1950.

[77] C. D. Cavellin, I. Trimaille, J. J. Ganem, M. D'Angelo, I. Vickridge, A. Pongracz, and G. Battistig, "An ^{18}O study of the interaction between carbon monoxide and dry thermal SiO_2 at 1100 °c," *Journal of Applied Physics*, vol. 105, p. 033501, feb 2009.

[78] G. Amsel and D. Samuel, "Microanalysis of the stable isotopes of oxygen by means of nuclear reactions," *Analytical Chemistry*, vol. 39, no. 14, pp. 1689–1698, 1967.

[79] B. E. Deal and A. S. Grove, "General relationship for the thermal oxidation of silicon," *Journal of Applied Physics*, vol. 36, pp. 3770–3778, jul 1965.

[80] B. E. Deal and C. R. Helms, *The physics and chemistry of SiO_2 and the Si-SiO_2 interface*. Springer Science & Business Media, 2013.

[81] W. HERTL and W. W. PULTZ, "Disproportionation and Vaporization of Solid Silicon Monoxide," *Journal of the American Ceramic Society*, vol. 50, pp. 378–381, jul 1967.

[82] V. Silica, F. E. WAGSTAFF, and K. J. RICHARDS, "Preparation and Crystallization Behavior of Oxygen-Deficient," *Journal of the American Ceramic Society*, vol. 48, pp. 382–383, jul 1965.

[83] M. K. Schurman and M. Tomozawa, "Equilibrium oxygen vacancy concentrations and oxidant diffusion in germania, silica, and germania-silica glasses," *Journal of non-crystalline solids*, vol. 202, no. 1-2, pp. 93–106, 1996.

[84] M. Chiari and P. Dimitriou, "Technical Meeting on Benchmarking Experiments for Ion Beam Analysis. Summary Report," tech. rep., 2016.

[85] M. Kokkoris, S. Dede, K. Kantre, A. Lagoyannis, E. Ntemou, V. Paneta, K. Preketes-Sigalas, G. Provatas, R. Vlastou, and I. Bogdanović-Radović, "Benchmarking the evaluated proton differential cross sections suitable for the EBS analysis of ^{nat}Si and ^{16}O," *Nuclear Instruments and Methods in Physics Research Section B: Beam Interactions with Materials and Atoms*, vol. 405, pp. 50–60, 2017.

[86] A. F. Gurbich, "SigmaCalc recent development and present status of the evaluated cross-sections for IBA," *Nuclear Instruments and Methods in Physics Research Section B: Beam Interactions with Materials and Atoms*, vol. 371, pp. 27–32, 2016.

[87] H. Rafi-kheiri, O. Kakuee, and M. Lamehi-Rachti, "Differential cross section measurement of ^{16}O(d, $p_{0,1}$) reactions at energies and angles relevant to NRA," *Nuclear Instruments and Methods in Physics Research Section B: Beam Interactions with Materials and Atoms*, vol. 371, pp. 46–49, 2016.

[88] A. F. Gurbich and S. L. Molodtsov, "Application of IBA techniques to silicon profiling in protective oxide films on a steel surface," *Nuclear Instruments and Methods in Physics Research Section B: Beam Interactions with Materials and Atoms*, vol. 226, no. 4, pp. 637–643, 2004.

[89] M. Kokkoris, P. Misaelides, S. Kossionides, C. Zarkadas, A. Lagoyannis, R. Vlastou, C. T. Papadopoulos, and A. Kontos, "A detailed study of the ^{12}C(d, p_0)^{13}C reaction at detector angles between 135° and 170°, for the energy range Ed, lab= 900–2000 keV," *Nuclear Instruments and Methods in Physics Research Section B: Beam Interactions with Materials and Atoms*, vol. 249, no. 1-2, pp. 77–80, 2006.

[90] W. A. Lanford, M. Parenti, B. J. Nordell, M. M. Paquette, A. N. Caruso, M. Mäntymäki, J. Hämäläinen, M. Ritala, K. B. Klepper, and V. Miikkulainen,

"Nuclear reaction analysis for H, Li, Be, B, C, N, O and F with an RBS check," *Nuclear Instruments and Methods in Physics Research Section B: Beam Interactions with Materials and Atoms*, vol. 371, pp. 211–215, 2016.

[91] H. R. Verma, *Atomic and nuclear analytical methods*. Springer, 2007.

[92] J. R. Bird, "Total analysis by IBA," *Nuclear Instruments and Methods in Physics Research Section B: Beam Interactions with Materials and Atoms*, vol. 45, no. 1-4, pp. 514–518, 1990.

[93] C. Jeynes, V. V. Palitsin, M. Kokkoris, A. Hamilton, and G. W. Grime, "On the accuracy of Total-IBA," *Nuclear Instruments and Methods in Physics Research Section B: Beam Interactions with Materials and Atoms*, vol. 465, pp. 85–100, 2020.

[94] C. Jeynes, M. J. Bailey, N. J. Bright, M. E. Christopher, G. W. Grime, B. N. Jones, V. V. Palitsin, and R. P. Webb, ""Total IBA"–Where are we?," *Nuclear Instruments and Methods in Physics Research Section B: Beam Interactions with Materials and Atoms*, vol. 271, pp. 107–118, 2012.

[95] J. Demeulemeester, D. Smeets, N. P. Barradas, A. Vieira, C. M. Comrie, K. Temst, and A. Vantomme, "Artificial neural networks for instantaneous analysis of real-time Rutherford backscattering spectra," *Nuclear Instruments and Methods in Physics Research Section B: Beam Interactions with Materials and Atoms*, vol. 268, no. 10, pp. 1676–1681, 2010.

[96] G. Amsel, "Spectroscopie par détecteurs à semiconducteur des réactions nucléaires O^{16+} d, O^{18+} p," in *Annales de Physique*, vol. 13, pp. 297–344, 1964.

[97] M. Kokkoris, K. Michalakis, P. Misaelides, A. Lagoyannis, S. Harissopulos, R. Vlastou, and C. T. Papadopoulos, "Study of selected differential cross-sections of the ^{28}Si(d, p_0, p_1, p_2, p_3) reactions for NRA purposes," *Nuclear Instruments and Methods in Physics Research Section B: Beam Interactions with Materials and Atoms*, vol. 267, no. 8-9, pp. 1744–1747, 2009.

[98] A. Gurbich and S. Molodtsov, "Measurement of (d, p) and (d, α) differential cross-sections for aluminum," *Nuclear Instruments and Methods in Physics Research Section B: Beam Interactions with Materials and Atoms*, vol. 266, no. 16, pp. 3535–3539, 2008.

[99] R. Mateus, M. Fonseca, A. P. Jesus, H. Luís, and J. P. Ribeiro, "PIGE analysis and profiling of aluminium," *Nuclear Instruments and Methods in Physics Research Section B: Beam Interactions with Materials and Atoms*, vol. 266, no. 8, pp. 1490–1492, 2008.

[100] M. J. F. Healy, A. J. Pidduck, G. Dollinger, L. Gorgens, and A. Bergmaier, "Ion beam analysis of aluminium in thin layers," *Nuclear Instruments and Methods in Physics Research Section B: Beam Interactions with Materials and Atoms*, vol. 190, no. 1-4, pp. 630–635, 2002.

[101] S. Pellegrino, L. Beck, P. Trouslard, and P. Trocellier, "Differential cross-sections for nuclear reactions on Al and Si induced by deuterons at low energy (1–2 MeV)," *Nuclear Instruments and Methods in Physics Research Section B: Beam Interactions with Materials and Atoms*, vol. 266, no. 10, pp. 2268–2272, 2008.

[102] G. Corleo and S. Sambataro, "Differential absolute cross-section for the nuclear reactions ^{27}Al(d, p)^{28}Al and ^{27}Al(d, α)^{25}Mg at θ_L= 90°," *Il Nuovo Cimento B (1965-1970)*, vol. 56, no. 1, pp. 83–88, 1968.

[103] G. Corleo, G. Pappalardo, and A. Rubbino, "Analysis of nuclear reactions with the ^{29}Si as intermediate system," *Il Nuovo Cimento B (1965-1970)*, vol. 52, no. 1, pp. 248–250, 1967.

[104] C. S. Lin and E. K. Lin, "The reaction ^{27}Al(d,p)^{28}Al in the energy range of the deuteron from 2.0 MeV to 3.0 MeV," *Il Nuovo Cimento A (1965-1970)*, vol. 66, no. 2, pp. 336–342, 1970.

[105] K. Holz, J. Lietard, and M. M. Somoza, "High-power 365 nm UV LED mercury arc lamp replacement for photochemistry and chemical photolithography," *ACS sustainable chemistry & engineering*, vol. 5, no. 1, pp. 828–834, 2017.

[106] R. Dalmau, B. Moody, R. Schlesser, S. Mita, J. Xie, M. Feneberg, B. Neuschl, K. Thonke, R. Collazo, A. Rice, *et al.*, "Growth and characterization of AlN and AlGaN epitaxial films on AlN single crystal substrates," *Journal of The Electrochemical Society*, vol. 158, no. 5, p. H530, 2011.

[107] A. Redondo-Cubero, R. Gago, F. González-Posada, U. Kreissig, M.-A. di Forte Poisson, A. F. Braña, and E. Muñoz, "Aluminium incorporation in AlxGa1 xN/GaN heterostructures: A comparative study by ion beam analysis and X-ray diffraction," *Thin Solid Films*, vol. 516, no. 23, pp. 8447–8452, 2008.

[108] J. C. Zhang, M. F. Wu, J. F. Wang, J. P. Liu, Y. T. Wang, J. Chen, R. Q. Jin, and H. Yang, "A study of the degree of relaxation of AlGaN epilayers on GaN template," *Journal of crystal growth*, vol. 270, no. 3-4, pp. 289–294, 2004.

[109] E. Gadioli, I. Iori, M. Mangialaio, and G. Pappalardo, "Study of the ^{27}Al(d, α)^{25}Mg and ^{27}Al(d, p)^{28}Al nuclear reactions at 2 MeV deuteron energy," *Il Nuovo Cimento (1955-1965)*, vol. 38, no. 3, pp. 1105–1132, 1965.

[110] M. Corti, G. M. Marcazzan, L. M. Colli, and M. Milazzo, "Direct effect and evaporation mechanism in ^{27}Al(d, p)^{28}Al and ^{27}Al(d, α)^{25}Mg reactions," *Nuclear Physics*, vol. 77, no. 3, pp. 625–640, 1966.

[111] A. Osman and G. U. Din, "The (d, p) Reactions below 3.0 MeV," *Annalen der Physik*, vol. 491, no. 1, pp. 64–80, 1979.

[112] H. Rafi-Kheiri, O. Kakuee, and M. Lamehi-Rachti, "Measurements of the ^{24}Mg(d,p$_{0,1,2,3,4}$) and ^{nat}Mg(d,d$_0$) reactions cross sections in the energy range of 1.2-2 MeV for NRA and EBS applications," *Nuclear Instruments and Methods in Physics Research, Section B: Beam Interactions with Materials and Atoms*, vol. 373, pp. 63–69, 2016.

[113] T. Rubehn, G. J. Wozniak, L. Phair, L. G. Moretto, and K. M. Yu, "Characterization of nuclear physics targets using Rutherford backscattering and particle induced X-ray emission," *Nuclear Instruments and Methods in Physics Research Section A: Accelerators, Spectrometers, Detectors and Associated Equipment*, vol. 387, no. 3, pp. 328–332, 1997.

[114] M. A. Abuzeid, Y. P. Antoufiev, A. T. Baranik, M. I. El-Zaiki, T. M. Nower, and P. V. Sorokin, "The reaction ^{27}Al(d, α)^{25}Mg in the deuteron energy range 1.5–2.6 MeV," *Nuclear Physics*, vol. 54, pp. 315–320, 1964.

[115] D. Abriola, N. P. Barradas, I. Bogdanović-Radović, M. Chiari, A. F. Gurbich, C. Jeynes, M. Kokkoris, M. Mayer, A. R. Ramos, and L. Shi, "Development of a reference database for Ion Beam Analysis and future perspectives," *Nuclear Instruments and Methods in Physics Research Section B: Beam Interactions with Materials and Atoms*, vol. 269, no. 24, pp. 2972–2978, 2011.

[116] R. Ansari and L. Valbonesi, *Signals and Systems*. Prentice Hall, 2005.

[117] J. L. Devore, *Probability and Statistics for Engineering and the Sciences*. Cengage Learning, 2015.

[118] A. R. Ramos, A. Paul, L. Rijniers, M. F. Da Silva, and J. C. Soares, "Measurement of (p, p) elastic differential cross-sections for carbon, nitrogen, oxygen, aluminium and silicon in the 500-2500 keV range at 140 and 178 laboratory scattering angles," *Nuclear Instruments and Methods in Physics Research Section B: Beam Interactions with Materials and Atoms*, vol. 190, no. 1-4, pp. 95–99, 2002.

[119] M. Nastasi, J. W. Mayer, and Y. Wang, *Ion beam analysis: fundamentals and applications*. CRC Press, 2014.

[120] A. F. Gurbich, "Differential Cross Sections for Elastic Scattering of Protons and Helions from Light Nuclei," in *Lectures given at the Workshop on Nuclear Data for Science and Technology: Materials Analysis*, 2003.

[121] J. Demarche and G. Terwagne, "Precise measurement of the differential cross section from the ^{16}O (α, α) ^{16}O elastic reaction at 165° and 170° between 2.4 and 6.0 MeV," *Journal of applied physics*, vol. 100, no. 12, p. 124909, 2006.

[122] G. Battistig, G. Amsel, E. D'Artemare, and I. Vickridge, "A very narrow resonance in ^{18}O(p, α)^{15}N near 150 keV: Application to isotopic tracing. II. High resolution depth profiling of ^{18}O," *Nuclear Instruments and Methods in Physics Research Section B: Beam Interactions with Materials and Atoms*, vol. 66, no. 1-2, pp. 1–10, 1992.

[123] G. Battistig, G. Amsel, E. D'Artemare, and I. Vickridge, "A very narrow resonance in ^{18}O(p, α)^{15}N near 150 keV: Application to isotopic tracing: I. Resonance width measurement," *Nuclear Instruments and Methods in Physics Research Section B: Beam Interactions with Materials and Atoms*, vol. 61, no. 4, pp. 369–376, 1991.

[124] J. C. Sens, F. Rietsch, A. Pape, and R. Armbruster, "A spectroscopic study of 18F:(I). The ^{17}O(p,p)^{17}O and ^{17}O(p, α_0)^{14}N reactions," *Nuclear Physics A*, vol. 199, no. 2, pp. 232–240, 1973.

[125] J. C. Sens, S. M. Refaei, A. B. Mohamed, and A. Pape, "Search for simple configurations in F. 18 I. The ^{17}O(p,p)^{17}O reaction," *Physical Review C*, vol. 16, no. 6, p. 2129, 1977.

[126] K. Yagi, K. Katori, H. Ohnuma, Y. Hashimoto, and Y. Nogami, "Experiment on Elastic Scattering of Protons by ^{18}O," *Journal of the Physical Society of Japan*, vol. 17, no. 4, pp. 595–603, 1962.

[127] H. J. Kim, W. T. Milner, and F. K. McGowan, "Nuclear cross sections for charged-particle-induced reactions: N and O," *Nuclear Data Sheets. Section A*, vol. 3, no. 2, pp. 123–127, 1967.

[128] D. L. Sellin, H. W. Newson, and E. G. Bilpuch, "High resolution investigation of resonances in 19F," *Annals of Physics*, vol. 51, no. 3, pp. 461–475, 1969.

[129] G. Amsel and D. Samuel, "The mechanism of anodic oxidation," *Journal of Physics and Chemistry of Solids*, vol. 23, no. 12, pp. 1707–1718, 1962.

[130] N. Kitamura, K. Fukumi, J. Nishii, and N. Ohno, "Relationship between refractive index and density of synthetic silica glasses," *Journal of applied physics*, vol. 101, no. 12, p. 123533, 2007.

[131] S. Rigo, G. Barbottin, and A. Vapaille, "Instabilities in silicon devices," *Silicon Passivation and Related Instabilities*, vol. 1, p. 32, 1986.